Bichromatic Collimation to Make an Intense Helium Beam

A Dissertation Presented

by

Matthew Jeremiah Partlow

to

The Graduate School

in Partial Fulfillment of the Requirements

for the Degree of

Doctor of Philosophy

in

Physics

Stony Brook University

December 2004

Stony Brook University

The Graduate School

Matthew Jeremiah Partlow

We, the Dissertation committee for the above candidate for the Doctor of Philosophy degree, hereby recommend acceptance of the Dissertation.

Distinguished Teaching Professor Harold J. Metcalf, Dissertation Director

Department of Physics and Astronomy, Stony Brook University

Professor Madappa Prakash, Chairman of Defense

Department of Physics and Astronomy, Stony Brook University

Professor Norbert Pietralla

Department of Physics and Astronomy, Stony Brook University

Professor Philip M. Johnson

Department of Chemistry, Stony Brook University

This Dissertation is accepted by the Graduate School.

Dean of the Graduate School

Abstract of the Dissertation

Bichromatic Collimation to Make an Intense Helium Beam

by

Matthew Jeremiah Partlow

Doctor of Philosophy

in

Physics

Stony Brook University

2004

Over the past two decades of development in the field of laser cooling, atomic beam slowing and collimation has mainly been implemented within the framework of a monochromatic laser beam. In this picture, the radiative force arises from absorption followed by spontaneous emission and is therefore limited in magnitude to $F_{rad} \equiv \hbar k\gamma/2$ by the excited-state decay rate, γ. Furthermore, the velocity capture range is limited to $v_c \equiv \pm\gamma/k$. Both limits can be overcome by coherent control of the momentum exchange between the atoms and the light field. This situation may be realized by a light field created by two counterpropagating beams, each with two frequencies mutually detuned from

atomic resonance by $\pm\delta$. The resulting magnitude and velocity range of the bichromatic force scale with this detuning: $F_{bichro} \sim \hbar k\delta/\pi$ and $v_c \sim \pm\delta/2k$, neither limited by γ, but rather set by the experimentally chosen δ. The magnitude of the force allows for very short interaction lengths, leading to the possibility of compact, bright atomic sources. This technique is of particular interest to the brightening of metastable rare gas atomic beams, which have metastable production efficiencies on the order of 10^{-5}.

We have used the bichromatic force to collimate a beam of metastable helium (He*). Transverse compression of the atomic beam was realized with four separate bichromatic interaction regions, with a total length of only ~ 5 cm. We have observed an extraordinary capture of atoms from within a 175 mrad cone, a factor of 6 larger than the previously reported value for He*. The collimated beam has an integrated flux of 1.4×10^{11} atoms/s and thus contains $\sim 1/4$ of the total output of the source . Further compression with a subsequent optical molasses yields an overall increase in brightness by a factor of 4100.

For my wife, Jennifer

Contents

List of Figures

List of Tables

Acknowledgements

"Once in a while you get shown the light in the strangest of places if you look at it right" - Robert Hunter

My time here at Stony Brook has been quite a journey. The opening line from Dickens' "A Tale of Two Cities" comes to mind in describing it. In almost all graduate careers there are some dark days, however, in retrospect, my time here certainly was "the best of times." It still amazes me how much I have learned, grown, and matured while being here. In some ways it felt as though the time crawled by, but looking back on it now, while it still seems long, it feels like it went by quite fast. This journey would not have been remotely possible without the help and support many, many people. Here I hope to recognize some of them now, and ask to be forgiven by those whom I forget.

First, I would like to thank my parents. Although sometimes separated by great distances, their unconditional support and love has meant a great

deal to me. They believed in me even in those times when I did not believe in myself.

That Hal Metcalf would be my advisor I think was inevitable. He was responsible for my decision to come to Stony Brook. As I was exploring my options for graduate study, I waivered between two schools. At an APS regional conference, I saw Hal give a talk and realized then that the other school was not an option, since they had no AMO physics program. Hal is an exceptional advisor, whose passion for research and for mentoring students is obvious to anyone who gets to know him. To all of his students he is an incomparable role model as a physicist, who provides a great learning environment in the lab. More often than not, when I was stuck on something, Hal would always have an idea or suggestion that cut straight to the heart of the matter. Looking back now, I am surprised by how long it took me to call him "Hal" instead of "Professor Metcalf" despite his insistence otherwise. I am more than fortunate to have had the opportunity to work with him.

Even with spending long days in the lab, I had plenty of opportunities to explore the world by getting to know and working with the wide variety of students, post-docs, and visiting professors who were in the lab at one point or another during my time here. In my early years there was Jo Bellanca, Marty Williams, Liang Liu, and Felix Chi. Felix's experiment was the first that I

was directly involved with, and I am thankful to him for introducing me to the workings of the lab. Soon after, I began working with Matt Cashen, as he was finishing the last stages of his thesis. His setup would become my own, and he set me on solid footing for taking it over. I am also thankful for Matt's friendship and continued support after his leaving Stony Brook.

Jörg Bochmann's arrival in the lab came with perfect timing, as the collimation experiments were really gaining momentum. I am thankful to him for those late nights and weekends in the lab when I could not have run the experiment on my own and also for the many discussions and challenges about the experiment outside the lab. As he is getting ready to finish at Würzburg and head to the Max-Plank-Institut I wish him all the best of luck. As our research interests are not branching too far apart, I look forward to any future collaborations we might have, either in the lab or the biergarten.

Xiyue Miao has also been involved with the collimation experiments for some time, and I am thankful to her for all of her help, coping with my frustrations, and forcing me to be able to explain my work well to other students. She and Matt Eardley have already made good progress on taking the experiment over from me, and will be steering it in a variety of exciting directions. I wish them success and hope they keep me updated with their progress. I must also thank Matt E. for helping me with all things "computer", and warn him that

he might not graduate until another “Matt” joins the lab.

It has been a pleasure getting to know and work with the other current members of the group. Oleg Kritsun and Olexiy Boyko have taught me much on experimental technique as well as their homeland, Ukraine. Seung-Hyun Lee is as dedicated in the lab as he is as a husband and father and I hope our two families may continue to be friends in the future. Claire Shean rounds out the group with her energy and enthusiasm.

The Physics Department and Stony Brook campus are staffed with many skilled and knowledgeable people, without whom none of the research performed in the labs would ever be possible. Linda Dixon provides immeasurable assistance in keeping the group organized and in good working order. Sal Natale gets our packages to us before we expect them. The staff of the machine shop are top notch. I wish to extend thanks to Rich Yoepp, Walter Schmeling, and Bill Shilling. Mark Jablonski was always willing to help design a project and taught me most of what I know of machining. Jeff Slechta helped me design the new source chamber, and did a marvelous job with the welding. Pete Davis knows everything, and has been extremely helpful with the ATL. Bruce Gutschow provided us a good deal of assistance with the turbo pumps. Bob Segnini performs the amazing feat of keeping the physics building from falling apart or sinking into the ground. The staff of the Department Main

Office is the most friendly *and* capable that I have ever met. Pat Peiliker is the guardian angel of all physics graduate students.

Of course, no human being can work 24 hours a day, 7 days a week, and several good friends dragged my brain, or at least my body, out of the lab when it needed it. Stu Silverberg, Bill Jaffee, Victor Santiago, Heather Mann, Andrew and Michelle Steiner, John and Melanie Wilson, Yusuf Kinkhabwala, Scott and Lisa Craig and many others have given me many fond memories of my time here.

I would also like to thank 22 Riverhead Road in Sound Beach.

Lastly, and most importantly, I would like to thank my wife, Jennifer. Without her, none of this would have been possible. Her love, patience, support, and understanding have been a guiding light to me on this journey. May she shine forever in my eyes, and our family be equally as bright.

Chapter 1

Introduction

The field of laser cooling and trapping may well be a quarter century old, depending upon the point from which one starts counting. The first proposals for using the radiation scattering force for the cooling of atoms were made in the mid-to-late 1970's [1–3] and by the early 1980's several laboratories were pursuing experimental applications of these ideas [4–7]. Since then, laser cooling has become a major subfield of atomic, molecular, and optical physics. The techniques have been extended well beyond those of the early experiments, and cold atoms are used in both fundamental research and practical applications, from the study of Bose-Einstein condensation to quantum information processing to nanoscale neutral atom lithography [8].

As the field has developed, so too have comprehensive sources in the literature that give a broad picture of the field [8–10]. This introductory

chapter will present several key concepts of laser cooling that will provide a backdrop for the unique nature of the bichromatic force.

1.1 Radiative Force

The simplest situation that leads to an optical force on an atom is that of a two-level atom subjected to a monochromatic light field. No atom is truly a two level atom, but one can be approximately two-level when the monochromatic field strongly couples only two of the internal electronic states of the atom, typically the ground state and a low lying excited state, which can be labeled $|g\rangle$ and $|e\rangle$. The two states are separated in energy by $\hbar\omega_a$, the atomic resonance frequency, and are coupled by the monochromatic laser field, with photon energy $\hbar\omega_\ell$, which may be detuned from the resonance frequency by $\delta \equiv \omega_\ell - \omega_a$ as shown in figure 1.1. When the laser frequency is close to resonance, the atom may be excited by absorption of a photon to the excited state. Since the photon of energy E has momentum of E/c, the atom receives a momentum "kick" of $\hbar\vec{k}$, where $|\vec{k}| = k \equiv 2\pi/\lambda$ is the wavenumber of the light field. This is shown in the first two steps of figure 1.2. If the light is of low enough intensity, stimulated emission can be ignored, and the atom will eventually decay back to the ground state via spontaneous emission at a rate give by $\gamma \equiv 1/\tau$, where τ is the excited state lifetime. The spontaneous

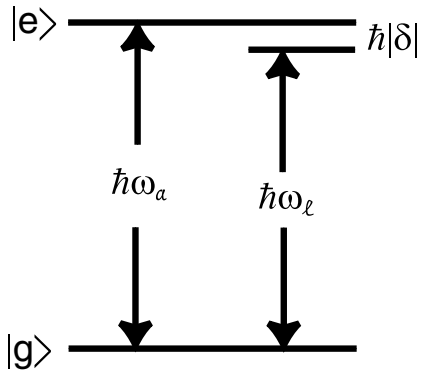

Figure 1.1 Simplified energy levels of the two level atom. The ground $|g\rangle$ and excited $|e\rangle$ states are separated by $\hbar\omega_a$. Laser light couples the two states, and can be detuned from the resonance by $\delta \equiv \omega_\ell - \omega_a$.

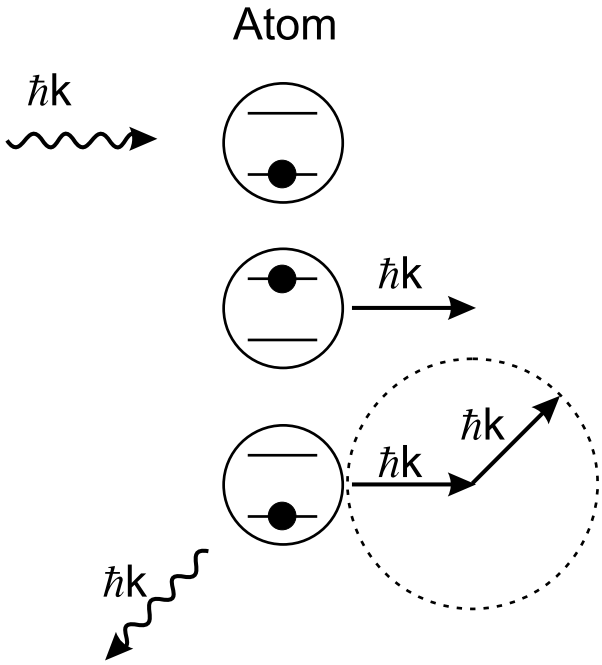

Figure 1.2 The steps of the cycle that produces the scattering or radiative force. The top picture is just a two-level atom in a monochromatic laser light field. The atom is excited by absorption and receives a momentum kick $\hbar\vec{k}$. Spontaneous emission is spatially symmetric and after many repeated cycles, the associated momentum kick averages to zero.

emission gives the atom another kick, in a direction directly opposite to the random direction of the emitted photon, as shown in the third step of figure 1.2. With the atom back in the ground state, the process then repeats. Over many cycles, the random nature of the spontaneous emissions causes their contribution to the momentum change of the atom to be averaged to zero. Thus, the net change in momentum is due only to the momentum kicks from the absorbed photons. The net force on the atom depends on how frequently this process happens in a given length of time:

$$F_{rad} = \hbar k \gamma_p \tag{1.1}$$

where γ_p is the total scattering rate of light from the laser field [8]:

$$\gamma_p = \frac{s\gamma/2}{1 + s + (2(\delta + (-\vec{k} \cdot \vec{v}))/\gamma)^2} \tag{1.2}$$

Here several key parameters have been introduced. The saturation parameter, s, is the ratio of the intensity of the laser field to the saturation intensity:

$$s \equiv \frac{I}{I_{sat}} \quad \text{with} \quad I_{sat} \equiv \frac{\pi h c}{3\lambda^3 \tau} \tag{1.3}$$

Typical values of the saturation intensity for atoms used in laser-cooling are several mW/cm^2. However, for the transition of interest in helium, the saturation intensity is only ~ 0.17 mW/cm^2, with $\lambda = 1.083$ μm and $\tau = 98$ ns ($\gamma = 1/\tau = 2\pi \times 1.6$ MHz). Also in equation 1.2 the Doppler shift, $-\vec{k} \cdot \vec{v}$,

of the light field as "seen" by a moving atom has been incorporated into the detuning of the light field.

Increasing the intensity of the light field will increase this scattering rate, up to a certain point. For $s \gg (\delta/\gamma)^2$ the scattering rate saturates to $\gamma/2$ so that the scattering force, also called the radiative force, saturates to a magnitude of

$$F_{rad,max} \equiv \frac{\hbar k \gamma}{2} \tag{1.4}$$

(resulting in typical values for $F_{max}/mg \sim 10^5 - 10^6$). The saturation of the force can be understood in a simple manner. As the intensity of the light increases, so does the possibility of the excited atom to decay to the ground state via stimulated emission. The rate of stimulated emission can become much greater than the rate of spontaneous emission. However, each stimulated emission gives the atom a kick in the direction opposite of the emitted photon, and since the emitted photon has the same $\vec{k}$ of the absorbed photon, the two kicks cancel each other out. Thus, absorption followed by stimulated emission does not contribute to the radiative force, and therefore, the magnitude of the force is fundamentally limited by the spontaneous decay rate.

It should be noted that the range of atomic velocities over which the force is strong is also limited. A moving atom will be Doppler shifted away from

resonance, reducing the scattering rate (see equation 1.2). Considering the on-resonance case ($\delta = 0$) and low intensity, the radiative force is only significant over a range $\sim \pm\gamma/k$ of atomic velocities, with γ/k being on the order of several m/s for atoms of interest to laser cooling. However, by changing the detuning of the laser, δ, to compensate for the Doppler shift, a faster moving atom can be resonant with the laser light.

1.2 Optical Molasses

Consider an atom moving in a light field that is "red-detuned" from resonance (i.e. $\omega_\ell - \omega_a = \delta$ is negative). Due to the combined Doppler shift and negative detuning, the atom will be more likely to absorb light if it has a velocity opposite to the direction of $\vec{k}$. That is, the atom will experience a force that opposes its direction of motion (as long as $v \lesssim \delta/k$). Adding another red-detuned, counter-propagating beam will impose a force with similar properties on atoms with the opposite velocity. In the low intensity limit, the forces from the two counter-propagating beams can simply be added together:

$$\vec{F}_{OM} = \hbar\vec{k}\frac{\gamma s/2}{1+s+(2(\delta+(-\vec{k}\cdot\vec{v}))/\gamma)^2} + \hbar(-\vec{k})\frac{\gamma s/2}{1+s+(2(\delta+(\vec{k}\cdot\vec{v}))/\gamma)^2} \tag{1.5}$$

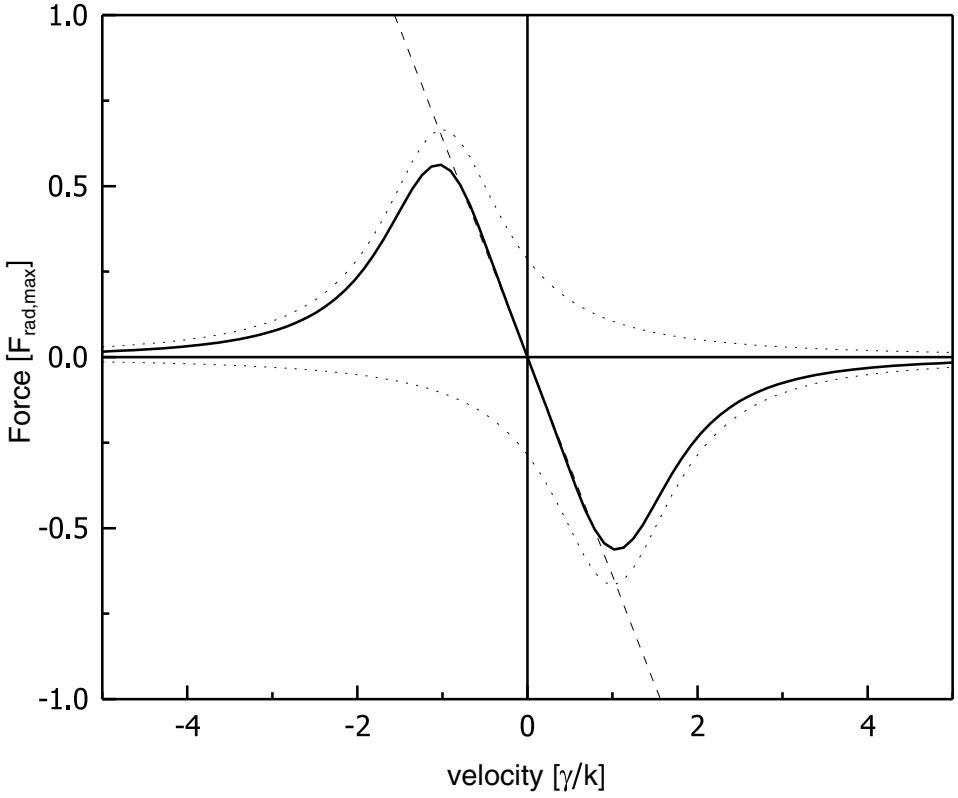

Figure 1.3 The force dependence of the optical molasses that results from two counter-propagating red-detuned laser beams. The two dotted lines show the force due to each individual beam, and the solid line is the combined force. The linear dashed line has slope $-\beta$. The force is calculated for $s = 2$ and $\delta = -\gamma$.

Note the change of signs between the two halves of the equation, due to the two counter-propagating beams having opposite $\vec{k}$. In the limit of small velocities ($kv < \gamma, \delta$), such that terms of order $(kv/\gamma)^2$ and higher can be neglected, there is a linear approximation to equation 1.5:

$$\vec{F}_{OM} \approx \frac{8\hbar k^2 \delta s_0 \vec{v}}{\gamma(1 + s_0 + (2\delta/\gamma)^2)^2} \equiv -\beta\vec{v} \tag{1.6}$$

It can be seen that, in the small velocity limit, the force is always proportional

to, *and* opposes, the velocity of the atom. The factor β is termed the damping coefficient, and due to the viscous damping nature of this force, the force was given the name "optical molasses." Figure 1.3 illustrates the above equations. The factor β gives the characteristic damping time, m/β, typically $\sim 10^{-7} - 10^{-6}$ seconds.

This picture is not quite complete. With no other influence on the atomic motion than the damping force described above, all atoms in the field would be decelerated to $v = 0$ (i.e. cooled to $T = 0$). While the net momentum transfer to the atom from many spontaneous emissions is zero, the rms scatter around zero of these $\hbar k$ momentum kicks is not. The result of multiple random kicks via spontaneous emission is well described as a random walk in momentum space, leading to a diffusion in momentum space. The rms scatter, or velocity spread, of the atoms can be characterized by a diffusion coefficient, D_0. In the steady state, where this heating rate is equal to the cooling rate of optical molasses, Brownian motion theory gives the steady state temperature $k_B T = D_0/\beta$. For the ideal optical molasses case, $s \ll 1$ and $\delta = -\gamma/2$, this gives a final temperature of $T_D = \hbar\gamma/2k_B$, termed the Doppler temperature, or Doppler limit. For the typical atoms used in laser cooling experiments, namely the alkalis and metastable noble gases, these temperatures range from hundreds of μK to tens of μK. Experimental observation of temperatures below

this limit [11] necessitated the formulation of new theories.

1.3 Sub-Doppler Cooling with Multi-Level Atoms

The observation, in 1988 [11], of sodium atoms cooled to temperatures 10 times lower than the expected Doppler temperature came as an "enormous suprise" [8]. New theories were soon developed [12, 13] to explain the lower temperatures. The crucial new feature was the incorporation of the multiplicity of the sublevels that make up any give atomic state, for example Zeeman sublevels and hyperfine structure. Optical pumping among the multiple levels, enabled by spontaneous emission, provides the main scheme in which additional energy is removed from the atom-field system. Sisyphus cooling in a light field with a polarization gradient [13] is one of the key examples. The "finger physics" explanation for these schemes is that of an atom moving through a spatially varying potential and in doing so gaining potential energy at the cost of kinetic energy. The additional potential energy gained is radiated away by spontaneous emission. An excellent introduction to the subject can be found in a 1990 *Physics Today* article by Cohen-Tannoudji and Phillips [14]. The magneto-optical trap (MOT) and velocity-selective coherent population trapping (VSCPT) are other methods of optical manipulation of atomic motion utilizing these multiple level schemes. The text by Metcalf and

van der Straten [8] illuminates the finer points of sub-Doppler laser cooling as well as provides a comprehensive list of references. Unfortunately, the forces in these sub-Doppler processes are limited in both magnitude and capture range to that of the Doppler cooling of optical molasses or even less. Hence, they are not of immediate use to the goals of this experiment, where a large force over a large velocity range is needed to slow and/or collimate a thermal atomic beam.

1.4 Dipole Force

The counter-propagating beams of the optical molasses arrangement combine together to form an optical standing wave. The spatial variation of the standing wave intensity causes a spatial variation of the energy levels of the two-level atom. This arises from the light shift due to the coupling of the two states by the light field. For an atom in the ground state, and for the simplified case of a laser far detuned from resonance, the light shift is given by [8]:

$$\Delta E_g = \frac{\hbar \Omega_r^2}{4\delta} \tag{1.7}$$

Here, Ω_r is the Rabi frequency for each of the beams and is related to the saturation parameter by:

$$|\Omega_r| = \gamma\sqrt{\frac{s}{2}} = \gamma\sqrt{\frac{I}{2I_{sat}}} \tag{1.8}$$

Choosing a generic form of $I(z) = I_0 \cos^2(kz)$ for the intensity of the standing wave, the dipole force on the atom is then given by the gradient of the energy levels:

$$F_{dip} = -\frac{\partial}{\partial z}\Delta E_g = -\frac{\partial}{\partial z}\left(\frac{\hbar\gamma^2}{8\delta}\frac{I}{I_{sat}}\right) = \frac{\hbar k\gamma^2 I_0}{8\delta I_{sat}}\sin(2kz) \tag{1.9}$$

In contrast to the radiative force, the dipole force is not limited in magnitude by the excited state decay rate, and can be made to be quite large by increasing the laser intensity (as long as $|\delta| \gg |\Omega_r|$ [8]). It is analogous to the force on a classical dipole in an inhomogeneous electric field. However, the sign of the force changes with the period of the standing wave, and thus the force vanishes in a spatial average over the optical wavelength.

A more rigorous treatment of the dipole force reveals several ways in which a non-vanishing wavelength-averaged force can occur as a consequence of atomic motion. However, both a version of the Sisyphus effect [15] and multi-photon "Doppleron" resonances [16] are limited in both magnitude and velocity range.

1.4.1 Rectified Dipole Force

The potential magnitude of the dipole force illustrated by equation 1.9 makes it an attractive tool for manipulating atoms. Several schemes have been proposed to spatially "rectify" the dipole force on the wavelength scale[17, 18]. One possible way to do this is to use *two* standing waves, each of a different frequency, with one field close to resonance creating a large dipole force, and the other detuned far off resonance which serves to provide a modulation of the atomic transition frequency, altering the detuning of the first field.

The description of the force begins with the simplifying condition that:

$$|\delta_2| \gg \Omega_2, \Omega_1, |\delta_1|, \gamma \tag{1.10}$$

where subscripts 1 and 2 denote the parameters of the two different standing waves of different detunings and intensities. In a monochromatic standing wave of detuning δ_1 and Rabi frequency Ω_1, the dipole force can be written as [19]:

$$F(r) = -\frac{1}{2}\hbar\gamma \frac{\delta_1/\gamma}{\delta_1^2/\gamma^2 + 1 + s_1(r)} \nabla s_1(r) \tag{1.11}$$

where $s_1(r) = I_1(r)/I_{sat}$ is the position-dependent saturation parameter. A second, strongly detuned (i.e. condition of equation 1.10) standing wave is applied, and the rectified force in the bichromatic field can be found from equation 1.11 by adjusting the detuning of the first standing wave, replacing

it with [17, 20]:

$$\delta_{eff}(r) = \delta_1 + \gamma^2 s_2(r)/\delta_2 \tag{1.12}$$

Making this modification takes into account the position-dependent light shift of the atomic transition induced by the second field. Note that this is only possible with the initial condition of equation 1.10, otherwise, one would have to take into account the contribution to the dipole force of the second field. Figure 1.4 shows an example where the parameters are set such that the effective detuning oscillates about zero.

Due to the difference in detuning between the two standing waves, there is a slowly varying spatial phase shift between them: $\phi = 2z|\delta_1 - \delta_2|/c$ which can be considered constant over many optical wavelengths. With proper choice of this phase, the sign reversal of the effective detuning due to the second field can be set to exactly compensate for the sign reversal due to the intensity gradient (see figure 1.4) and thus have a non-zero spatial average.

The rectified dipole force has been investigated with several experiments [20–22], resulting in a magnitude of force several times the radiative limit. However, due to the condition 1.10, the frequencies have to be fairly well specified. The weakness of the rectified dipole force is that the mechanism can only tolerate small Doppler shifts (the effective detuning may no longer oscillate about zero in the frame of a moving atom), which limits the velocity

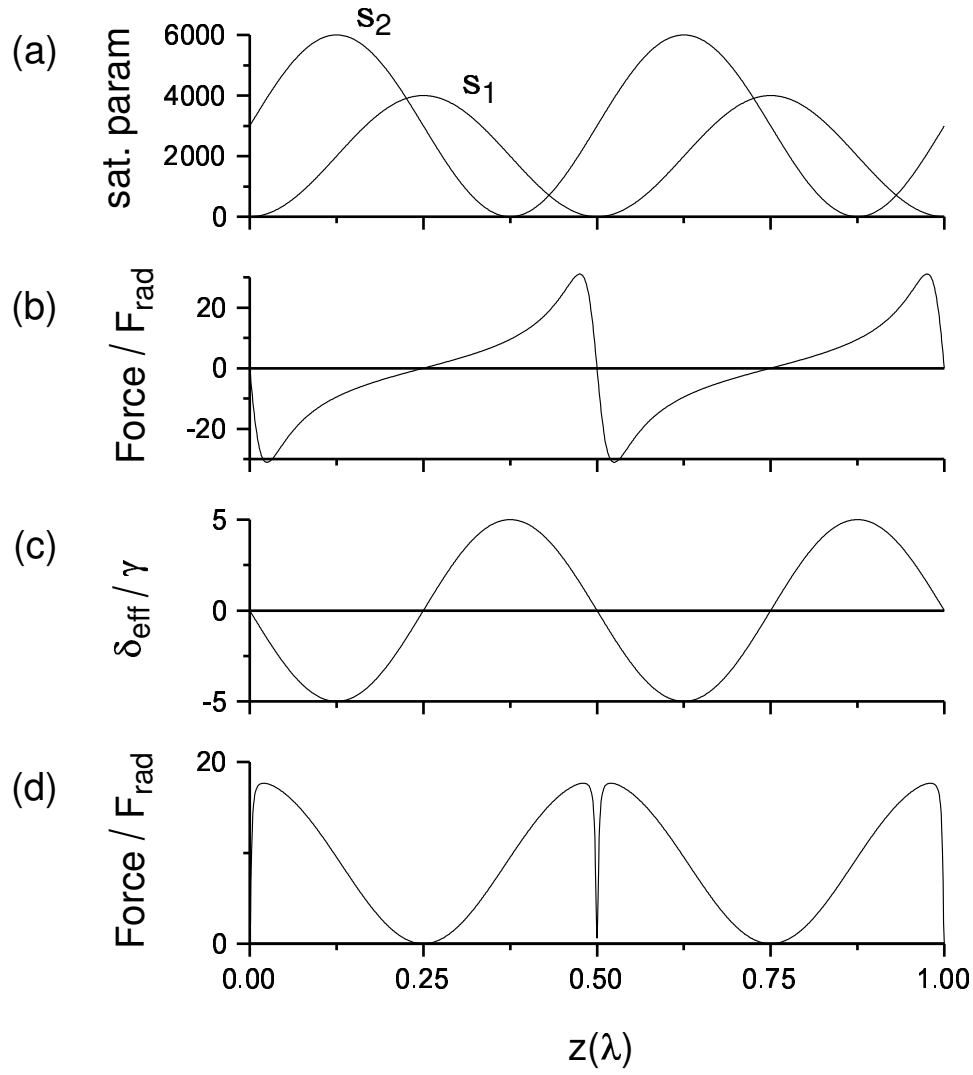

Figure 1.4 The rectified dipole force. The parameters used here are $\delta_1 = 5\gamma, \overline{s}_1 = 2000, \delta_2 = -150\gamma, \overline{s}_2 = 3000, \text{and} \phi = \pi/2$. Plot (a) shows the intensity profiles of the two standing waves. Plot (b) shows the non-rectified dipole force due to the first standing wave alone. Plot (c) is the effective detuning of the resonance induced by the second standing wave. Finally, plot (d) is the rectified dipole force.

range of the force. Fortunately, a different approach with bichromatic fields yields dramatically different results.

Chapter 2

The Bichromatic Force

The bichromatic force can be considered a special case of the rectified dipole force. Indeed, the bichromatic force was initially developed as an extension of the dipole force. However, the description given in the previous chapter for the rectified dipole force cannot be applied to the bichromatic force, due to the choice of detunings and intensities of the two frequencies, and the contribution to the force from the second frequency cannot be ignored.

The bichromatic force overcomes the limits of the radiative force by the coherent control of momentum exchange between the atoms and the laser field brought about by frequent sequences of absorption followed immediately by stimulated emission. However, spontaneous emission is not eliminated, and does play a role in creating a non-vanishing force.

2.1 π-Pulse Model

The bichromatic force occurs for a very particular choice of parameters for light comprised of two frequencies. A bichromatic light beam with two frequency components symmetrically detuned about atomic resonance by $\pm\delta$ (difference frequency $= 2\delta$), and each component having equal intensities, can be written as:

$$E = E_0 \cos[(k + \Delta k)z - (\omega_a + \delta)t] + E_0 \cos[(k - \Delta k)z - (\omega_a - \delta)t] \quad (2.1)$$

where ω_a is the atomic resonance frequency, $k = \omega_a/c = 2\pi/\lambda$, and $\Delta k = \delta/c$. With a regrouping of terms, equation 2.1 can be rewritten:

$$E = 2E_0 \cos(kz - \omega_A t) \cos(\delta t - \Delta k z) \quad (2.2)$$

This has the form of an amplitude modulated traveling wave, with carrier frequency at the atomic resonance, ω_a, and with modulation (or "beat") frequency δ. If the Rabi frequency

$$|\Omega_r| \equiv \gamma\sqrt{I_0/2I_s}, \quad I_0 \propto |E_0|^2 \quad (2.3)$$

of each frequency component is properly chosen for a given δ, then the envelope of each beat can act as a π-pulse for the atoms.

This π-pulse model of the bichromatic force was first proposed by Voitsekhovich et al. [18, 23] and is the most intuitive description of the force. A

π-pulse inverts the atomic population of a two-level atom by coherently driving ground-state atoms to the excited state and vice-versa. The term "π-pulse " comes from the Bloch vector picture, in which a vector $\vec{R}$ describes the state of the two-level atom [8, 24]. A pulse that takes the atom from the ground to excited state rotates the Bloch vector by π radians. The π-pulse condition for each bichromatic beat can be found from [24]:

$$\int_{-\pi/2\delta}^{\pi/2\delta} 2\Omega_r \cos(\delta t) dt = \pi \tag{2.4}$$

with each beat having a period π/δ. Equation 2.4 yields the condition:

$$\Omega_r = \frac{\pi}{4}\delta \tag{2.5}$$

When this condition is satisfied, the amplitude modulated bichromatic beam becomes a series of π-pulses , as shown in figure 2.1 (for experimental consideration, recall that $I \sim \Omega^2$ as in equation 2.3 and so with a chosen bichromatic detuning of 60 MHz, the π-pulse condition requires intensity of the bichromatic beam of $s \sim 4000$). Inserting a retro-reflecting mirror after the light beam interacts with atoms creates the situation where an atom sees π-pulses arriving from opposite directions. In figure 2.1, the first π-pulse from the left causes excitation to the excited state as well as a momentum transfer of $\hbar k$ along the direction of pulse propagation. The following retro-reflected pulse from the right causes stimulated emision, returning the atom to the ground state, and

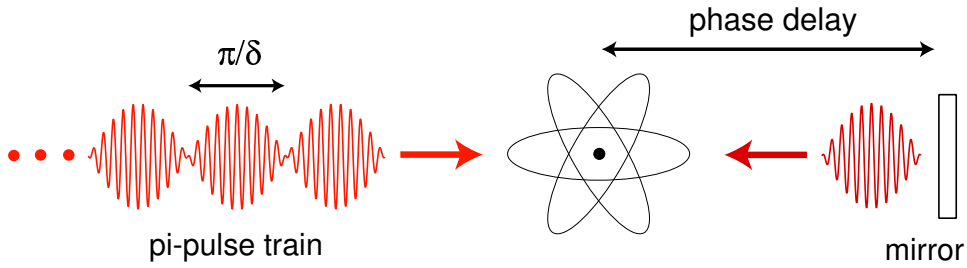

Figure 2.1 Simple scheme for coherent momentum transfer using bichromatic "pulses." The position of the mirror serves to set a phase delay between the arrival of the counter-propagating beats.

a momentum transfer along the same direction of the first momentum transfer (opposite in direction to the stimulated emitted photon). This yields a total momentum transfer from the light field to the atom of $2\hbar k$. The process is then repeated, with an excitation by a pulse from the left. This sequence of momentum kicks is not unperturbed by spontaneous emission, but if the repetition rate, δ/π, is chosen to be much greater than the decay rate $\gamma \equiv 1/\tau$, many of these sequences can occur between spontaneous emissions. This results in a force which has magnitude:

$$F_B = \frac{\Delta p}{\Delta t} = \frac{2\hbar k}{\pi/\delta} = \frac{2\hbar k\delta}{\pi} \gg F_{rad,max} = \frac{\hbar k\gamma}{2} \tag{2.6}$$

The force is independent of γ, as the rate of momentum exchange is set by δ.

Of course, spontaneous emission cannot be ignored. Each spontaneous emission returns the atom to the ground state so that absorption rather than stimulated emission occurs with the next π-pulse , and thus switches the direction of the force produced by the counter-propagating π-pulse process. When

the arrival of the counter-propagating beats are spaced evenly in time there is $\pi/2\delta$ between each pulse (beats are spaced by π/δ in a given travelling wave). In this situation, multiple spontaneous emissions will cause there to be no preferred direction of the force, and the average force will be zero. A non-vanishing force occurs when the arrival time between pulses is arranged to be asymmetric, such as having the pulse from the right (from of the mirror in figure 2.1) arriving shortly after the pulse from the left. The shorter time interval between pulses reduces the likelihood of an unwanted spontaneous emission. If spontaneous emission were to occur between the two closely spaced pulses, and thus switch the direction of the force, the longer time before the next arrival of a pulse from the left increases the likelihood of another spontaneous emission that would correct the direction of the force. Numerical calculations have found the optimum delay between the counter-propagating beats is $\sim \pi/8\delta$ or $\phi = \pi/2$, where the length in time of one beat is equivalent to 2π phase in the intensity of the travelling wave (so in the symmetric case, the phase delay between pulses is π). The choice of $\phi = \pi/2$ is a tradeoff between maximizing the asymmetry and minimizing the beat overlap (which falls outside the description of the π-pulse model), as well as dependent on the choice of δ and Ω_r. Figure 2.1 also illustrates how this phase can be set by simply changing the optical path length of the retro-reflected beam. With this choice of phase,

the atoms typically spend 1/4 of their time cycling with momentum "kicks" to the right and 3/4 of their time receiving "kicks" to the left. Thus the average force is reduced from equation 2.6 by a factor of two:

$$F_B = \frac{\hbar k \delta}{\pi} \tag{2.7}$$

which is still much greater than the radiative force, and can be made arbitrarily large by increasing δ. Note that, in the above picture, if the phase is changed to $\phi = 3\pi/2$ the direction of the force changes sign.

Being the most intuitive model, several effects are left out of the π-pulse picture. One is the temporal overlap between pulses, as the pulse width and repetition rate are interrelated (i.e. they are really beats, not pulses). Also, the π-pulse condition of equation 2.4 is for light that is exactly on resonance, so that the π-pulse condition is not satisfied for a moving atom that is Doppler shifted out of resonance.

2.2 Doubly Dressed Atom Picture

Another model that can be used to describe the bichromatic force is the doubly dressed atom picture (DDA) [25–27]. In this model, the four components of the bichromatic field (two in each direction and two frequencies) are paired differently than in the π-pulse model. Here, oppositely propagating

beams with identical frequency are paired together to form spatially different standing waves (as in the rectified dipole force). This can be written in a similar way as equation 2.1 yet containing all four components:

$$E = 2E_0 \left(\cos[kz + \chi/2]\cos[(\omega_A + \delta)t] + \cos[kz - \chi/2]\cos[(\omega_A - \delta)t]\right) \quad (2.8)$$

where the standing waves are spatially out of phase by $\chi = 2\Delta kz = 2\delta z/c$. Also note that $\chi = \phi/2$ since intensity has twice the spatial frequency of the electric field.

As suggested in the π-pulse model, $\delta \gg \gamma$ is required for a large bichromatic force, and Ω_r (the Rabi frequency of each component of the field) needs to be scaled proportionately large as well. The Rabi frequency Ω_r characterizes the light-induced coupling between the ground and excited state of the two-level atom. Such large required values of Ω_r suggests that one should take into account the energy levels of the combined system of atom, laser field, and atom-laser interaction. The energy levels resulting from adding in the interaction term to the atom-field system are called "dressed states." The "dressed atom" model has been well developed for atom-laser interaction in a monochromatic standing wave [28], providing useful pictures for the interpretation of such effects as "Sisyphus" cooling in a blue-detuned standing wave [15]. The approach to dressing the states with the bichromatic field begins in a similar fashion.

The approach starts with enumerating the "undressed", uncoupled states which are simple product states of the bare atom and the light field. We can label the bare atomic states with the state of the light field as $|g, b, r\rangle$ and $|e, b, r\rangle$, where $|g\rangle$ and $|e\rangle$ are the ground and excited states of the atom, and b photons are in the blue-detuned standing wave mode ($\omega_a + \delta$) and r photons are in the red-detuned standing wave mode ($\omega_a - \delta$, also note that in this this r should not be confused with the subscript of Ω_r). The energies of these two undressed states are simply [25, 26]:

$$\begin{aligned} E_{g,b,r} &= (b + r)\hbar\omega_a + (b - r)\hbar\delta \\ E_{e,b,r} &= (b + r + 1)\hbar\omega_a + (b - r)\hbar\delta \end{aligned} \tag{2.9}$$

These two uncoupled basis states each form a manifold that is itself an infinite ladder of equally spaced levels separated by $\hbar\delta$, as will be illustrated. The two manifolds themselves are separated by $\hbar\omega_a$, connected by a loss of energy from the atom-field system(i.e. spontaneous emission) as shown in figure 2.2. Within a manifold, an atom can be excited from $|g, b, r\rangle$ by the blue light to $|e, b - 1, r\rangle$ with an energy $\hbar\delta$ lower than that of $|g, b, r\rangle$, or by the red light to $|e, b, r - 1\rangle$ which has an energy higher by $\hbar\delta$. Either of these states may return to $|g, b, r\rangle$ by stimulated emission by the same field, or they can also return to the ground state, $|g, b - 1, r + 1\rangle$ or $|g, b + 1, r - 1\rangle$ respectively, by stimulated emission of light into the other beam, losing or gaining another $\hbar\delta$

of energy. This coherent process could continue, extending a given manifold infinitely in both directions.

The Hamiltonian $\mathcal{H}$ of the dressed states, including the atom-field coupling, can be written in the basis of the undressed states of a single manifold as a tridiagonal matrix [25, 27]. When truncated to 7×7, $\mathcal{H}/\hbar - (b+r)\omega_a$ looks like:

$$\begin{bmatrix} 3\delta & V_- & 0 & 0 & 0 & 0 & 0 \\ V_- & 2\delta & V_+ & 0 & 0 & 0 & 0 \\ 0 & V_+ & \delta & V_- & 0 & 0 & 0 \\ 0 & 0 & V_- & 0 & V_+ & 0 & 0 \\ 0 & 0 & 0 & V_+ & -\delta & V_- & 0 \\ 0 & 0 & 0 & 0 & V_- & -2\delta & V_+ \\ 0 & 0 & 0 & 0 & 0 & V_+ & -3\delta \end{bmatrix} \tag{2.10}$$

where the off diagonal elements are the spatially dependent coupling parameters (see equation 2.8):

$$V_\pm = \Omega_r \cos(kz \mp \chi/2) \tag{2.11}$$

Recall that Ω_r is the magnitude of the Rabi frequency for each of the four individual components of the bichromatic field. It should also be noted that χ is slowly varying and can be considered constant over small distances, $z \ll c/2\delta$. Calculating the eigenvalues of the truncated matrix gives an approximation of

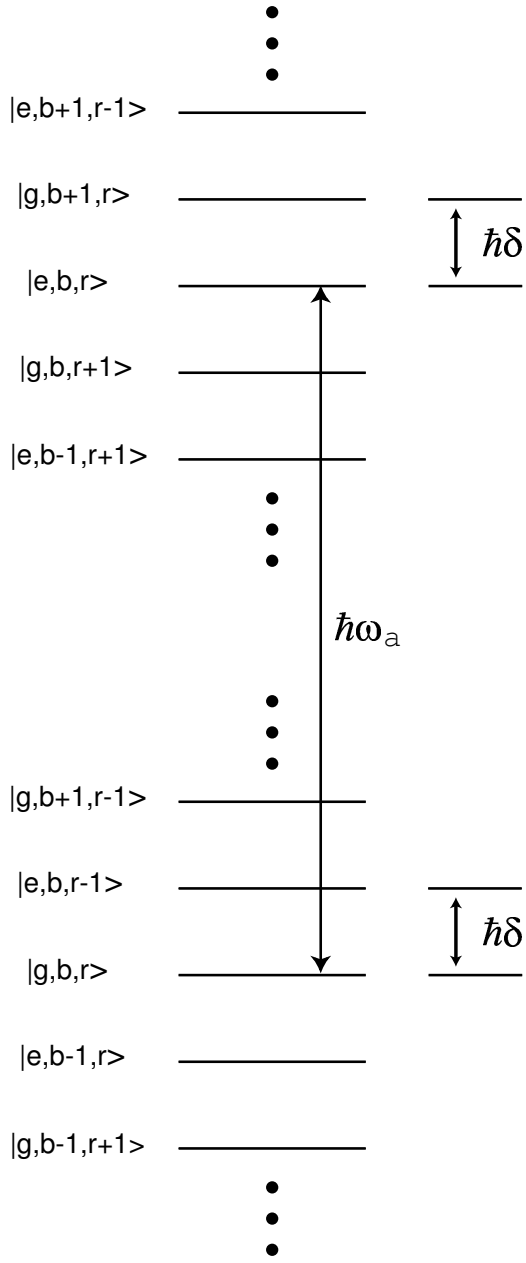

Figure 2.2 Schematic diagram representing the uncoupled energy levels of the combined atom-field states. Two manifolds are shown, the energies in each separated by $\hbar\delta$. The equal spacing is due to the symmetric detuning of the standing waves. Neighboring states are coupled by absorption or simulated emission from one of the standing waves, so that all states in each manifold are coherently coupled.

the position dependent dressed-state energies. Near the nodes of the standing waves, where the coupling from one of the fields is minimum, the energy levels show avoided crossings. Figure 2.3 displays the levels calculated from an 11×11 matrix for two different values of the Rabi frequency of each frequency component: the first is for the π-pulse condition, with $\Omega_r = \frac{\pi}{4}\delta$, and the second with $\Omega_r = \sqrt{\frac{3}{2}}\delta$ where it is found that the levels actually touch. These states can no longer be labeled with $|g\rangle$ and $|e\rangle$ as the fields of the two standing waves mix ground states with a component of the excited state and vice versa.

A moving atom has non-zero probability of moving diabatically through the avoided or real crossings, via a Landau-Zener transition. This probability can be modeled by [29, 30]:

$$P_{NA} = e^{-\pi U^2/\hbar v \nabla E} \tag{2.12}$$

where the subscript NA stands for non-adiabatic, $2U$ is the energy splitting at the avoided crossing, v is the velocity of the atom, and ∇E is the slope of the energy level approaching the crossing. When the the splitting at the avoided crossing becomes small, $P_{NA} \approx 1$. The path such a moving atom may take is shown by the bold line in (B) of figure 2.3. As the atom "climbs the Landau-Zener ladder," the atom-field system gains energy, energy which must come at the expense of the kinetic energy of the atom, through a coherent

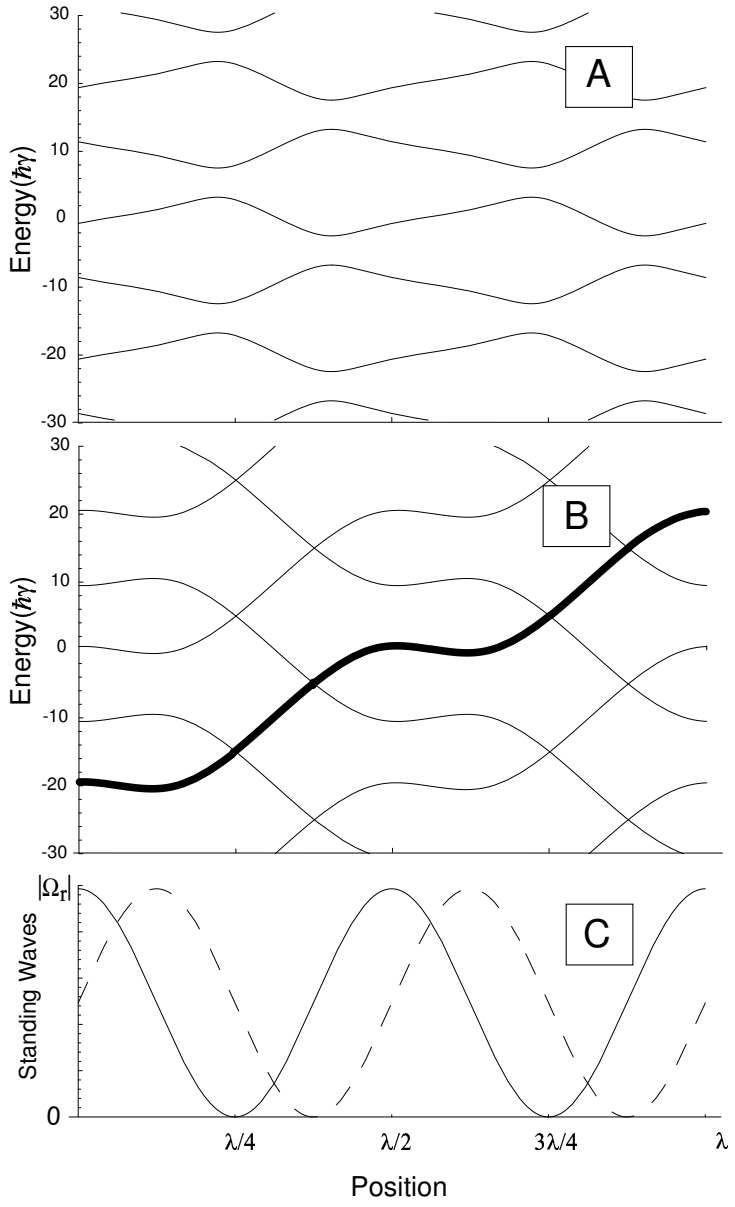

Figure 2.3 Spatial dependence of the approximated dressed state energy levels for the parameters $\delta = 10\gamma$ and $\chi = \pi/4$. In part (A) $\Omega_r = \frac{\pi}{4}\delta$, the π-pulse condition (eqn. 2.5). In part (B), $\Omega_r = \sqrt{\frac{3}{2}}\delta$. In part (C) the standing wave intensities are plotted. Note that the levels are equally spaced where the intensities of the two standing waves are equal. The spacing of the avoided crossings (that occur at the nodes of the standing waves) are large for $\Omega_r = \frac{\pi}{4}\delta$, while for $\Omega_r = \sqrt{\frac{3}{2}}\delta$ the crossings become real. The heavy line in (B) shows a possible path of an atom moving diabatically through the real crossings. It is paths such as this that give rise to the large bichromatic force.

conversion of photons from one standing wave field to the other. The average force on the atom is given by the average gradient of the energy change, and can be estimated from the slope of the bold line in figure 2.3:

$$|F| = \left|\frac{\Delta E}{\Delta z}\right| = \frac{20\hbar\gamma}{\lambda/2} = \frac{2\hbar k\delta}{\pi} \tag{2.13}$$

which is exactly the same as the initial estimate from the π-pulse model (equation 2.6)!

As in the π-pulse model, spontaneous emission must be included. Equation 2.13 only holds if an atom stays on the given manifold for the entire interaction time. Spontaneous emission will cause the atom to move to a lower manifold, and change the sign of the slope of the average change in energy (i.e. change the direction of the photon conversion between the fields). Figure 2.4 shows the calculation for the position dependent eigenvalues of the dressed states for the lower manifold of figure 2.2. In this figure, the bold lines represent energy levels that are a greater mixture of the bare atomic excited state. Therefore, an atom is more likely to undergo spontaneous emission while in this level than in the levels drawn with a thinner line. Analogous to the π-pulse model, the choice of χ determines the ratio of time the atom is in either type of state. In figure 2.4, an atom is more likely to follow path (b), since overall it has a smaller mixture with the excited state. If it were to undergo spontaneous emission to path (a), where the mixture with the excited state

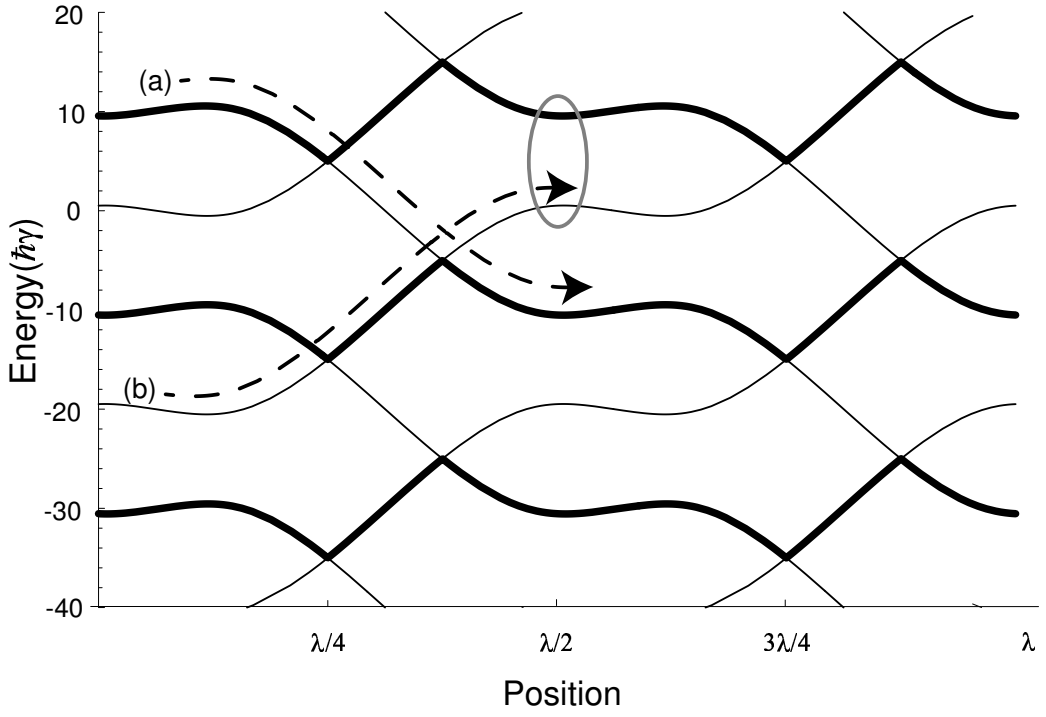

Figure 2.4 Two types of paths which could give rise to the bichromatic force. The bold lines indicate which levels have the greatest mixture with the excited state of the atom. In path (a), the overall path of the atom has greater mixture with the excited state and so is more likely to undergo spontaneous emission. The parameters used for the calculation were $\delta = 10\gamma$, $\chi = \pi/4$, and $\Omega_r = \sqrt{\frac{3}{2}}\delta$.

is greater, it has more time to undergo sponaneous emission again and return to path (b). Thus, with $\chi = \pi/4$, the atom spends 3/4 of its time on path (b) and 1/4 of its time on path (a), averaged over many spatial periods. The average force is then reduced to:

$$F_B = \frac{\hbar k \delta}{\pi} \tag{2.14}$$

which is the same result of the π-pulse model, except that in the DDA model the optimal choice of the Rabi frequency for each field component is $\Omega_r = \sqrt{\frac{3}{2}}\delta$.

The DDA model also suggests the origins of the limits on the velocity range of the force. An atom must have velocity such that it will diabatically move through the crossings as shown in the path of figure 2.4. The path drawn assumes that the atom adiabatically follows the energy levels in between these crossings. However, if the velocity is too large the atom will also experience Landau-Zener transitions at avoided crossings such as that indicated by the vertical ellipse in figure 2.4. This would cause the atom to experience no net force on average.

An approach to the dressed atom picture has been recently developed using a Floquet Hamiltonian ([31, 32]) by Yatsenko and Metcalf [27]. Here the time dependence of the system is removed by using a Floquet Hamiltonian whose fundamental time variation is the frequency difference, 2δ, between the standing waves. Not only does this approach analytically find the critical

Ω_r^{cr} for the avoided crossings to touch as well as the proper choice of χ for a given δ and $\Omega_r > \Omega_r^{cr}$, it also arrives at an upper limit to the velocity range of the force. This achieved in two ways, with a Landau-Zener estimate and analytically with a 2^{nd} order perturbation calculation, and the result is that the velocity range is $\pm\delta/4k$. However, this is not in agreement with some of the numerical calculations (to be discussed in the next section) which show the range can extend to $\pm\delta/2k$. This difference is believed to arise from the fact that the Floquet approach does not take into account the effect of atomic motion on the optical frequencies through the Doppler shift [27]. A second Floquet approach, in a reference frame moving at velocity $v_{ref} = \delta/2k$, is in development and is expected to explain this difference.

2.3 Numerical Calculation

The models only go so far in describing the physical origin of the bichromatic force, and are mostly qualitative in giving estimates of its magnitude and direction, as well as the optimal laser parameters, δ and Ω_r. An exact numerical calculation can provide much greater detail.

The calculation is performed with Fortran code originally provided by the authors of [25]. It has been well described in subsequent work [33–35] and will only be described briefly here.

In both of the presented models, the bichromatic force arises from multiple sequences of absorption to the excited state followed by stimulated emission to the ground state, coherently exchanging momentum between the atom and the light field. Thus it can be seen that accurate calculation of the force requires the inclusion of the relative populations of the states as well as how these populations change by stimulated and spontaneous emission. The Bloch vector [36] can be used to describe the internal state of the atom and the Optical Bloch Equations (OBE) are the equations of motion for the components of the Bloch vector.

With a transformation to a rotating frame (to remove the time dependance at the optical frequency, ω_a), the coefficients of the states of the two level atom can be combined to form the three components of the Bloch vector [36]:

$$\begin{aligned} r_1 &= c_g c_e^* + c_g^* c_e \\ r_2 &= i(c_g c_e^* - c_g^* c_e) \\ r_3 &= |c_e|^2 - |c_g|^2 \end{aligned} \tag{2.15}$$

where $|c_g|^2$ and $|c_e|^2$ are the populations of the ground and excited state. Then, leaving out many steps which are described in [8, 24, 28], the OBE for

a two-level atom in the bichromatic standing waves are:

$$\dot{r}_1 = -(\gamma/2)r_1 - \mathrm{Im}(\Omega_R)r_3 \tag{2.16}$$

$$\dot{r}_2 = -(\gamma/2)r_2 - \mathrm{Re}(\Omega_R)r_3$$

$$\dot{r}_3 = \mathrm{Im}(\Omega_R)r_1 + \mathrm{Re}(\Omega_R)r_2 - \gamma(r_3 + 1) \tag{2.17}$$

where the total field of the standing waves is included through the total Rabi frequency of the field: $\Omega_R(z,t) = -\vec{d} \cdot \vec{E}(z,t)/\hbar$. The force on an atom from the optical field can be dervied via the Ehrenfest theorem [37] and found to be:

$$F(z,t) = \hbar[r_1(t)\nabla\mathrm{Re}(\Omega_R(z,t)) - r_2(t)\nabla\mathrm{Im}(\Omega_R(z,t))] \tag{2.18}$$

While a velocity dependence does not directly appear in equation 2.18, a force *vs.* velocity profile can be obtained by inserting a velocity dependence through a "constant velocity appoximation" that gives the position of the atom as $z = vt$. The Fortran code calculates the force by solving equations 2.17 over small time steps and and evaluating equation 2.18 after each step.

Figure 2.5 shows several force profiles with intensities and detuning of experimental interest for this dissertation. The force profiles have previously been experimentally verified for a wide range of parameters [38, 39]. The calculations confirm that the maximum force for low velocity atoms does indeed occur when $\Omega_r = \frac{\pi}{4}\delta$, and not at the π-pulse condition, $\Omega_r = \sqrt{\frac{3}{2}}\delta$. The figure

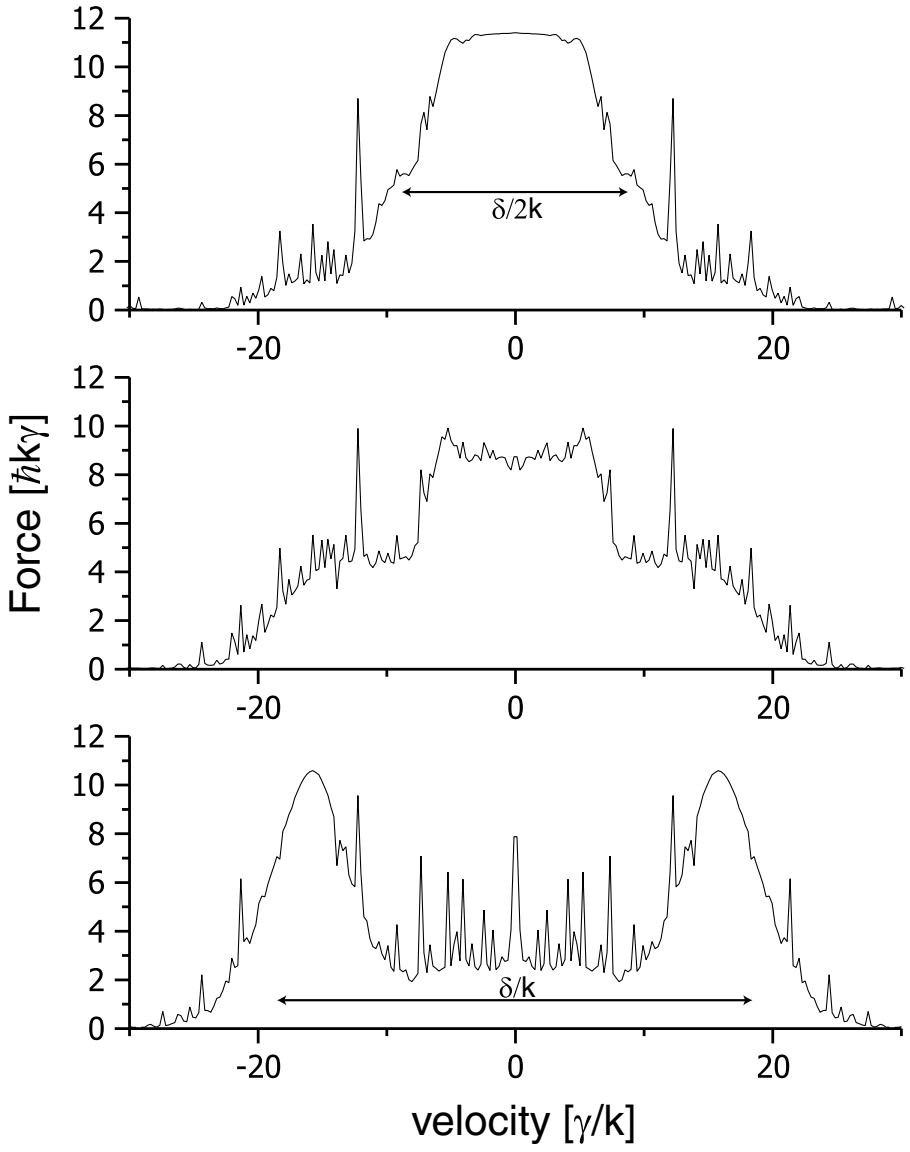

Figure 2.5 Calculated bichromatic force vs. velocity profiles for $\delta = 37\gamma$ and $\chi = \pi/4$ with various values of the Rabi frequency. In the top plot, $\Omega_r = \sqrt{\frac{3}{2}}\delta = 45\gamma$, in the middle $\Omega_r = 42\gamma$, and in the bottom $\Omega_r = 37\gamma$. Some of the sharp spikes are multiphoton resonances. Note the force axis is scaled by twice the radiative force, $F_{rad} = \frac{\hbar k\gamma}{2}$.

also shows the discrepancy of the force alluded to in discusion of the Floquet Hamiltonian approach to the DDA. The top plot shows the predicted range of the force, $\pm\delta/4k$. The bottom plot shows a range twice as large, which may be analytically verified with a second Floquet approach.

A strong force over the entire velocity range is possible experimentally, since the laser light used to create the bichromatic field can have a Gaussian (or other) intensity profile, such that as the atoms traverse the light beam, they "see" a changing Rabi frequency and thus a changing force, and the total force may be estimated by the average of the profiles shown in figure 2.5. This can give an estimate that demonstrates the usefulness of the bichromatic force. If an atom experiences a constant force of $\hbar k\delta/\pi$ as it is accelerated through a velocity range of δ/k, the time it takes for this acceleration is:

$$\Delta t = \frac{m\Delta v}{F} = \frac{m(\delta/k)}{(\hbar k\delta/\pi)} = \frac{\pi/2}{\omega_r} \tag{2.19}$$

which is independent of δ and only depends on the property of the atom (recoil frequency $\equiv\ \omega_r = \hbar k^2/2m$). For the transition of interest in Helium, the "bichromatic slowing time" is only $\Delta t = 5.9\ \mu$s, meaning that even with a fast beam of atoms (~ 1000 m/s), the interaction lengths can be under 1 cm.

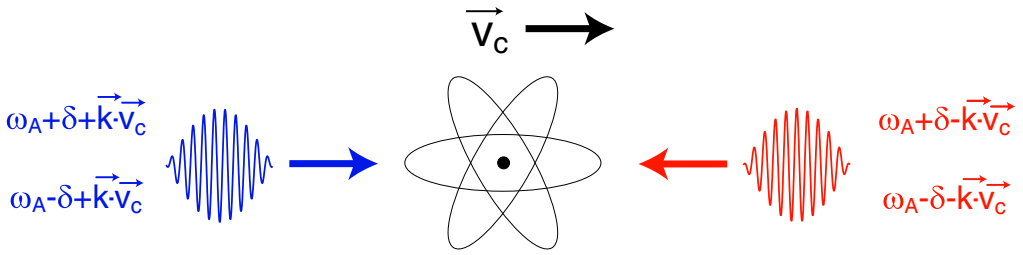

Figure 2.6 A representation of the scheme used to shift the center of the force profiles away from $v = 0$. In the frame of the moving atom, the four laboratory-frame fequencies become $\omega_a \pm \delta$.

2.4 Shifting the Center of the Force

Several aspects of the bichromatic force should be addressed before putting it to practical use. One is that the force is always positive (or negative, depending on χ) for all velocities. That is, the force can push in only one direction, unlike optical molasses. Another is that the force profile is centered around $v = 0$. In a collimation experiment, one would ideally want to collect atoms from both positive and negative velocities to $v = 0$. The first step in doing this is to shift the velocity center of the force. This is done by removing the mirror of figure 2.1 and adding a second independent counterpropagating amplitude modulated travelling wave. As shown in figure 2.6, the frequencies of the two travelling waves can be Doppler shifted (one up by "$+kv_c$"and the other down by "$-kv_c$") so that in the reference frame of an atom moving with velocity v_c the frequencies of each beam are $\omega_a \pm \delta$. Choosing $v_c = \delta/k$, the force is shifted so that the profile drops off sharply at $v = 0$. Note that

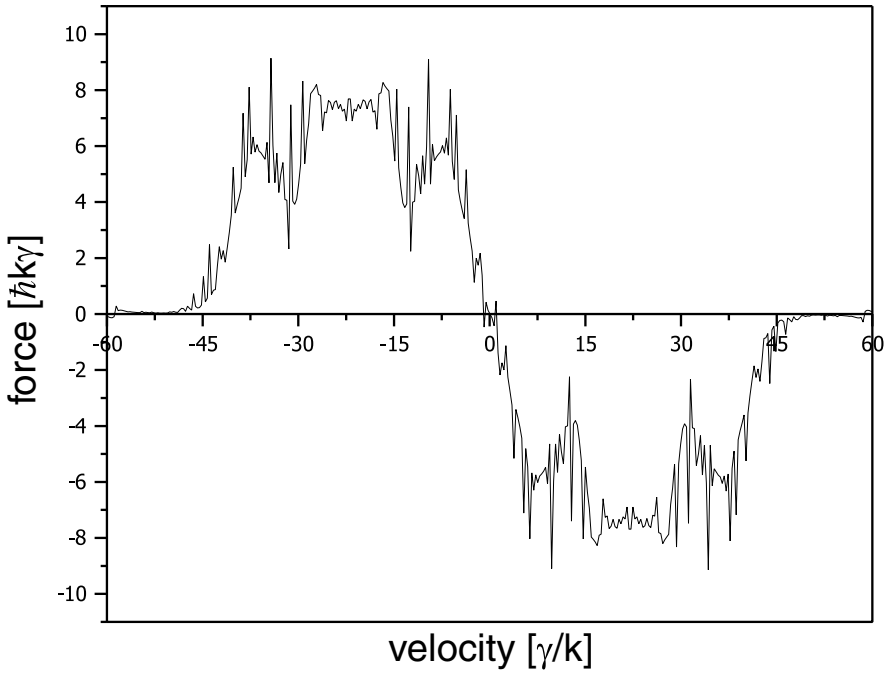

Figure 2.7 The bichromatic force vs. velocity profile calculated with parameters of experimental interest, $\delta = 37\gamma$ and $\Omega_r = 41\gamma$. Here two interaction regions (two sets of counter-propagating beams) are used to have the bichromatic force "simulate" an very strong optical molasses. The velocity range of an ordinary molasses is only a few γ/k.

when the beat nodes of "$-kv_c$"are $\phi = \pi/2$ ahead of those of "$+kv_c$", the the bichromatic push is in the direction of the propagation of "$-kv_c$".

Adding a second set of Doppler-shifted counter-propagating beams, spatially separated from the first, with opposite frequency shifts and opposite spatial phase ϕ results in a combined push to $v = 0$ from opposite directions, as shown in figure 2.7. The profile emulates the profile of an optical molasses, but has a much larger capture range and force magnitude. A description of how the bichromatic beams are produced follows in chapter 4.

Chapter 3

Metastable Helium Apparatus

The "two-level atom" used in these experiments is the Helium atom in the metastable 2^3S_1 state (He*). This excited state of He is metastable because decay to the ground state via an electric dipole transition is prohibited by the selection rules (electron spin cannot change *and* $\Delta L = \pm 1$). Here the Russell-Saunders notation $n^{2S'+1}L_J$ is used, except that we use S' instead of S to represent the total spin of the core *plus* valence electron. With a lifetime of $\sim$ 8000 s, the 2^3S_1 serves as the effective ground state of the "two level atom." The energy levels relevant to this experiment are shown in figure 3.1. Transitions to the first excited states, $2^3P_{J=0,1,2}$, are driven by a laser with $\lambda = 1083$ nm (this laser will be discussed in the next chapter). Note the lack of hyperfine states, since the Helium nucleus has no spin. This chapter discusses how we produce a beam of He*, and subsequently detect the atoms.

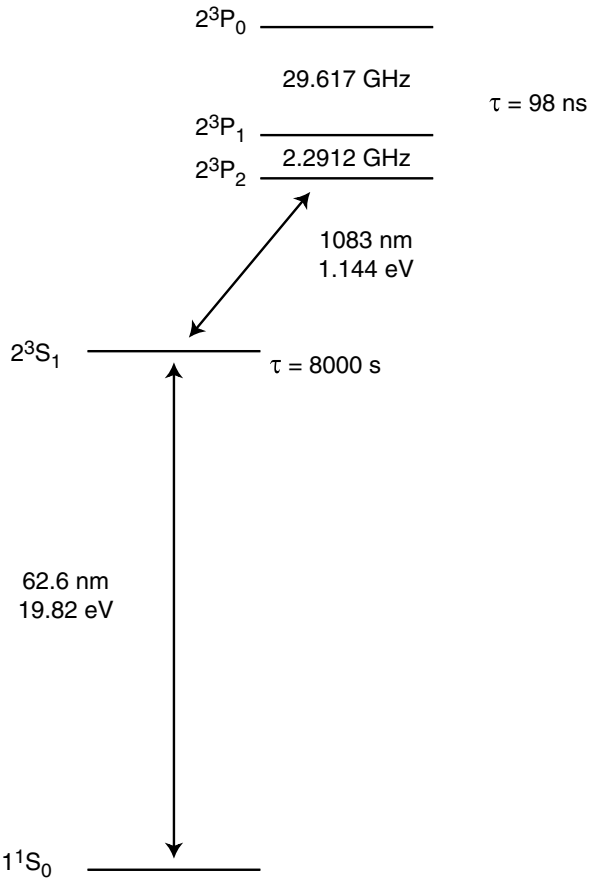

Figure 3.1 Energy level diagram for He* and the transitions of interest. (Note that the levels are not drawn to scale.)

Quantity Units	λ (nm)	$\hbar\omega_a$ (eV)	τ (ns)	$\gamma/2\pi$ (MHz)	I_{sat} (mW/cm^2)	$\omega_r/2\pi$ (kHz)
	1083.33	1.144	98.04	1.62	0.17	42.46

Table 3.1 Values for the various properties of the $2^3S_1 - 2^3P_2$ Helium transition used in this experiment, taken from [8].

3.1 Metastable Helium Source

The helium source that is currently in use in the lab was originally fabricated at Utrecht University in the Netherlands. It was then assembled and tested at Stony Brook by Matthew Cashen and Michiel van Rijnbach [35], and in good working order by the spring of 1999. Since then the source's primary use has been the investigation of polychromatic forces.

The metastable helium beam is produced by a DC glow discharge. The source design is based on that developed by Kawanaka et. al. [40] and slightly modified by the group at Utrecht [41, 42]. It is comprised of a 1 cm diameter pyrex glass tube, with a narrowed end, centered inside a stainless steel coaxial jacket, which is filled with liquid nitrogen (see figure 3.2). He gas flows into the vacuum chamber between the glass tube and the LN_2 filled jacket, and is thus cooled before entering the tip of the glass tube. A teflon spacer, which holds the end of the glass tube in place, further narrows the spacing and increases the contact between He atoms and the cold walls. Most of the atoms are then pumped away through the inside of the glass tube by a rotary-vane mechanical pump. Along the center of the glass tube is a 1 mm diameter tungsten rod with the end sharpened to a point, and held centered in place by a ceramic spacer (not shown). The spacer has several channels cut into it to allow appropriate flow of the helium gas away from the source region. In front of the glass tube

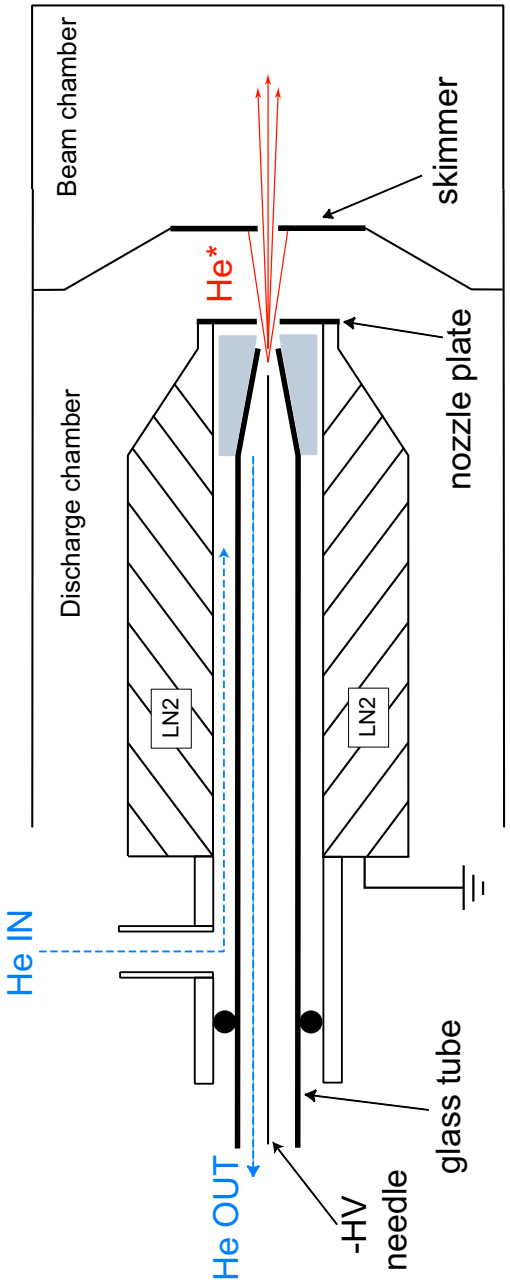

Figure 3.2 Cross sectional schematic of the DC discharge source for metastable helium. Ceramic spacer on tungsten wire not shown.

is an aluminum plate, called the nozzle plate, which has a 0.5 mm aperture and is connected to ground through the vacuum chamber. With proper gas flow, a negative high voltage (1 to 3 kV) is applied to the needle which creates a DC discharge between the needle (cathode) and the nozzle plate (anode).

In the resulting plasma, metastable atoms are produced by electron impact and/or ion-electron recombination. Unfortunately, most of these metastables are quenched by collisions in the dense plasma. Outside the plasma in the afterglow of the discharge, directly behind and past the nozzle plate, more metastables are created by collisions with secondary electrons. These atoms pass through the nozzle without passing through the main discharge region, and so are not heated or quenched by the plasma [40, 43]. However, the atoms in the metastable state make up only a small fraction ($\approx 10^{-5} - 10^{-4}$) [8] of the total number of He atoms in the beam. Besides electrons, ions, and visible light, the source also produces UV light (20 eV) resulting from the decay of the 2^1P_1 excited state (also produced in the discharge), and to a smaller extent the collision-induced decay of the metastable back to the ground state. The beam is formed from the atoms that fly through the nozzle plate rather than being pumped out through the glass tube.

The reliable production of a discharge and subsequent metastable beam depends on several factors. The discharge begins to run stably for discharge

currents above 2 mA. The discharge could be run up to 12 mA or higher, but by increasing the current, the discharge becomes "hotter", and the beam has a higher longitudinal velocity. We typically chose 6 mA as a trade-off between metastable production and velocity. Discharge operation also relies on the pressure of gas entering the region, and the speed at which it is pumped away. The inlet pressure can be adjusted with a fine needle valve, and would typically have pressures of 5 to 10 Torr. Running at lower pressures results in greater metatstable production, but also causes the discharge to become unstable. This pressure was measured by a Granville-Phillips Convectron Gauge placed in the helium gas inlet. The gauge was read by a Terranova Scientific Gauge Controller (Model 926). By default such devices are calibrated for nitrogen (air) so a conversion chart for other gases had to be acquired from Duniway Stockroom, the manufacturer of the controller. Also of importance is the sharpness of the needle and the general cleanliness of the glass tube and anode. Although the source has not been in operation long enough to provide a large enough sampling, it seems that the sharpening of the needle and cleaning of the parts need be done on the period of every two years. Running the discharge at high currents dramatically shortens this lifetime. Taking all the precautions described above, the source reliably produces an output flux of atoms $\approx 10^{14}$ He* atoms/s·sr. Proper production of metastable atoms can be assured by

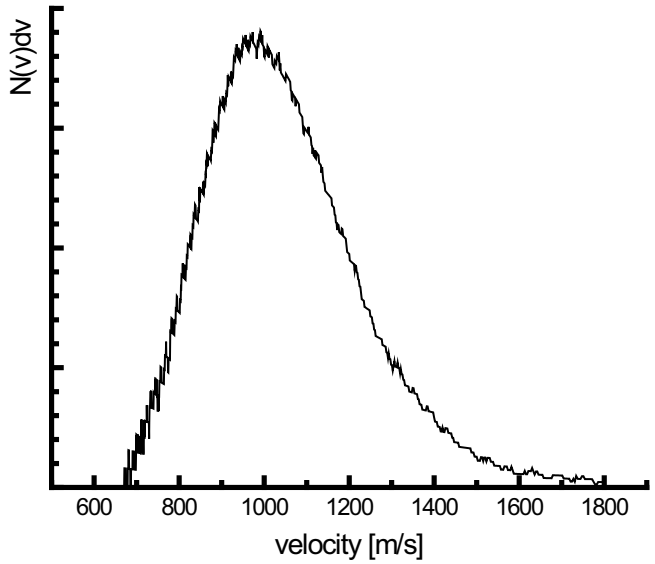

Figure 3.3 Metastable atom longitudinal velocity distribution with a discharge current of 6 mA.

monitoring the current and by viewing the color, intensity, and shape of the discharge glow.

The purpose of the liquid nitrogen jacket is to cool the atoms and nozzle plate such that the resulting beam has a reduced average longitudinal velocity and spread. The longitudinal velocity of the beam can be characterized by a time of flight (TOF) measurement. One way to do this is to use a mechanical chopper to pulse the beam. This method has the benefit of separating the atomic signal from the UV signal, which provides a zero point for time. TOF measurements for this source have been carried out for a wide variety of operating parameters [35]. The results were shown to be highly repeatable and were not remeasured for this thesis. At the source parameters used for these

experiments, the longitudinal velocity distribution is peaked at $\approx$ 1000 m/s with a FWHM of $\approx$ 400 m/s (figure 3.3). If the source were to be run at room temperature, longitudinal velocities would be peaked at $\approx$ 2500 m/s [44]. The source could also be cooled with liquid helium to produce even lower velocities ($\approx$ 300 m/s) [45]. The transverse velocity distribution will be discussed later in this chapter.

3.2 Metastable Helium Beam Chamber

As shown in figure 3.2, directly following the nozzle plate is a second plate with a 0.5 mm aperture, called the skimmer. The purpose of the skimmer is two-fold. First, to more geometrically define the beam, and second, to allow for differential pumping. With the discharge running, the pressure between the nozzle and skimmer is $\approx$ 10^{-4} Torr, while behind the skimmer the pressure remains several$\times 10^{-7}$ Torr (as measured by two ion gauges, both Kurt J. Lesker model# G100F). This region behind the skimmer is termed the beam chamber, and the low pressure is needed to reduce collisions between the metastable beam atoms and background gas, as collisions can cause decay back to the ground state. The distance between the nozzle plate and skimmer, as well as their mutual alignment, can be adjusted via a bellows which connects the source to the source chamber. The two apertures are typically separated

by about 0.5 to 1 cm. The source chamber (the area between the nozzle and skimmer), as well as the beam chamber are each pumped by a Pfeiffer model TPH 330 turbomolecular pump, backed by a Welch 1376 mechanical pump (refer to figure 3.4).

To do the collimation experiment a new vacuum system connecting the source to the beam chamber had to be designed and built. In the prior system, there was limited optical access near the skimmer. For the collimation to be most effective, optical access to the atomic beam was needed immediately as it entered the beam chamber, before it had expanded. A new chamber was designed so that the source and skimmer protruded into an area with considerable optical access. The main body of this new chamber was made of a tee welded to a 6-way cross, both of 4" outer diameter. The source was mounted through one arm of the tee and the beam chamber occupied the other arm. At the bottom of the tee the vacuum pump was attached. The next step of the design was to cut off the arm of the tee to the beam chamber, and to cut off one arm of the 6-way cross. These two cuts were then then welded together, so that the other two axes of the 6-way cross were at 45° to the horizontal plane and perpendicular to the beam line. In doing this weld, a wall was placed between the two sections. A large hole was machined into this wall, into which the fat end of a section cut from a conical reducer was

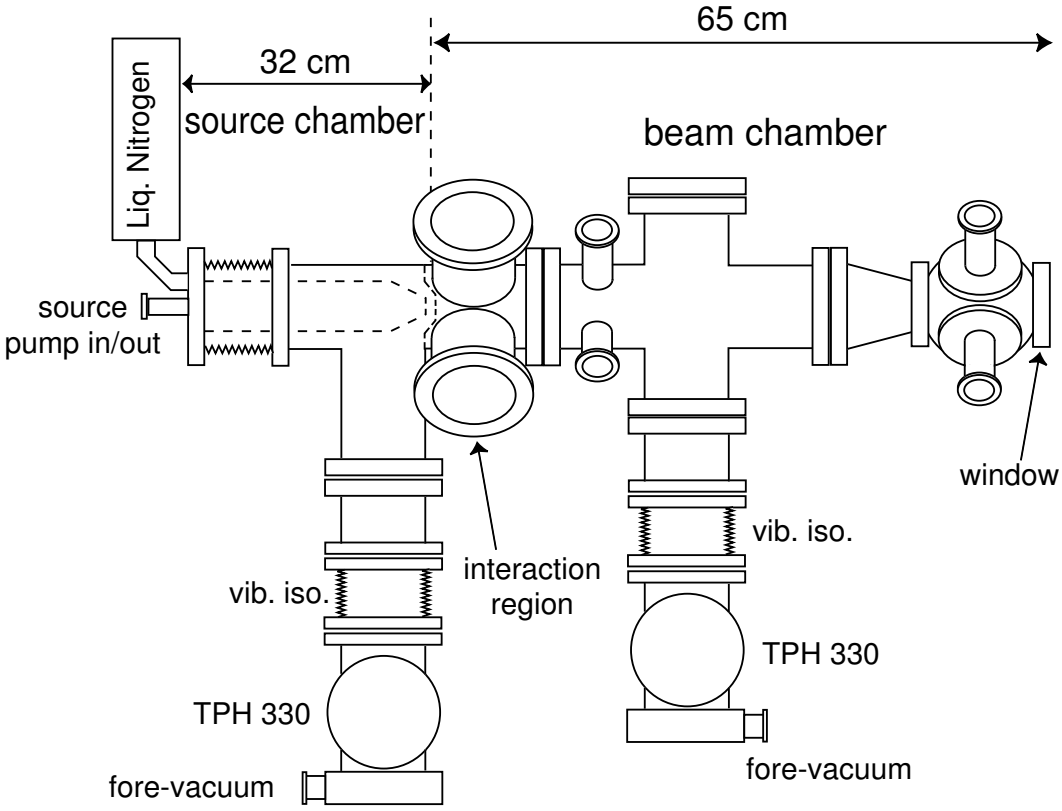

Figure 3.4 Diagram of the vacuum system in its final form as viewed from the side. The turbo pumps are attached to the system through vibration isolators. All seals are conflat, except for those connecting the gas flow and the vibration isolators. Interior components of the source are not shown (liquid nitrogen jacket and skimmer here as dashed lines). The discharge viewport is also not shown.

welded. Then a disc was welded onto the smaller end of the conical reducer, and the skimmer was mounted on this. The conical section and skimmer protruded 1 cm into the region that could be viewed through the 6-way cross, perpendicularly to the beam line. Extending the skimmer onto this conical section is what allowed optical access directly at the skimmer. Flanges were welded on all openings, taking care that at least one of a pair of opposing flanges was rotatable. On top of the vacuum chamber, up against the 6-way cross on the side of the source, a tube was welded in place that went through the vacuum wall *and* through the conical section, allowing one to view the after glow of the discharge between the nozzle and skimmer. The majority or the materials for this new construction were made of 304 Stainless Steel and obtained from Nor-Cal Products, at a total cost of $\sim$ \$1,400 (including nuts, bolts, and gaskets). All of the machining and welding was done at the Stony Brook Physics machine shop by Jeff Slechta. The new chamber is illustrated in part in figure 3.4.

The volume in the center of the 6-way cross defines the area that is the interaction region. Optical access in the region is facilitated by zero length 7056 glass viewports (Nor-Cal part# ZV-400). These are essentially windows embedded into a flange. The flange has the typical 6" outer diameter (for a 4" outer diameter tube) and the window has 3.97" clear aperture. Intensity

losses are an important consideration for the experiment, so the four windows were also anti-reflection coated for 1083 and 389 nm by VLOC. Total cost for the four flanged windows and coating was $\sim$ \$2,400.

The rest of the vacuum system containing the beam line has multiple points of access to the beam (see figure 3.4). The first section after the newly built chamber is actually what the new chamber replaced (the chamber was built in Utrecht to house the source and skimmer). It is a 4-way cross with an additional four ports (1 1/2" tube OD), each of these mounted at 45° to the horizontal plane. This section waqs mounted so that the plane of the cross is vertical, and the second turbo pump is connected to the down port. Following this section is a conical reducer and a spherical cube from Kimball Physics (MCF450-SC60000-A). This cube has a port on each side, and is mounted so that the ports perpendicular to the beam line are at 45° to the horizontal plane. This description represents the atomic beamline as it was for the final collimation experiments. The different detectors mounted in these ports will be described in the next section.

3.3 Detection and Beam Characterization

As described in the beginning of this chapter, the helium atom in the metastable state is $\sim$20 eV above the ground state. This internal energy can be

released when the He* atom experiences a collision, such as striking a metallic surface, and the ejection of an electron results. This makes the He* atom quite simple to detect, at least in large numbers. For example, if every He* produces one electron in a detector, then $\sim 6 \times 10^6$ atoms per second produces ∼one picoamp of current. Such a current is detectable with commercially available picoammeters, smaller currents have S/N ~ 1 with the meter in the lab.

3.3.1 Multichannel Plate and Phosphor Screen Detector

A very useful way to analyze the atomic beam is with a visual, real-time, two dimensional representation of a cross section of atomic distribution. This is implemented by the the combination of a multichannel plate (MCP) and a phosphor screen.

The MCP is a thin disc of lead glass which is comprised of many channels oriented parallel to one another and perpendicular to the surface of the disc. The channels form a hexagonal grid with spacings of 12 μm and have channel diameters ∼10 μm. Each channel acts as an electron multiplier. When a He* atom strikes the inside of a channel, an electron is produced, and a bias voltage accelerates the electron into the channel, causing a cascade of secondary electrons. The result is an electron multiplication factor of $\approx 10^3$ for

the bias voltages used (typically -400 to -700 Volts). The MCPs we used in the lab were purchased from BURLE (part #'s 30286 and 30299), and had an active area of 25 mm.

Directly behind the MCP was placed a phosphor screen (see figure 3.5a). This consists of a glass substrate of 1.5 inch diameter with a transparent gold evaporated coating. On top of this coating a thin layer of P20 phosphor particles is deposited, with a diameter of 1 to 1.25 inches. A thicker layer of gold in a ring around the outside of the glass plate allowed us to apply a voltage (typically +1200 to +3000 volts) to accelerate electrons from the MCP into the phosphor and then to bleed off the deposited charge. Electrons impacting the screen cause the phosphor to fluoresce with visible light. The brightness in a given spot depends on electron density (i.e. number of He* atoms hitting the MCP at that spot) and the accelerating voltage (i.e. energy of the electron). The phosphor screens were manufactured by James van House in Vancouver, WA. The MCP and phosphor screen were sandwiched together and mounted in the vacuum system using Kimball Physics eV Parts®. The whole assembly was mounted on a linear motion vacuum feedthough and can be moved completely into and out of the atomic beam at a distance of 22 cm from the skimmer (mounted from the top of the 4-way cross in the center of figure 3.4).

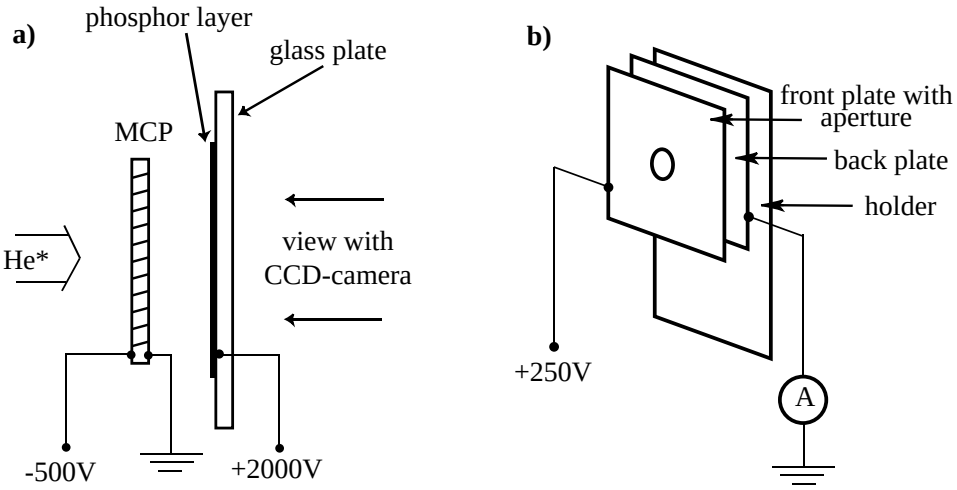

Figure 3.5 a) Schematic of the visual 2D detector. b) Schematic for the stainless steel plate detector. Typical values for voltages are shown.

The phosphor screen was viewed through a flanged window at the end of the vacuum chamber by a CCD camera (manufactured for use as a CCTV security camera). The "refresh rate" of the entire detection system is fast enough that changes to the experiment can be be viewed in real time, making this an essential tool for alignment and troubleshooting. Images can be grabbed from the camera and stored onto a computer using a TV tuner card (AVerMedia TV98) as bitmap files. Analysis of the images is primarily done with a public domain Java application called "ImageJ" developed at the National Institute of Health. There is a direct correlation between the greyscale pixel value across the image to the brightness across the phosphor screen.

While being very useful for real time viewing of the collimation alignment, the MCP/phosphor screen had some severe limitations. A calibration

of the correlation between atom flux and pixel value was not possible. The efficiency of a He* to eject an electron from the surface of the MCP is not well known. The sensitivity of the combination of MCP and phosphor screen to atomic flux is also non-linear and non-uniform. The non-uniformities are a result of the quality of production of the components and moreover due to higher fluxes causing faster aging of the MCP and phosphor screen (e.g. see figure 3.6). Applying voltages to the phosphor screen while pulled out of the beam would refresh it some, and higher voltages could be applied to regain brightness. Many tests were done looking at atom conservation and varying source flux, but we were unable to produce images we could trust as having a direct linear correlation between atomic flux and pixel value. To obtain an absolute measurement of atomic flux, we resorted to a more simple detection scheme.

3.3.2 Stainless Steel Scanning Plates

For a more qualitative measurement of atomic flux we used a set of 0.5 mm thick stainless steel plates in an arrangement shown in figure 3.5b. Helium atoms that pass through the 1 mm aperture of the front plate strike the solid back plate, ejecting an electron with roughly 70% efficiency [46]. The positive voltage on the front plate collects these electrons and the resulting current off

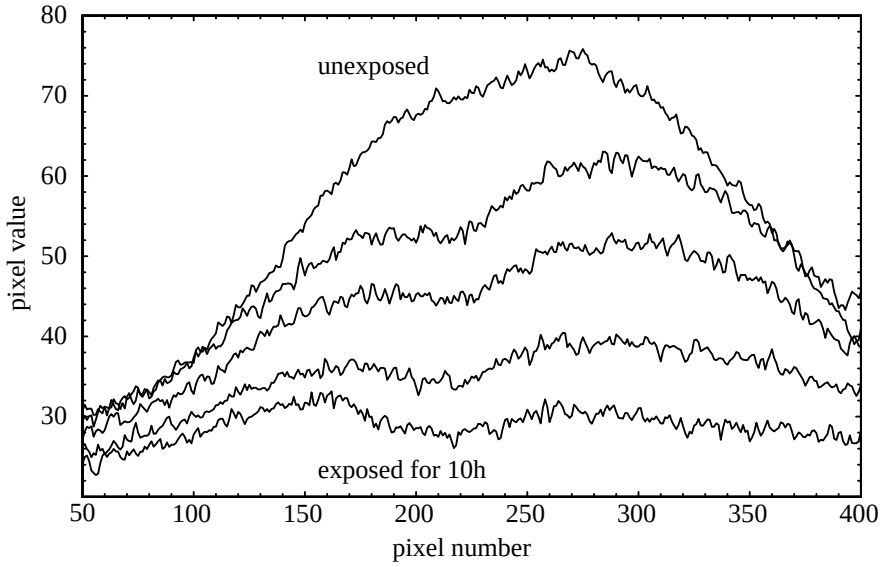

Figure 3.6 Profile of pixel values taken from a line across phosphor screen images. The top profile is from an image taken immediately after installing a new phosphor screen. The lowest is after approx. 10 hours of exposure to the atomic beam. The aging is greater at the center, where the atomic flux is higher.

of the back plate is measured with a Keithley model 486 picoammeter. The two plates are rigidly mounted on a third supporting plate by nylon nuts and bolts, and isolated from each other by alumina spacers (2 mm between each plate). The stainless steel detector (SSD) is then mounted in vacuum on a linear motion feedthrough and can be scanned transversely (5 mm scan range) through the center of the atomic beam, measuring atom flux as a function of position. We have three SSD's placed on our beamline, one at 16 cm from the skimmer, and two (scanning orthogonally) at 56 cm from the skimmer. They are mounted on the smaller feedthroughs, at 45° to the horizontal, shown in figure 3.4.

Metastable helium atoms are not the only contribution to the current. The SSD is also sensitive to UV photons entering the aperture. By using a blue-detuned optical molasses, He* atoms can be completely removed from a given part of the beam. With the aperture placed in the "shadow" of the molasses, the measured current is only a result of UV photons. In this way, we determined that the UV fraction of our measured flux is about 25% of the background signal. We also assume that the angular distribution of UV photons from the source is the same as for He* atoms. This method also indiscriminately accounts for measured flux due to the shorter lived 2^1S_0 metastable, although this is believed to be quite small ([44, 45]).

Another contribution to the measured flux are charged particles, mostly electrons, but possibly some helium ions as well. The contribution from electrons takes the form of a negative linear offset to the positive current due to He* atoms. We were able to use a uniform magnetic field ($\approx$4 Gauss) created by Helmholtz coils to sweep all the charged particles out of the beam. This allowed for measurement of the uncollimated beam, however, it established an undesirable quantization axis for the bichromatic experiment. Instead we used two parallel stainless steel plates, separated by 3 cm and centered around the atomic beam. These were placed between the interaction regions and the SSD at 16 cm. Ideally the plates would be placed directly after the skimmer,

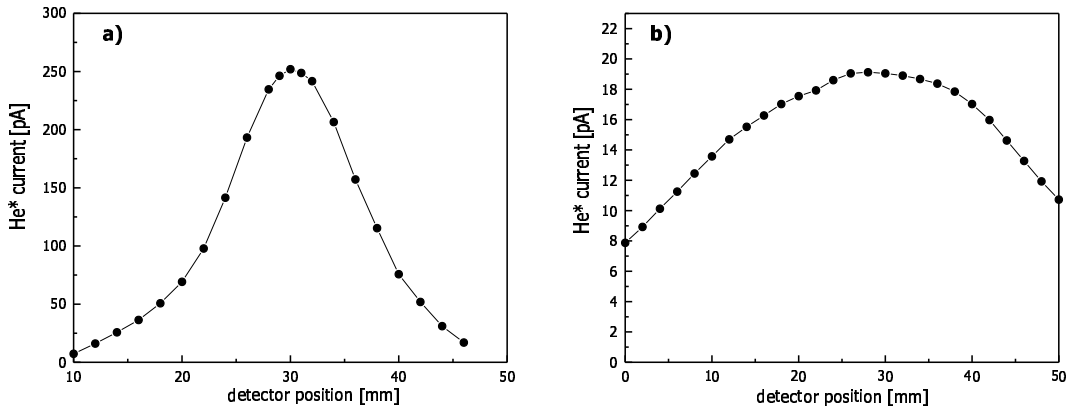

Figure 3.7 a) Background scan at 16 cm from skimmer b) Background scan at 56 cm. The scan at 16 cm includes a small linear correction. Both scans have had the UV contribution removed. Curves are drawn to guide the eye.

but for collimation we wish to have our interaction regions directly after the skimmer. Voltages applied to the plates up to ± 1000 volts were used to sweep most of the charged particles out of the beam and a small linear correction was used for what remained. Even with the deflection plates in place, we still observed a negative offset to the signal on the two SSD's at 56 cm. This suggests that electrons are created within the beam, either by inter-beam collisions, collisions with the background gas, or stray UV light ejecting electrons from the vacuum walls. To correct for this, we placed a magnetic optic table mount (permanent magnet) over top of the beamline directly before the far SSD's. This removed all of the negative offset, and no adverse effects were observed from any stray fields this may have created in the interaction region.

Typical profiles of the uncollimated atomic beam measured with the

SSD's are shown in figure 3.7. Here the source discharge is at 6 mA. The spatial FWHM of these profiles shows that the uncollimated beam has a FWHM divergence of 90 mrad (the same value obtained from the unexposed trace in figure 3.6 agrees well with this) . With an average longitudinal velocity of 1000 m/s, the beam has a FWHM transverse velocity spread of ±45 m/s. Note that the atomic beam at 56 cm has expanded enough such that the full SSD scan range barely covers the FWHM. From these profiles we have also extracted information about the total output of the source. In the scan at 16 cm from the skimmer, we observed 250 pA at the peak. This gives a flux of

$$\dot{N} = \left(250 \times 10^{-12} \frac{C}{s}\right) \left(\frac{1 \text{ e}^-}{1.6 \cdot 10^{-19} \text{C}}\right) \left(\frac{1 \text{ He}^*}{0.7 \text{ e}^-}\right) = 2.2 \times 10^9 \frac{\text{atoms}}{\text{s}} \quad (3.1)$$

into the 1 mm diameter aperture of the SSD. The solid angle subtended by the aperture is 3.1×10^{-5} sr, which results in a centerline flux per sterradian of 7.2×10^{13} atoms/s-sr. Combined with the measured FWHM, we estimate a total ouput flux from the source of 4.3×10^{11} atoms/s.

A summary of the type and location of the detectors is given in Table 3.3.2.

Detector	Distance from Source Skimmer	Angle Subtended	Data taken as:	Scan Direction
SSD1	16 cm	318 mrad	current [pA]	UL to LR
MCP/Ph.Scr.	22 cm	115 mrad	.BMP image	NA
SSD2a	56 cm	91 mrad	current [pA]	UL to LR
SSD2b	56 cm	91 mrad	current [pA]	UR to LL

Table 3.2 A summary of key information about the detection of the atomic beam. SSD=Stainless Steel Detector, and MCP/Ph.Scr. is the Multi-Channel Plate and Phosphor Screen combination. The MCP/Ph.Scr. sits in the beam, while the SSD's scan. The direction of the scan is described from the viewpoint of an observer with the atomic beam coming towards them. U,L = Upper, Lower. R,L = Right, Left.

Chapter 4

Bichromatic Light Production

One of the most elegant aspects of this experiment is that all of the light was derived from a single diode laser. This chapter describes the laser system that was used to produce the multiple frequencies in multiple beams of intense light for the collimation experiment.

4.1 The Diode Laser

The laser used to generate light for collimation was a Spectra Diode Labs SDL-6702-H1 Distributed Bragg Reflector (DBR) diode laser. The practical use of diode lasers in atomic physics has been well established for almost 20 years. An excellent review of the subject can be found in [47] and the references therein. The DBR laser is a more recent development, first used with He* in 1994 [48], and is well described in recent texts [49, 50]. The basic

concept is that a grating is incorporated into the active region of the diode. The grating acts as a narrow band reflector and thus becomes a wavelength selective element in the laser cavity. There are several of these specific SDL lasers in the lab. Their frequency control and stabilization was first investigated by C. Avila [51] and they were first put to use in the polychromatic force experiments by M. Cashen [35]. The particular diode used for this experiment has been in use since the beginning of the polychromatic force experiments (first light in March, 1999). It has had a long life and is showing signs of age (for example, on occasion the operating temperature had to be changed to keep it on atomic resonance). Before the collimation experiments began, the laser was discontinued by Spectra Diode Labs (for lack of commercial interest in the particular wavelength) and no replacement was available until recently. A German company, Sacher Lasertechnik, is now making a more sophisticated version.

The SDL-6702-H1 laser comes in a standard TO-3 window package with 8 pins. Incorporated into the package is a thermistor and thermoelectric cooler (TEC) for temperature monitoring and control. The temperature was controlled via feedback from the thermistor to the TEC with a commercial temperature controller, ILX Lightwave model LDT-5910. Injection current to the diode is provided by a commercial current controller, Thorlabs model

LDC 500. The current (and thus the laser frequency) could be modulated up to 150 kHz by applying a voltage to a BNC input on the rear of the controller. The diode could have an output power of 50 mW with injection current near the maximum 170 mA specified by the manufacturer. However, for this experiment, the laser was operated at 24.4°C with 135 mA injection current, resulting in 30 mW output power. The reduced current results in a reduced power, but will lengthen the life of the laser. The temperature of 24.4°C is slightly below the average room temperature of 26°C [1]. At these settings we were able to reliably have the laser on atomic transition at 1083 nm.

4.1.1 Frequency Control and Linewidth Narrowing

Precise control of laser frequency is required in almost any atomic physics experiment. With diode lasers, the frequency can be tuned by adjusting the temperature and injection current, or with optical feedback [47]. For the collimation experiment, temperature and current were used as course frequency control to set the laser at 1083 nm. These tuning characteristics were previously thoroughly investigated [35, 51]. In order to fine tune the

[1] The room was kept this warm since it was found that the overall room temperature was most stable at this thermostat setting. The stability of room temperature was not as large a concern for this experiment as it was for other experiments in the room.

laser frequency and scan over a particular resonance we used controlled optical feedback in the form of an "extended cavity" (EC) [52]. The configuration for this optical feedback is shown in figure 4.1. In essence, an extra cavity is formed, between the back Bragg reflector of the DBR diode and the external high reflectivity mirror, which is coupled to the cavity of the laser diode itself. The frequency of the laser can be controlled by adjusting the length of the EC. The length of the EC is adjusted by a piezo electric transducer (PZT) driven by a homebuilt high voltage controller. In this way, the laser is tuned by about 3.2 MHz per Volt applied to the PZT. With the extended cavity in place, the frequency stability of the laser becomes quite sensitive to any perturbations in the length of the EC, such as those caused by vibrations, temperature drifts, and air currents. Typical sources of vibrations range from mechanical pump rattling transmitted through the floor to someone speaking loudly in the lab. In order to reduce the effects of these perturbations, several steps were taken. The entirety of the laser and EC components were mounted (with 1 inch high, 1 inch diameter pedestal posts) on a solid $12 \times 24 \times 3$ inch slab of aluminum set on top of a larger 2 inch thick piece of Owens-Corning polystyrene foam insulation. A "housing" to cover the entire Al slab and laser/EC was made of the same insulation material. This construction reduces disturbances to the extended cavity to the extent that the laser frequency is stable on the

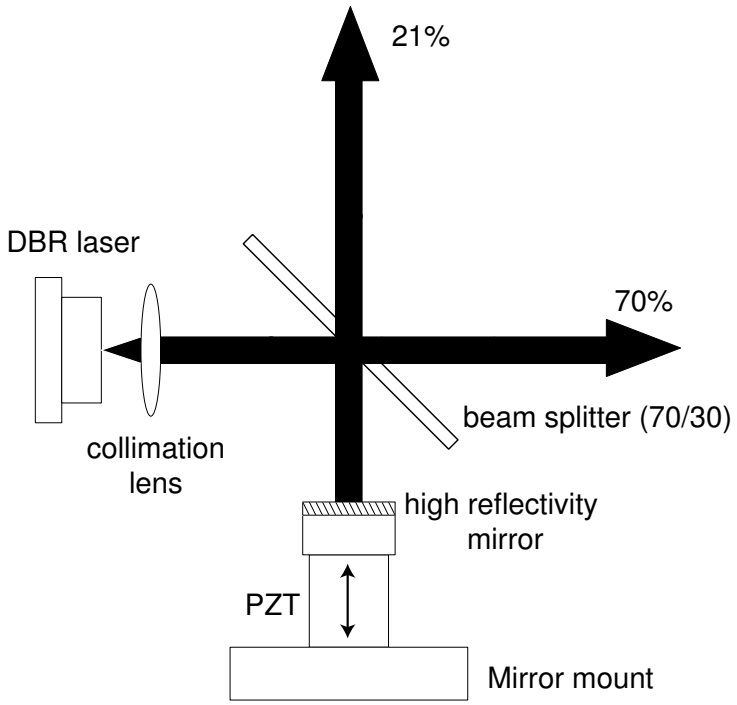

Figure 4.1 The configuration of the extended cavity that provides optical feedback to the laser. The laser light is collimated and incident on a 70% transmission beamsplitter. The reflected part of the light from the beamsplitter is retroreflected by a $> 99\%$ reflectivity mirror mounted on a PZT on a kinematic mirror mount. On route back to the laser, 30% of the light is reflected by the beamsplitter, so that 9% of the original laser output is fed back. The 70% transmitted by the beamsplitter is used for the experiment, and the remaining 21% can be used for saturated absorption spectroscopy. [35]

order of or less than a few MHz. To further reduce fluctuations and long term drift more steps were necessary. The means by which the laser was set to a particular frequency will be described in a subsequent section.

Besides allowing one to fine tune the frequency of the laser, the extended cavity also serves to narrow the linewidth of the laser [47, 52]. Without the extended cavity, the linewidth of the laser is 3 MHz, while the natural linewidth of the atomic transition used in the experiments ($2^3S_1 \rightarrow 2^3P_2$) is

1.6 MHz. Linewidth reduction by EC feedback was measured [35] by beating the laser with a second DBR laser (also with an extended cavity) and determined to be 125 kHz. This is an order of magnitude smaller than the natural linetwidth and more than narrow enough for the bichromatic collimation experiment.

4.1.2 Saturated Absorption Spectroscopy

A Doppler-free Saturated Absorption Spectroscopy (SAS) signal was used to monitor the frequency of the laser relative to an atomic transition [53]. Figure 4.2 shows schematically how the extra beam off of the extended cavity can be used to derive this signal. A thick un-coated glass plate reflects $\sim 4\%$ of the input beam from each surface, making two weak beams, termed "probe" and "reference." The two beams pass parallel through a He discharge cell, through a 50/50 beamsplitter, and onto two photodiodes. The beam that passes through the thick glass plate, called the "pump", is reflected off of the 50/50 beamsplitter to counterpropagate against the probe through the cell. As the laser is tuned across atomic resonance, the absorption from the reference and probe beams is dominated by the Doppler broadened peak. However, as the frequency scan nears atomic resonance, the probe and pump (which have opposite Doppler detunings) interact with atoms of the same velocity.

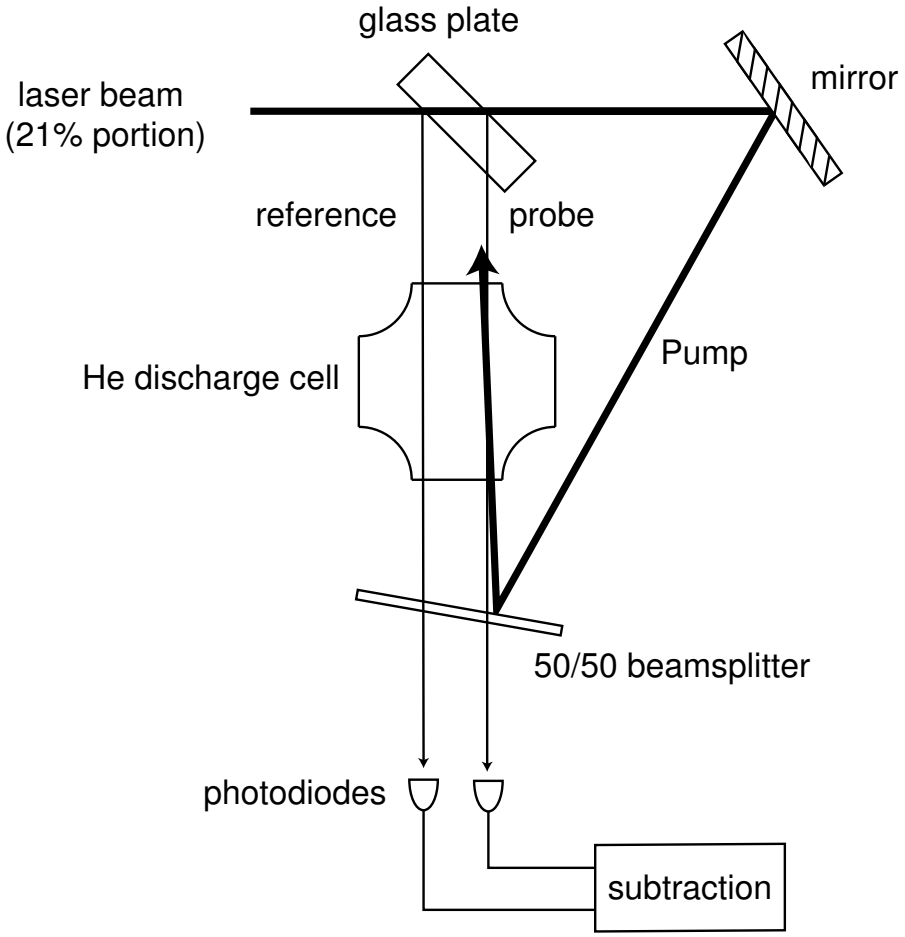

Figure 4.2 Schematic showing how a portion of the laser beam can be used to set the frequency of the laser on an atomic resonance. The mechanism of Saturated Absorption Spectroscopy is described in the text. Note that the cell has *two* pairs of parallel surfaces.

The pump, being much more intense, saturates the transition, diminishing absorption of the probe. The resulting feature is the Doppler-free Lamb dip. Since the photodiode signals of the probe and reference are subtracted from each other, the Doppler broadened peak is eliminated from the signal, leaving only the narrower Lamb dip.

Often, such as when aligning the laser beam to the atomic beam, the laser can be tuned to atomic resonance "by hand", and be stable enough for the task. However, for collimation, the laser needs to be locked to a certain frequency. The locking method will be described after the introduction of one more key element.

4.2 Four Frequency Production

After the extended cavity an optical isolator was placed in the 70% beam to the experiment (see figure 4.1). The isolator is critical in preventing unwanted optical feedback to the laser diode which could result in frequency instability or the failure of the diode. A commercial isolater was used, OFR model IO-3-1083-HP, which utilizes the Faraday effect to create an "optical diode" [54]. The isolator had an isolation $\sim$ 39 dB in the reverse direction and allowed $\sim$ 90% transmittance in the forward direction (i.e. 20 mW).

The output of the isolator was then coupled into a single mode optical

fiber. The purpose of this step was two-fold. This brought the height of the laser beam closer to the optical table, and also cleaned up the spatial profile of the light. The output of the diode laser is elliptical, and the collimation lenses that were used could not completely compensate for this. The output of a single mode fiber is a TEM_{00} Gaussian beam. Typically, the coupling efficiency into the fiber was $\sim 40\%$.

4.2.1 Double-passed Acousto-Optic Modulator

The bichromatic force actually requires four frequencies, as described in section 2.4, to be used in the collimation experiment. This is necessary to Doppler shift the force profile to be centered at a non-zero velocity, v_c , and to position the sharp force drop-off at $v = 0$. An acousto-optic modulator (AOM) is used to produce the four frequencies from the single frequency laser diode [34, 38, 39].

Light from the optical fiber is directed into the AOM setup shown in figure 4.3. The AOM is an Isomet model 1205-603F and was originally manufactured in 1988[2]. An RF acoustic wave is launched into the crystal. The compressional nature of the wave creates a sinusoidal variation in the

[2] The AOM was borrowed from another experimental setup (Rubidium) in the lab, and was likely purchased from a re-seller. The surface of the crystal is coated, but the type of coating is unknown.

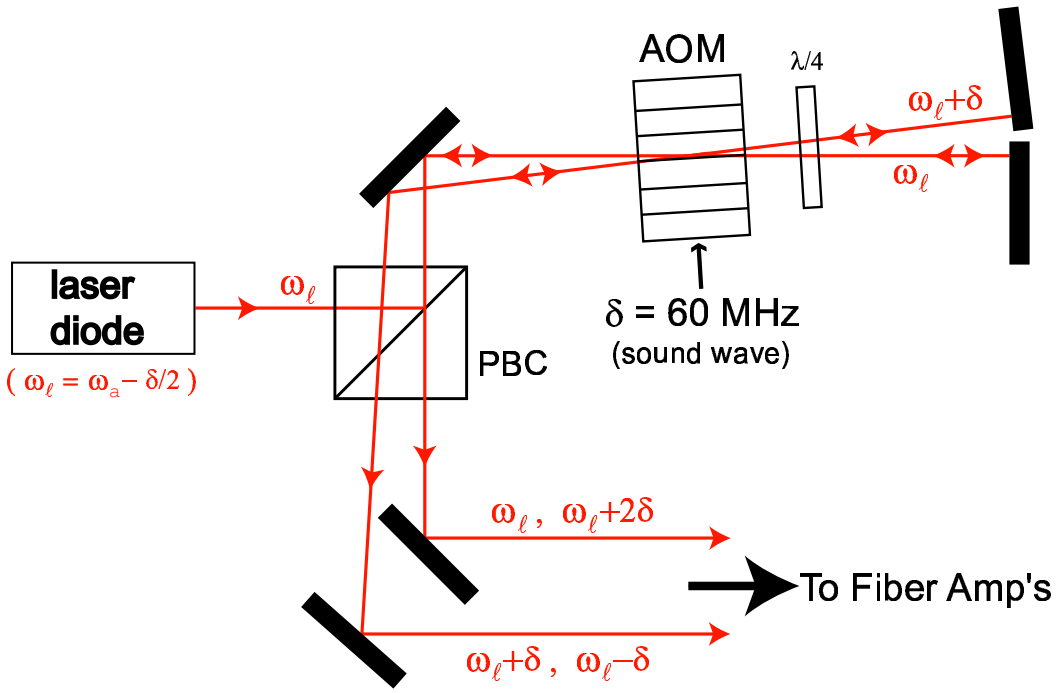

Figure 4.3 Double-pass AOM schematic for producing all four necessary bichromatic frequencies. The AOM is operated at $\delta/2\pi = 60$ MHz, the bichromatic detuning. The diffraction angle has been exaggerated, and is actually $\sim 1°$. Polarization optics serve to separate the bichromatic beams from the input beam. PBC = polarizing beamsplitting cube. The optical isolator and fiber between the laser and AOM are not shown.

local index of refraction within the crystal, which acts as a traveling diffraction grating.

With careful optical alignment (mainly the angle between the input beam and front surface of the crystal) and choice of RF drive power, the beam can be equally split ($\sim$ 49% each) into the zero order, ω_ℓ , and first order, $\omega_\ell + \delta$, diffracted beams. Both of these beams are then retroreflected back into the AOM and each are again diffracted equally into two beams. The zero

order ω_ℓ is split into ω_ℓ and $\omega_\ell - \delta$. The first order $\omega_\ell + \delta$ is split into $\omega_\ell + \delta$ and $\omega_\ell + 2\delta$. The result is two spatially distinct beams, each with two frequencies separated by 2δ. Polarization optics were used to remove the two bichromatic beams from the input beam (see figure 4.3). Each of the beams were then coupled into two single mode fibers, the inputs of the fiber amplifiers.

When the laser frequency is set such that $\omega_\ell = \omega_a - \delta/2$, the frequencies in these two beams are those required to produce the Doppler shifted bichromatic force:

$$\omega_\ell, \omega_\ell + 2\delta \Rightarrow \omega_a \pm \delta + kv_c$$
$$\omega_\ell - \delta, \omega_\ell + \delta \Rightarrow \omega_a \pm \delta - kv_c \tag{4.1}$$

with $kv_c = \delta/2$. The right hand side of equation 4.1 is identical to the frequencies of figure 2.6.

4.2.2 Bichromatic Locking Scheme

In order to compensate for long term drift of the laser frequency, it was necessary to lock the laser. To have the laser set to $\omega_\ell = \omega_a - \delta$ we used SAS with the He* cell to lock $\omega_\ell + \delta = \omega_a$. However, no light is produced by the double-passed AOM at this frequency. So, part of the $\omega_\ell \pm \delta$ beam was split off, after the fiber amplifier (discussed below), and sent to another AOM driven at 90 MHz ($\frac{3}{2}\delta$). The first order beam (now with frequencies $\omega_\ell + \frac{1}{2}\delta$ and $\omega_\ell + \frac{5}{2}\delta$)

is then sent to the discharge cell. As the laser is scanned over resonance, three Doppler-free peaks are observed, one for each of the frequencies and a third crossover peak halfway between them (see figure 4.4a).

A 10 kHz sinusoidal signal is applied to the modulation input of the injection current to the DBR, and also given as a reference signal to a lock-in amplifier (Princeton Applied Research model 5104). The modulated SAS signal is fed into the lock-in amplifier and mixed with the reference signal. The resulting output is proportional to the derivative of the Doppler-free absorption signal (figure 4.4b). This serves as an error signal. When the PZT scanning is turned off and the laser set to a peak, the error signal is fed back to the EC PZT to compensate for any drift away from resonance. A schematic of this feedback loop is shown in figure 4.5.

4.3 Fiber Optic Amplifiers

If the double-passed AOM were to be considered the "heart" of the experimental setup, then the "muscle" is certainly the fiber amplifiers. As has been shown, the bichromatic force requires that the Rabi frequency of each component of the bichromatic field needs to be scaled with the bichromatic detuning ($\Omega_r \simeq \sqrt{\frac{3}{2}}\delta$). For the collimation experiment, this required that the two bichromatic beams leaving the AOM need each have on the order of 1

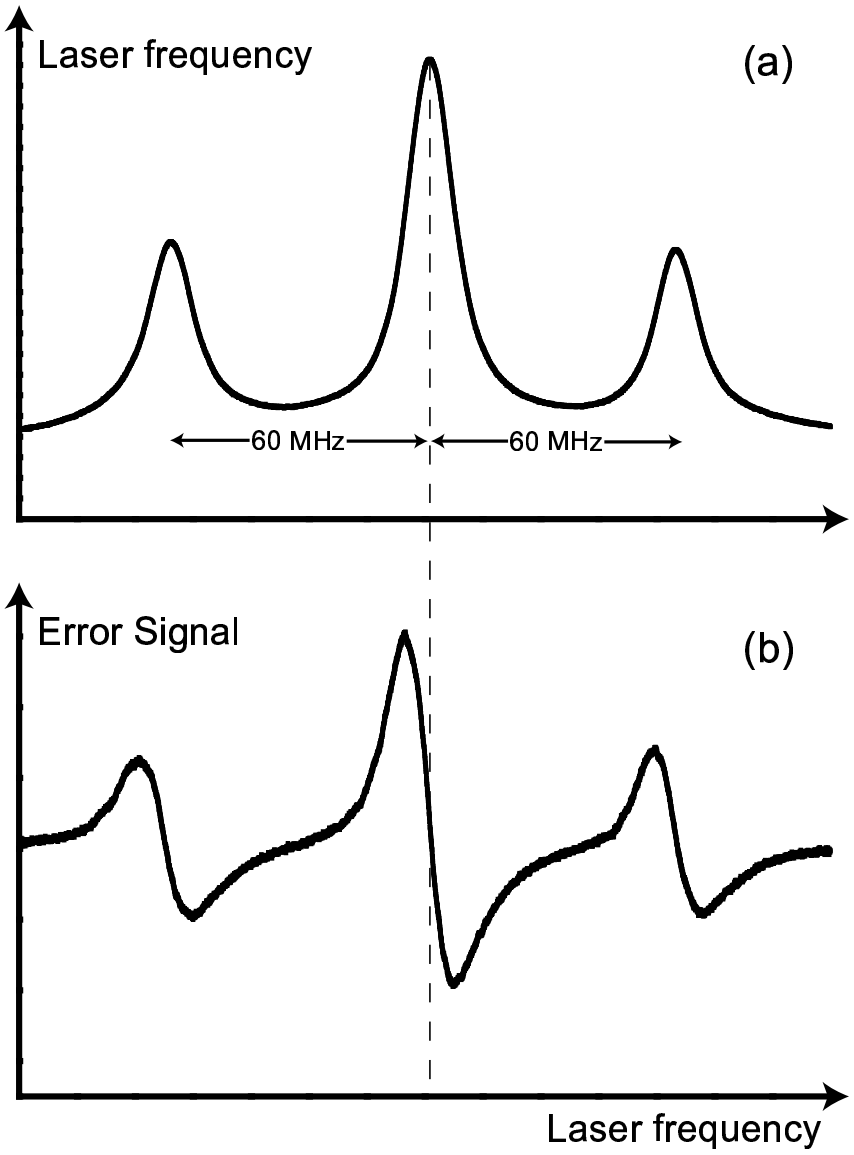

Figure 4.4 Saturated absorption spectroscopy (a) and derived error signal (b) vs. frequency of the laser. In this SAS arrangement the laser has two frequencies separated by 2δ. The middle peak is a crossover between them. The error signal was recorded with a slow scan rate of 1 Hz and 16 averages. Note in (b) that the error signal crosses zero at the peak position.

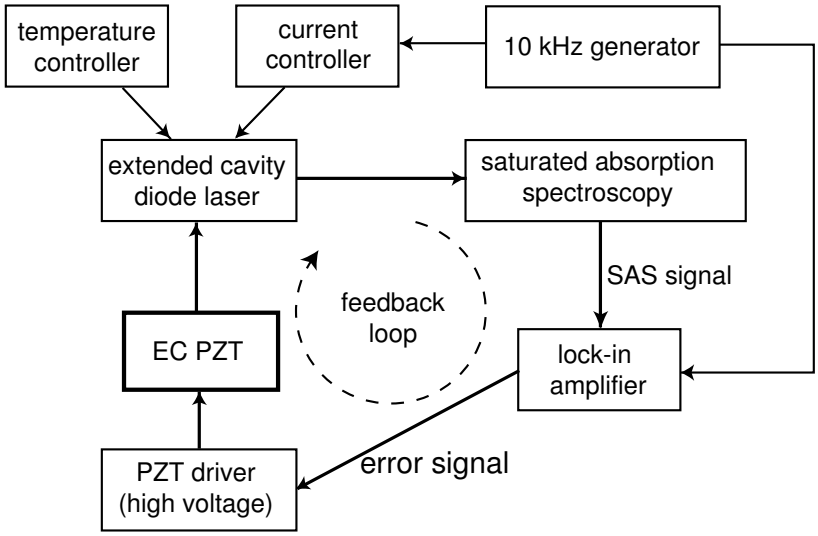

Figure 4.5 Schematic flow chart for how the laser frequency is controlled. Temperature and current are chosen to set the laser at 1083 nm. The extended cavity fine tunes this frequency. Current modulation provides the means to derive an error signal to feedback to the EC to account for frequency drifts.

Watt cw power. However, of the 30 mW output of the DBR, only several mW is in each beam. These two beams are coupled into two fiber amplifiers (FA's).

The fiber amplifiers currently in use are manufactured by Keopsys, and were custom built for this experiment from their model KPS-BT2-YFA. They were purchased (at ∼$20k each) in the late fall of 2003, were tested for performance, and finally put into use in the collimation experiment in early February 2004. Up to that point we had been using an older model manufactured 5 years prior. The advantages of the newer model over the old were more than just an increase in power, and will be discussed.

The new FA's are made up of two gain stages. In each stage, single mode fiber with a core doped with ytterbium (Yb) is the gain medium. Light

from high power, wide-bandwidth diode lasers, operating at 975 nm, is injected into the core. This pump light provides the population inversion necessary to amplify the light at 1083 nm via stimulated emission [49]. The first stage, or "pre-amp", is a fixed gain stage, and provides ∼200 mW at the output with 1 mW injected light. (A fiber-spliced photodiode monitors the input power). The "pre-amp" stage was found to be easily saturated, providing constant output power over variations (±0.2 mW) in input power. The second, "booster" stage is pumped by two diode lasers. Adjusting the injection current of each serves to adjust the gain of the amplifier. The FA allows independent current control of these two diodes. Setting the first to its maximum current of 5 Amps yields 3 Watts output. Then, adding current to the second diode provides additional gain for over 4 Watts of output power (see figure 4.6). For the collimation experiment, the second pump diode was not used.

Internal to the amplifier, an optical isolator at the input reduces (> 20 dB) optical feedback to the DBR. A second isolator between the two gain stages serves to reduce the potential of any non-linear effects, such as Stimulated Brillouin Scattering (SBS) [55, 56], building up over the entire length of the gain medium. The main limitation to the output power of the FA lies in avoiding the onset of non-linear effects. This threshold depends on other factors relating to power density per frequency, such as laser linewidth and the

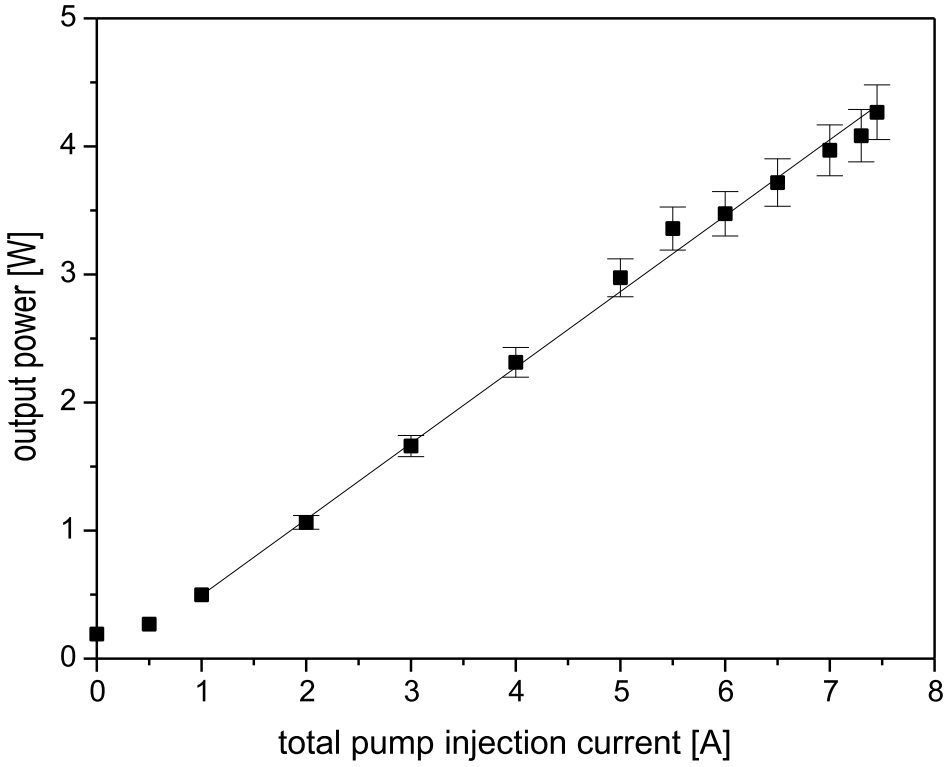

Figure 4.6 Fiber amplifier gain vs. combined "booster" pump diode current for 1 mW injected power. The maximum output power is 4.3 W at the maximum current settings specified by the manufacturer. The line is a fit to the linear portion of the curve, and has a slope $\sim$ 590 mW/A. Error bars are from the calibrations of our various power meters.

cross sectional area of the fiber core. The total length of the fiber also must be taken into account, especially regarding SBS. To calculate the maximum power obtainable without inducing SBS is not possible for us, as it would require proprietary knowledge of the FA's. However, we can estimate that for the narrow input linewidth, the maximum is on the order of only several watts, and 4 W was the specification from Keopsys. Several steps were taken by the manufacturer to achieve this power, such as inserting the second isolator. The

output fiber had a "non-standard" large core (9.2 μm instead of 6.6 μm) and had to be limited in length to 70 cm. This necessitated mounting the FA's directly on the optical table, rather than in an electronics rack. In testing the FA's, we monitored the output power and spectrum for signs of non-linear effects up to 4 Watts output, and observed none. It is our understanding that this is one of the first fiber amplifiers Keopsys has produced for 4 W output at 1083 nm with a sub-MHz linewidth.

The input and output fibers were connectorized by Keopsys with industry standard FC/APC connectors. These connectors have the fiber end polished at an 8° angle, to reduce reflections back into the fiber. The older FA's (in use until the beginning of 2004) had bare fiber outputs which were either cleaved or connectorized in the lab. Although the lab has gained much experience with fibers, we are still not able to produce the high quality of fiber termination necessary for such large optical powers. With the older FA's, amplified spontaneous emission (ASE) and self-lasing were often a problem in terms of noise in the output spectrum and feedback to the DBR (older models also had no internal isolation). The amplifiers rarely worked well up to the specified output power of 1 Watt. At the point of replacing them, one did not operate noise free at the power needed for bichromatic collimation. Also, they did not have input coupling monitors or pre-amplification stage, such

that drifts in input coupling added another difficulty to the experiment during a given run.

Optical fiber is birefringent [57], the degree of which depends on physical stresses and strains. To set the polarization of the output light, the input and output fibers were coiled, bent, and secured to maximize the desired linear polarization. Fine-tuning of this polarization was possible by a component installed in the fiber amplifier that precisely squeezed and twisted a small section of the output fiber. The resulting light was 98% in the desired linear polarization.

Two ThorLab F230FC-C fiber couplers were used to collimate the output of the FA's. The output was Gaussian with a 800 μm waist.

4.4 Preparing the Bichromatic Collimation Beams

During the course of setting up the collimation experiment, it became most convenient to label the two beams, from the double-passed AOM, by their respective Doppler shifts (see figure 4.3 and equation 4.1). The "$+kv_c$" beam was coupled into a fiber amplifier (FA1), and the "$-kv_c$" beam was coupled into a second fiber amplifier (FA2).

At the output of FA2, a 70/30 beamsplitter was placed in the "$-kv_c$"beam, such that 30% of the beam went to the second AOM and SAS locking setup

as described in section 4.2.2. A portion of this beam was later used to supply the light for an optical molasses.

The light out of each fiber amplifier was further polarized by polarization beam-splitting cubes (PBC's). The $\sim 2\%$ of the light that was reflected rather than transmitted by the PBC was directed onto both a Fabry-Perot interferometer and a fast photodiode. The interferometers were mainly used to observe the bichromatic spectrum of the FA outputs, first to check that the components at each frequency were equal in magnitude, and second to ensure that no SBS, ASE, or self lasing occured. Since the separation of the peaks was well determined, the signal through the interferometer could be used to calibrate the frequency change per applied PZT voltage of the extended cavity (i.e. 3.2 MHz per Volt). Also, by adjusting FA output polarization to minimize the peaks, we maximized the preferred polarization. However, the polarization was found to be fairly constant, and only needed adjusting on a monthly basis to account for a small, few percent drift.

4.4.1 Intensity Beat Phase Measurement

Two fast photodiodes (UDT model InGaAs-100L) monitored the amplitude modulation (the beating at frequency 2δ) in each beam. The $2\delta/2\pi =$ 120 MHz signal was viewed with a Tektronix 2445 oscilloscope (with a rated

bandwidth of 150 MHz). Recall that these beats are the "pulses" of the π-pulse model in section 2.1. As described in that model, it is necessary to properly choose the arrival times of the counterpropagating pulses. Each beat has length in time $T = \pi/\delta \simeq 8.3$ ns, which corresponds to a length of $L = cT \simeq 2.5$ m and these lengths correspond to a phase change of 2π in a given beam. In the π-pulse model, the "$-kv_c$" beam must be $\phi = \pi/2$ ahead of the "$+kv_c$" beam at each interaction region to have the desired force.

To determine the phase between the bichro-light beams at the atomic beam, we measured the distance from the PBC's to the photodiodes and from the PBC's to the interaction regions. Delays between the photodiodes themselves were also accounted for. In comparing these lengths, we knew then what the time delay measured on the scope corresponded to in phase delay at the atomic beam. A rough adjustment to the desired phase was accomplished by changing the optical path lengths between the double-passed AOM and the respective fiber couplers of the FA's. The combined error from the photodiode measurement and from the distance measurement was $\approx \pm 4°$. This was easily compensated for while running the experiment by actively changing the phase. A variable phase delay was inserted into the "$+kv_c$" beam before the fiber amplifier. This consisted of a retro mirror on a translation stage with a PBC and $\lambda/4$ plate (see figure 4.7). The translation stage was inserted onto the optical

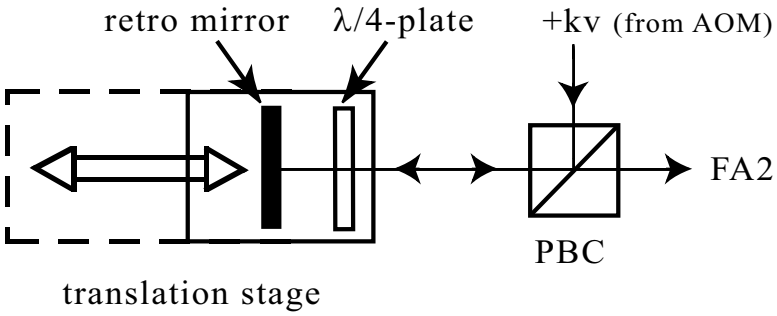

Figure 4.7 Schematic of translation stage setup used to fine tune the optical path lengths between the "$+kv_c$"and "$-kv_c$" beams. The translation stage was a simple slide on ball bearings, but the position could be repeatedly adjusted with steps of 1 mm $\simeq 1.5°$. The input polarization is linear, the double pass of the $\lambda/4$ plate makes the output also linear but orthogonal to the input, exactly as in figure 4.3.

table underneath the elevated fiber amplifiers. With a total range of motion of $\sim$ 30 cm, the phase between the "$+kv_c$"and "$-kv_c$" beams could be adjusted within $\pm 43°$of the desired phase relation set by the rough adjustment of path lengths. The phase stage also allowed us to compensate for daily fluctuations of the phase on the order of $\sim 6°$. Moving the translation stage did slightly change the coupling of the beam into the FA. However, this was compensated by the saturation of the FA pre-amp.

4.4.2 Interaction Regions

The $\sim$ 98% light flux transmitted by each PBC from the FA output was used to form the beams that were sent to the atomic beam for bichromatic collimation. Since the average longitudinal velocity of the atoms was $\sim$1000

m/s, the collimated output of the fiber needed to be expanded to have sufficient interaction with the atoms. To accomplish this, two telescopes were used in each beam, a spherical lens telescope to expand the beam overall, and a cylindrical lens telescope to expand the beam along one axis. This long axis was then oriented to be along atomic beam. The telescopes were adjusted so that the bichromatic beams were well collimated, by measuring the beam size both directly after the telescopes and at several meters away from the telescope (a distance corresponding to the beams having passed through the interaction regions). The profiles were measured by scanning a $\sim$ 25 μm pinhole across the beam and/or by using a CCD beam profiler (OphirOptronics Beamstar-USB). The profiler was convenient since it allowed real-time imaging of the beam profile, but did have some "noise" due to multiple reflections of the CCD glass cover and attenuators. The pinhole scan was more accurate, although the measurement required a great deal more time. The resulting Gaussian waists of each beam were $w_{long} = 6.3$ mm and $w_{short} = 1.8$ mm, where we have defined w as the $1/e^2$ radius of the profile ($I = I_0 \cdot e^{\frac{-2x^2}{w^2}}$). Note that w_{long} is comparable to the distance given by the bichromatic slowing time (see equation 2.19) of 5.9μs and $v_{long} = 1000$ m/s.

As shown in the numerical calculations and the DDA picture of the bichromatic force, it is required that $\Omega_r = \sqrt{\frac{3}{2}}\delta$. With $\delta = 2\pi \times 60\text{MHz} = 37\gamma$,

this requires a saturation parameter per frequency[8]

$$s \equiv 2|\Omega_r|^2/\gamma^2 = I/I_s \simeq 4100 \tag{4.2}$$

where the saturation intensity is

$$I_s \equiv \pi hc/3\lambda^3\tau = 0.167 \text{ mW/cm}^2 \tag{4.3}$$

for the transition in helium. Thus, the total power required in the collimated beams was

$$P_{total} = 2sI_s\frac{\pi}{2}w_{long}w_{short} \simeq 250 \text{ mW/cm}^2 \tag{4.4}$$

with the factor of 2 since this power includes both frequencies of the bichromatic beam.

Apertures were placed in the bichromatic beams close to the atomic beam to cut off the wings of the Gaussian profile. This allowed the interaction regions to be spaced more closely together and avoid overlapping them, which is necessary since the bichromatic force is a stimulated process. The apertures were opened to 11 mm, and did cause some diffraction at the edges, but not within the central w_{long} diameter at the 60% level of intensity.

A schematic for the arrangement of the beams for collimation in one dimension is shown in figure 4.8. Since the bichromatic force is unidirectional, we needed two interaction regions for collimation in one dimension. The interaction regions can be labeled by the sequence in which the atoms

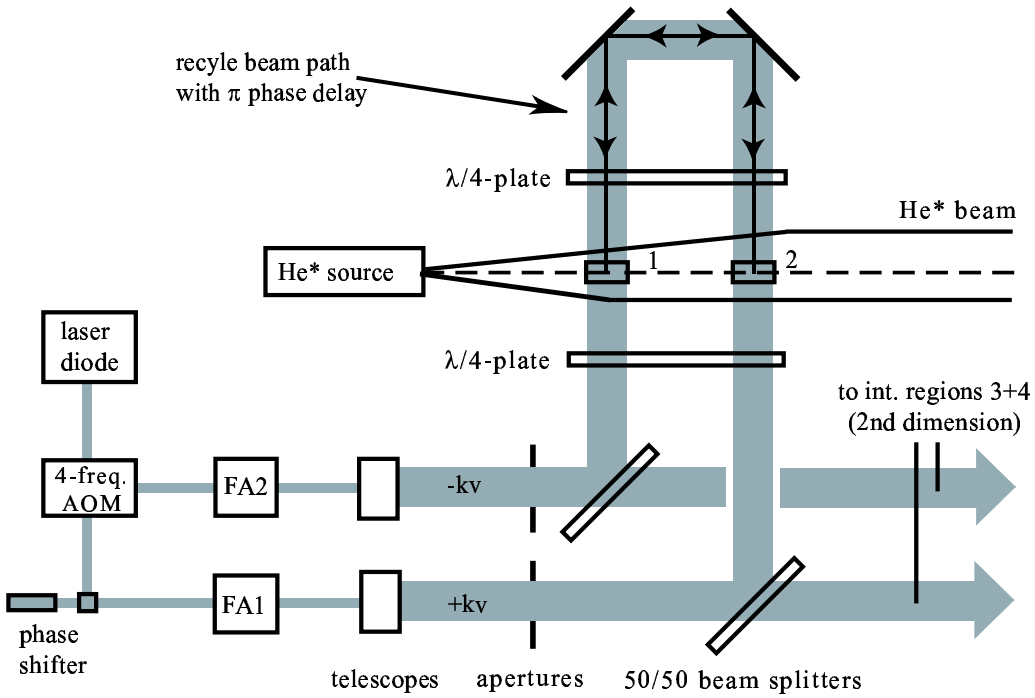

Figure 4.8 Schematic diagram showing how the bichromatic beams were delivered to the atomic beam. The relative spacing of the beams is not to scale (see text), and interaction regions 3 and 4 are not shown. Each pair of telescopes is represented by a single box.

transverse them. The "$-kv_c$" beam first enters interaction region 1, while the "$+kv_c$" beam first enters interaction region 2. After passing through the atomic beam the light beams are then recycled back onto each other to create two interaction regions comprised of counterprogating beams (see figure 4.8). The phase delay between the two beams was arranged (by the optical path length) such that "$+kv_c$" was $\pi/2$ ahead of "$-kv_c$" as each beam *first* crossed the atomic beam. The length of the recycle path was set to 125 cm (62.5 cm each way) corresponding to a phase change of π for each beam. Thus,

as "$+kv_c$" was recycled back, it gained π phase so that at interaction region 1, "$-kv_c$" was $\pi/2$ ahead of "$+kv_c$". Likewise, as "$-kv_c$" was recycled back, it came to be $\pi/2$ ahead of "$+kv_c$" at interaction region 2 as well.

Figure 4.8 is a simplified schematic. For example, there was a third mirror in the recycle path that folded the path to take up less space. Moreover, the first interaction region is $\sim$ 0.5 cm from the source skimmer, and the distance between the two interaction regions is $\sim$ 1 mm. In reference to figure 3.4 and the ports labeled "interaction region": the two bichromatic beams come up to the atomic beam through the lower port on the side facing away from the reader (at an angle of 45°to the horizontal), and out to the recycle path through the upper port facing the reader.

To achieve collimation in the dimension orthogonal to the one just described, mirrors reflecting the bichromatic beams up into the atomic beam were replaced with 50/50 beamsplitters. The transmitted beams were then reflected *under* the vacuum chamber and up through the lower port facing the reader in figure 4.8, orthogonal to the beams reflected off of the 50/50 beamsplitter. In being sent under the vacuum, the beams were also redirected slightly along the direction of the atomic beam, so that in eventually crossing the atomic beam they do not overlap with interaction regions 1 and 2. The interaction regions formed by the recycling of these beams formed interaction

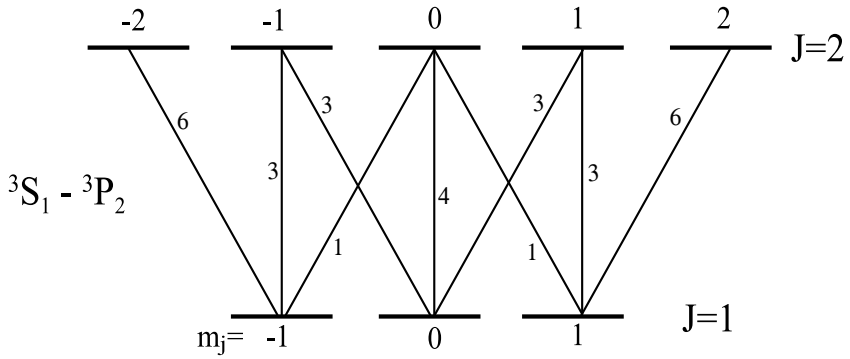

Figure 4.9 Transition strengths for the operative transition in He. The strength is normalized to the weakest allowed transition. Note that transitions with $\Delta m_j = \pm 1$ are driven by $\sigma^{\pm}$ light.

regions 3 and 4, which were also closely spaced, so that the total length of all 4 interaction regions was within 5.5 cm of the skimmer. The addition of collimation in the second dimension required that the power in the beams (equation 4.4) be doubled to $\simeq$ 500 mW/cm^2. In this way, four interaction regions of eight counterpropagating multi-frequency beams were formed from a single diode laser.

The description of the bichromatic force has been for a two-level atom. Of course, real atoms have multiple levels. To physically approximate a two level atom, we used a cycling transition, in which decay from the excited to ground state is only to the sublevel most strongly coupled by the light. We used the 2^3S_1 ($J = 1$) to 2^3P_2 ($J = 2$) transition, either from the $m_j = 1$ to $m_j = 2$ or from the $m_j = -1$ to $m_j = -2$ sublevels (see figure 4.9). These transitions are driven with circularly polarized light, σ^+ for the former,

and σ^- for the latter. At each interaction region, the beams need to both be either σ^+ or σ^-, so that they are driving the same transition. Since the beams are counterpropagating, they need to have opposite helicity (or handedness) to have angular momentum that points in the same direction [58]. To arrange this condition, the two $\lambda/4$-plates in figure 4.8 had their fast axis aligned [34], so that combined they acted as a $\lambda/2$-plate (rotating linear polariztion by 90°) on a beam passing through them. When light coming in from opposite sides of the atomic beam had parallel linear polarization, passing through the aligned $\lambda/4$-plates from opposite sides set up the desired arrangement of helicities[3]. Coming up to the vacuum chamber, "$-kv_c$" and "$+kv_c$" were set to have orthogonal linear polarization, so that if interaction region 1 has σ^+ on σ^+ light, then interaction region 2 had σ^- on σ^- light.

4.5 Additional Molasses Stage

In the latter stages of the experiment, we added an additional collimation stage of optical molasses. To generate the light, a third AOM was inserted before the AOM for saturated absorption spectroscopy. This AOM shifted the light by only 82 MHz, rather than the 90 MHz of the SAS AOM.

[3] If the light coming from opposite sides had orthogonal linear polarization, then after the waveplates the light would be σ^+ on σ^- on the atomic beam, which was experimentally confirmed using magnetically tuned velcoity selective resonances [8].

Thus when the $\omega_\ell - \delta + 90$ MHz light was locked to atomic resonance, the first order diffracted light of this third AOM was only -8 MHz red-detuned from atomic resonance (the other frequency in the bichromatic beam was then $\sim$ 130 MHz off resonance, and so too far detuned to have an effect on the molasses). The red-detuned light was then injected into a third fiber amplifier (one of the older models) to provide any range of s desired. The beam was then expanded and collimated by a spherical telescope and cylindrical telescope, with $w_{long} \sim 15$ mm and $w_{short} \sim 3$ mm. Apertures of ~ 25 mm diameter were used to trim the beam. Another set of mirrors directed the molasses beam through the atomic beam parallel to the bichromatic beams just several mm downstream from the 4th interaction region. However, the beam was not split with 50/50 beamsplitters, as were the bichromatic beams, but rather passed through the atomic beam once in each direction, overlapping with itself each time, in a pseudo bow-tie configuration (see figure 4.10).

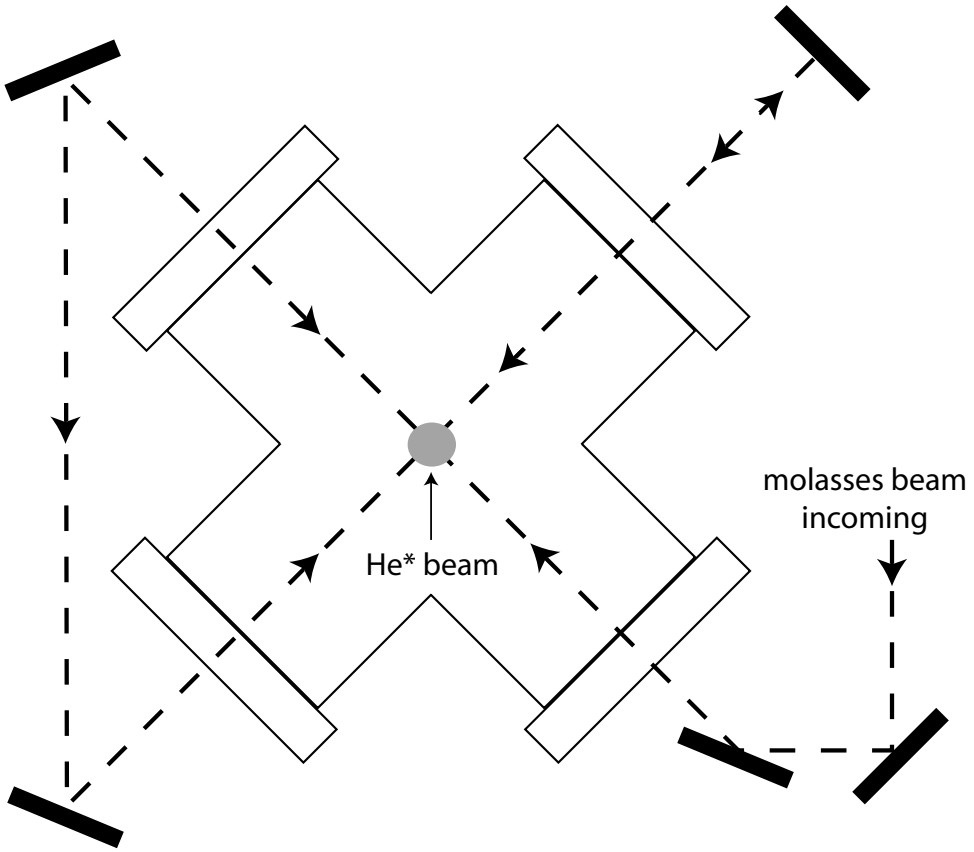

Figure 4.10 A simple drawing that shows how the single red-detuned molasses beam was delivered to the atomic beam. The upper right mirror is set to retro-reflect the beam back onto itself. In this drawing, the atomic beam is coming out of the page, and the bichromatic interaction regions are behind the molasses beam.

Chapter 5

Bichromatic Slowing

Before presenting the results of the collimation experiment, it is worthwhile to briefly discuss some of the other work in the lab using the bichromatic force to manipulate a metastable helium beam. Prior to collimation, we used the bichromatic force to slow and also to accelerate the atomic beam.

The experimental setup was conceptually the same as that described in the previous two chapters, however, there were several significant differences. Since the aim was longitudinal slowing of the beam, only one bichromatic interaction region was needed. Mirrors inside the vacuum were used to direct the counter-propagating bichromatic beams to be at approximately 1° to the atomic beam, so that only a minor component of the force was transverse to the atomic beam. Also, the bichromatic detuning, δ, was significantly larger than that used for collimation. With $\delta = 184\gamma = 2\pi \times 300$ MHz, the velocity

range of the force was $\approx \delta/k \approx 325$ m/s. For slowing, the center of the force was shifted to be near the center of the longitudinal velocity distribution (1000 m/s) rather than to push to $v = 0$ as in collimation. In order for the bichromatic light to have the appropriately scaled $|\Omega_r| \sim \sqrt{\frac{3}{2}}\delta \sim 220\gamma$, the bichromatic beams were focused and collimated to have a Gaussian waist $\approx$ 0.8 mm with a peak intensity of 16 W/cm^2. With this alignment and beam waist, the bichromatic beams had a ~ 5 cm overlap with the aperture-defined atomic beam, representing a significant reduction in slowing length as compared to radiative force slowing.

A time of flight (TOF) detection scheme, comprised of a 200-μm slit affixed to a tuning fork chopper which was mounted on a linear motion feedthrough, was used to measure the velocity distribution of the beam. Typical results of the bichromtaic slowing are shown in figure 5.1. The atoms that fell within the range of the force were slowed by the expected ~ 325 m/s. The resulting velocity spread of the slowed atoms was a factor of 3 smaller than the spread of initial velocity distribution. This reduction is due to the accumulation of atoms at the edge of the velocity range of the force, where a sharp drop-off in force magnitude occurs. Acceleration of the beam was also possible, by merely changing the spatial phase of the counter propagating beams from $\phi = \pi/2$ to $\phi = -\pi/2$. The observed result is shown in figure 5.2. The switch of the sign

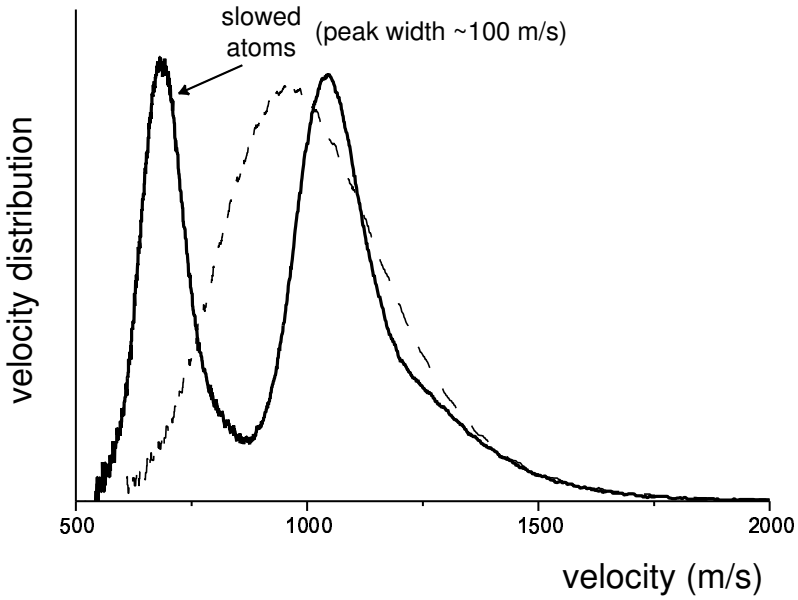

Figure 5.1 Slowing the atomic beam with bichromatic detuning $\delta = 184\gamma$. The expected velocity range of $\sim$ 325 m/s is observed. The slowed atoms also have a velocity width smaller than that of the original distribution.

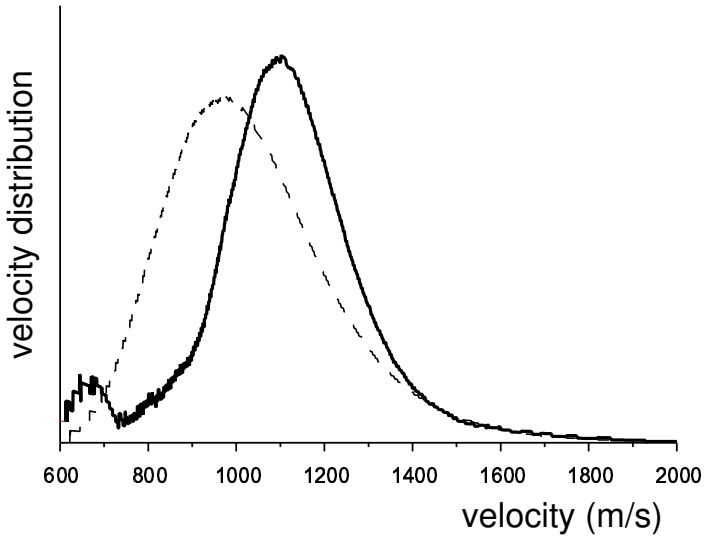

Figure 5.2 Acceleration of the atomic beam with bichromatic detuning $\delta = 184\gamma$. The expected velocity range of $\sim$ 325 m/s is observed. To achieve the acceleration, the phase of the counterpropagating bichromatic beams was switched from that of figure 5.1.

of the force when the phase is switched by π is a signature effect of the bichromatic force. More details on these experiments with a bichromatic detuning of $\delta/2\pi = 300$ MHz can be found in [35, 59].

With the success of these experiments, the next goal was to slow the beam using a bichromatic detuning of $\delta/2\pi = 600$ MHz. This required the maximum power output of the 1 W fiber amplifiers in use at the time. Unfortunately, the slowing experiments with larger detuning were not successful and revealed a possible upper limit to the magnitude of the force. As the bichromatic detuning increases, the length of each bichromatic beat decreases, which makes for a larger change in phase between the beams for a fixed change in distance within the interaction region. With 600 MHz, the phase changes by π in just 12.5 cm, just over double the interaction length.

While presenting the 300 MHZ experiments at several conferences, we were frequently asked why we weren't using the bichromatic force to collimate rather than slow the atomic beam.

Chapter 6

Bichromatic Collimation

6.1 Introduction

Due to the low efficiencies ($\approx 10^{-5} - 10^{-4}$) at which metastable rare gas atoms are produced in typical gas discharge sources, there has always been great interest in effective ways of collimating beams of these atoms to increase their intensity and brightness [8]. Atomic flux and/or beam brightness are important considerations for a variety of experiments with these atoms, such as neutral atom lithography [60, 61], trap loading for Bose-Einstein condensation, photoassociation spectroscopy and ultra-cold collisions [62–65], and precision measurements [66, 67]. The large magnitude and short interaction lengths of the bichromatic force make for an attractive method of improving beam intensity and brightness. Our results to date are presented in this chapter.

6.2 Collimation in 1-Dimension

Successful one-dimensional collimation (that is, two pushes to $v_{tranverse} = 0$ from opposite directions) was first achieved with the older interaction chamber. With that chamber, optical access was limited to allow only collimation in one dimension and with the interaction regions centered at a point roughly 5 cm from the skimmer plate. Also, the MCP/phosphor screen detector was slightly closer, at 21 cm. An end on view of the collimation of the atomic beam as recorded from the phosphor screen is shown in figure 6.1 (all other presented results were obtained with the configuration described in previous chapters). To enhance the image in terms of change in atomic distribution, an image taken with lasers blocked is subtracted from an image taken with the lasers on. Before subtraction, an offset is added to the latter, since the image processing program cannot handle negative pixel values. Thus, the gray level of the image outside the circle of the phosphor screen represents a "zero" level, and areas darker than this level represent a removal of atoms. It can be seen in figure 6.1 that atoms are removed from the lower right (the push from interaction region 1) and upper left (the push from interaction region 2), and accumulated in the center. The sharp contrast at the edge of the detector, along the pushes, suggests that atoms are collimated from outside the range of the detector. This corresponds to a collection of atoms from a

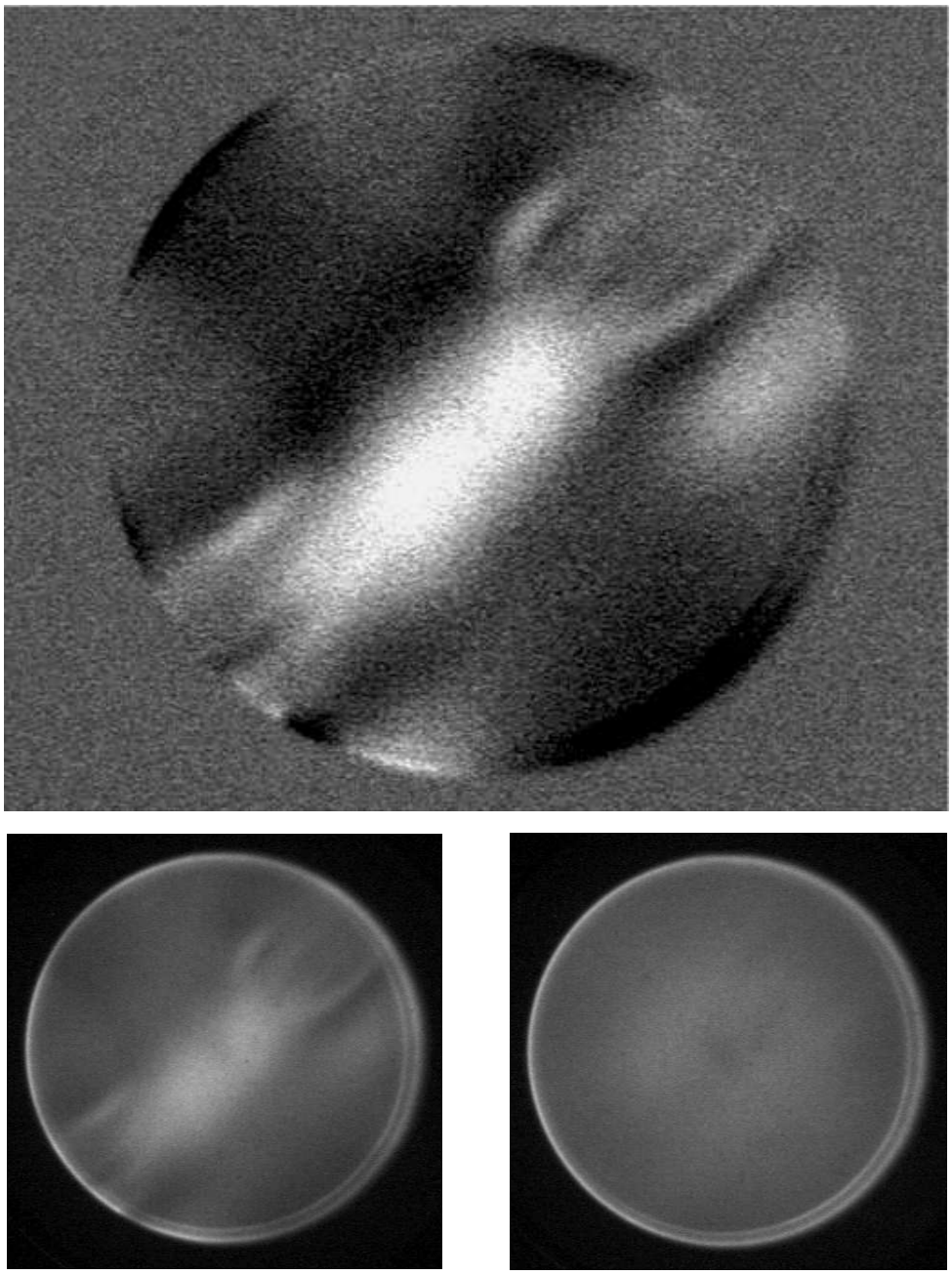

Figure 6.1 Collimation of the He* beam along one dimension. Smaller images are the raw pictures taken with the camera. The large image is a result of subtracting the two. Atoms are pushed to the center from the lower right and upper left. Note that atoms hitting the screen have transverse velocities within the range of ± 60 m/s.

full angle greater than 120 mrad (i.e. from transverse velocities greater than ±60 m/s). The peak of collected atoms has a width of $\sim$ 8 mm transverse to the dimension of collimation. Extended back to the interaction regions at 5 cm, this width corresponds quite well to w_{short}, the 60% Gaussian diameter of the short axis of the bichromatic beams. Outside of this 60% level the Rabi frequency conditions necessary for the bichromatic force are not well met, and other effects prevail, as can be seen in figure 6.1. The other effects are not yet well understood, since our primary focus was bichromatic collimation, and they are observed even in the central portion if other conditions for the bichromatic force are intentionally mismatched, such as removing one of the frequency components of the light field, or changing the phase.

It can also be illustrative to view profiles of the pixel values from the raw images (figure 6.2). In these plots it can be clearly seen that atoms have been collimated from the sides to the center. However, the plots also demonstrate the limitations of using the MCP/phoshphor screen for quantitative measurements. In figure 6.2 there are more atoms "missing" than collimated into the peak. We know from other measurements (such as with the SSD, as will be shown) that atoms are not being pushed away from the center, which suggests that the visual detection is subject to non-linearities.

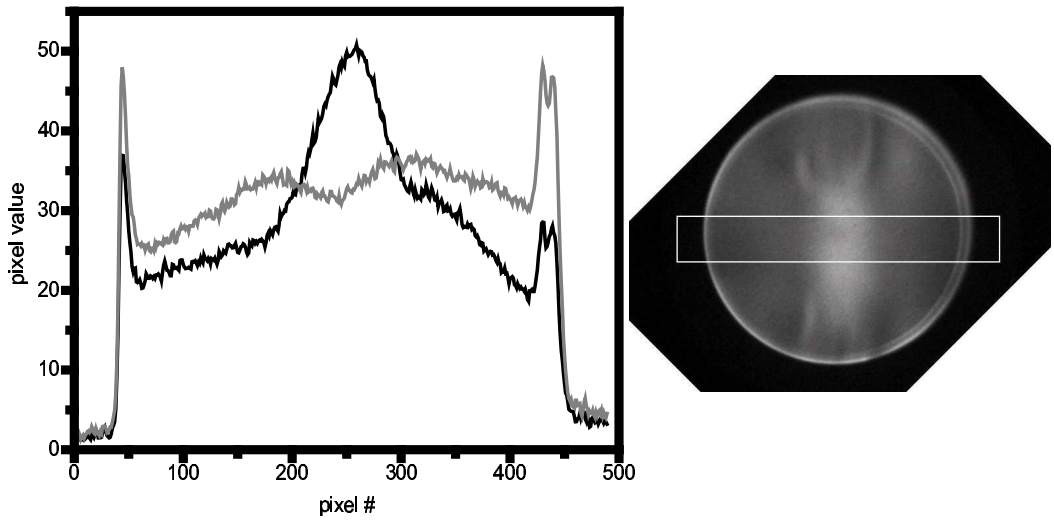

Figure 6.2 Profile plots from the raw images in figure 6.1. The gray line is with lasers off, the black line (with peak in center) is bichromatic collimation. The image on the right shows the area over which the profiles were taken, using as example the collimation image. The pixel value at each horizontal pixel is an average over the vertical range of pixels. The image and chart are not drawn with the same horizontal scale. 410 pixels corresponds to 2.54 cm. Thus the capture range is greater than $\frac{2.54\text{cm}}{21\text{cm}} \sim 120\text{mrad}$. The sharp features at either end of the profile are due to edge effects and non-linearities of the phosphor screen.

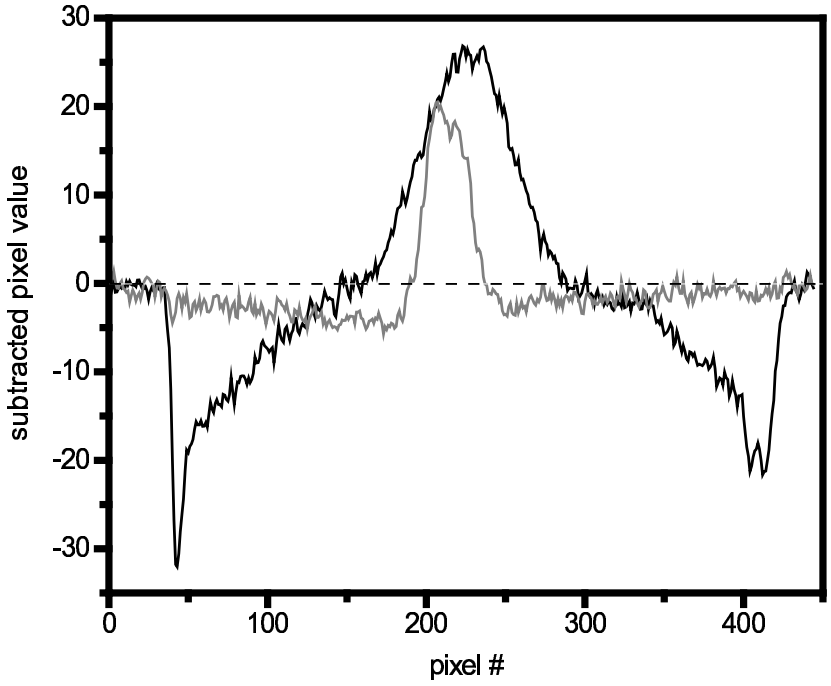

Figure 6.3 Profile plots for bichromatic collimation (black) and optical molasses (gray). Here the background profile has been subtracted from the collimation profile to show absolute change in signal.

The effectiveness of the bichromatic force can be seen when the collimation is compared to collimation achieved with an optical molasses (figure 6.3). The optical molasses was created by a single frequency of light injected into the fiber amplifier, with the same gain settings as used for bichromatic light (s$\sim$4000) and red-detuned $\sim$15 MHz from resonance. The figure shows that while optical molasses may cool the atoms to a smaller width, bichromatic collimation collects a much larger number of atoms from a much greater range of velocities. Note that comparisons cannot be made between figure 6.3 and figure 6.2 since the images from which the profiles were extracted were taken

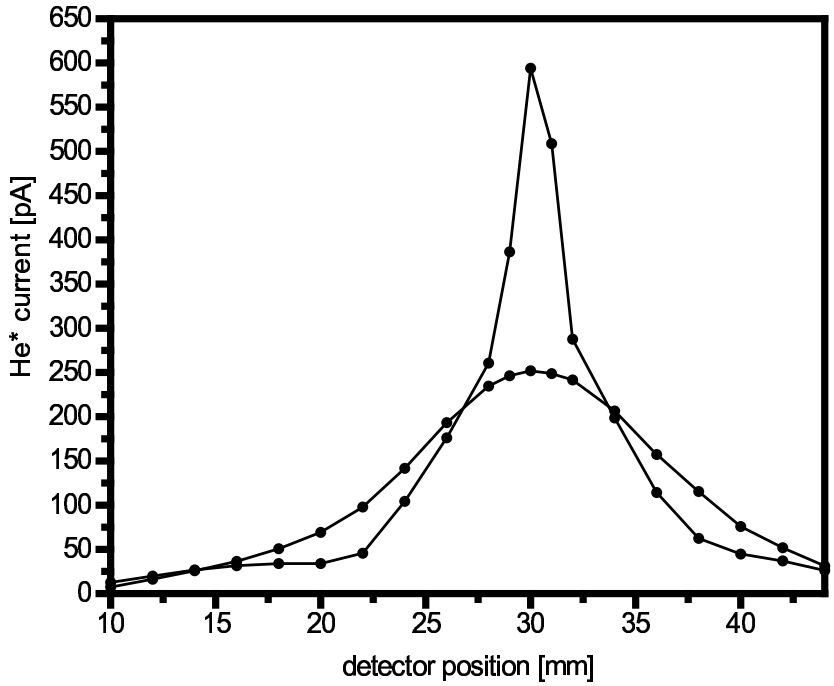

Figure 6.4 SSD scan of 1D bichromatic collimation. The scan taken with lasers blocked is also shown. The range of the scan is limited on the right due to the deflection plates blocking the uncollimated beam. Both scans have had the UV contribution removed. Curves are drawn to guide the eye.

with *different* MCP and phosphor screens, and also the latter is obtained with the new interaction chamber.

We were able to view the full range of velocities from which atoms were collected by scanning across the atomic beam with the SSD's. Figure 6.4 shows an SSD scan across the atomic beam at 16 cm from the skimmer. The quantitative measurement shows a conservation of atoms in collimation. The scan also shows a collection of atoms from ± 14 mm, corresponding to a full angle of 175 mrad, or capture of atoms with ± 87 m/s. The largest capture

angle previously reported for a He* beam is 30 mrad [68]. This is also larger than the expected capture range of $\delta/k = 65$ m/s. The observed capture range can be explained in part by the fact that as the atoms fly through the interaction region, they experience a changing Rabi frequency due to the Gaussian longitudinal profile of the bichromatic beams. Numerical calculations show that as the Rabi frequency lowers from $\Omega_r = \sqrt{\frac{3}{2}}\delta$, the peak force in the center of the force profile decreases, but the force profile also broadens and increases in magnitude for higher velocities (see figure 6.5). So, if what the atom "sees" is an average of these profiles, then it experences the strong force in the center of the profile, and in the broadened wings.

Using equation 6.1, we have $5.3 \times 10^9 \frac{\text{atoms}}{\text{s}}$ into the 1 mm diameter aperture of the SSD, for a flux density of $6.7 \times 10^9 \frac{\text{atoms}}{\text{s}\cdot\text{mm}^2}$. This is a factor of 2.5 increase in flux over the uncollimated beam. A more detailed discussion of increase in flux density will follow as the two dimensional collimation results are presented.

6.3 Collimation in 2-Dimensions

By implementing two more interaction regions, we were able to collimate the atomic beam along the second dimension. The beams are arranged as described in section 4.4.2, with interaction regions 1 and 2 collimating the

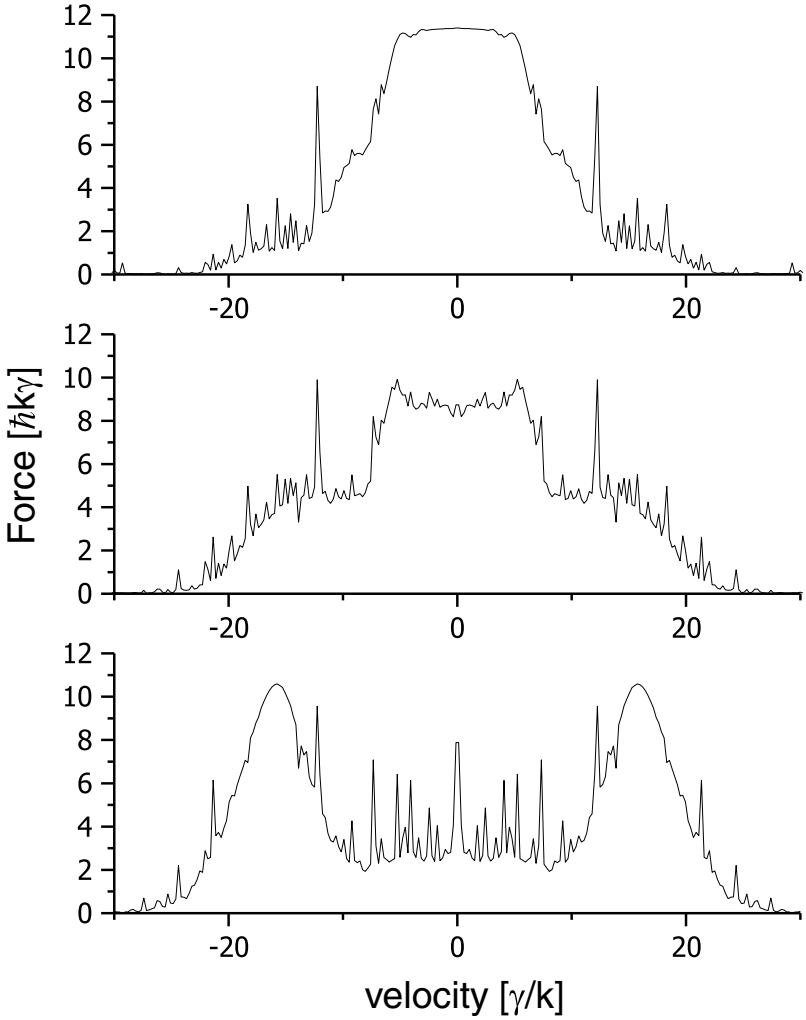

Figure 6.5 Calculated bichromatic force vs. velocity profiles for $\delta = 37\gamma$ and $\phi = \pi/2$ with various values of the Rabi frequency. In the top plot, $\Omega_r = \sqrt{\frac{3}{2}}\delta = 45\gamma$, in the middle $\Omega_r = 42\gamma$, and in the bottom $\Omega_r = 37\gamma$. The velocity range of the force is expected to be $\approx \delta/k = 37\gamma/k$, but at lower intensity broadens out. $\Omega_r = 37\gamma$ corresponds to a $\sim 67\%$ reduction in intensity from the peak intensity of the bichromatic beam. Note the force axis is scaled by twice the radiative force, $F_{rad} = \frac{\hbar k\gamma}{2}$.

beam as shown in figure 6.1, and the additional interaction regions 3 and 4 giving pushes at 90° to 1 and 2. The first two images of figure 6.6 show the results of each of the pairs of interaction regions acting alone on the atomic beam. The images have been processed in the same way as presented for figure 6.1. Note that in the right-most image, the collimated atom peak (from interaction regions 1 and 2) has a dimension transverse to the laser beam directions that is larger than the imaging detector (in contrast to the image of figure 6.1). This is because the interaction regions have been moved to be directly after the skimmer, so that more atoms may be collimated. In being closer to the skimmer, w_{short} of the bichromatic beams now subtends a larger solid angle downstream from the source. Interaction regions 3 and 4 are farther away from the skimmer, and thus the range of atoms, with velocities transverse to the pushes, that can be collimated is smaller than for collimation along the first dimension, as seen on the screen (middle image of figure 6.6). However, this does not result in a severe limit to the amount of the beam that is collimated when the four interaction regions are acting together. As well as capturing atoms from ±87 m/s, collimation in the first dimension also collects atoms from a large range of transverse velocities (transverse to the dimension of collimation) to the center of the beam. These atoms are left with velocities (along the dimension of the first collimation) small enough so that they are

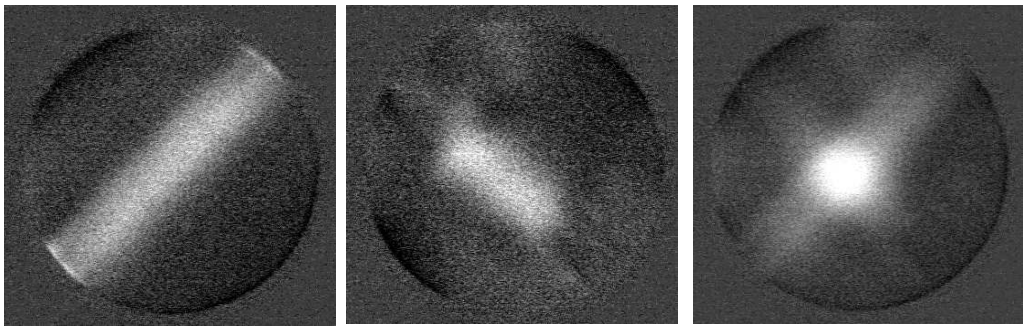

Figure 6.6 Images of 2D collimation. In the image on the left, only interaction regions 1 and 2 are active. In the middle image, only interaction regions 3 and 4 are active. And in the image on the right, all four interaction regions are active.

then all captured within the transverse range of collimation in the second, orthogonal dimension (interaction regions 3 and 4). The product is the image on the right in figure 6.6. The resulting peak is symmetric along the two axis of collimation. One might not expect this, since the beam has expanded slightly more before the second collimation. However, the remaining velocity spread of the atoms washes this out, and the symmetry is bourne out in the orthogonal SSD scans at 56 cm.

A more dramatic way of presenting the collimated peak than figure 6.6 is in a surface plot based on the gray-scale values of the pixels in the image. Such plots are easily created with ImageJ, and a typical plot is shown in figure 6.7. The arrows drawn to the side represent the direction of each push from the individual interaction regions. As in the other images, the surface level outside the circle of the detector represents a zero level, and levels below this

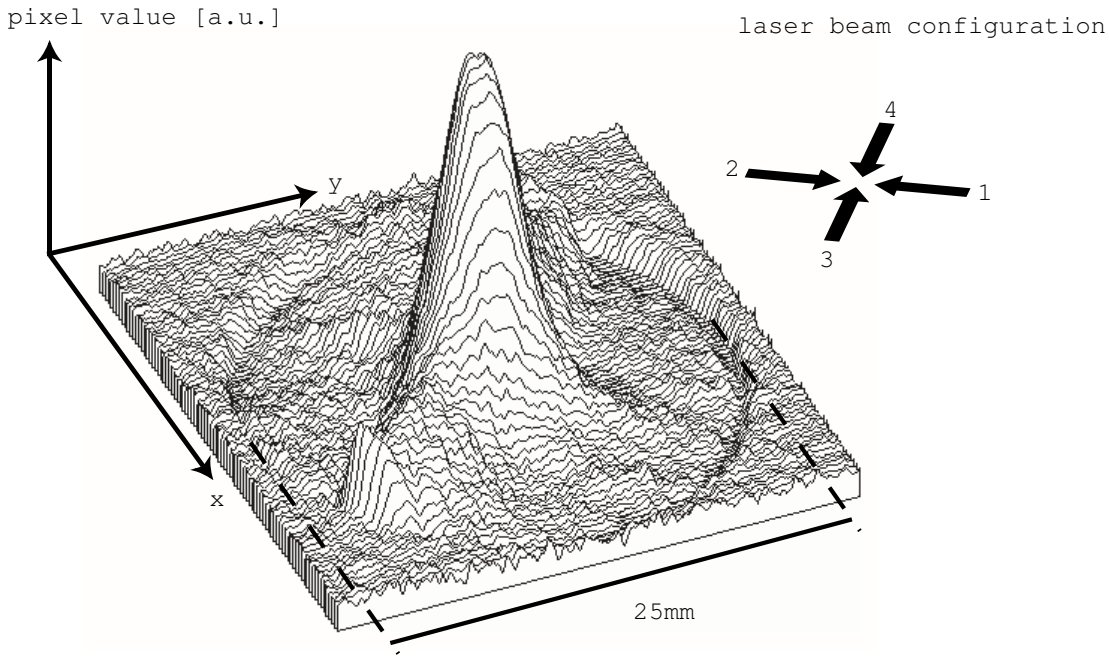

Figure 6.7 Surface plot of the right-most image of figure 6.6, created with ImageJ. Positive pixel value represents an accumulation of atoms. Arrows show the direction of each push, labeled by the designation of the interaction region. The peak in the foreground of the circle is an edge effect of the detector.

inside the detector represent a removal of atoms. Viewing the phosphor screen in real-time, and analyzing the images and surface plots provide an incredibly useful tool in aligning all the bichromatic beams, and configuring each of the pushes to "deposit" atoms at the same average transverse velocity. Alas, no real quantitative information of atom flux can be obtained from the images.

In order to obtain an accurate measure of the degree to which the beam was collimated, we measured the FWHM diameter of the beam in two places: with the SSD at 16 cm and an SSD at 56 cm. The FWHM divergence

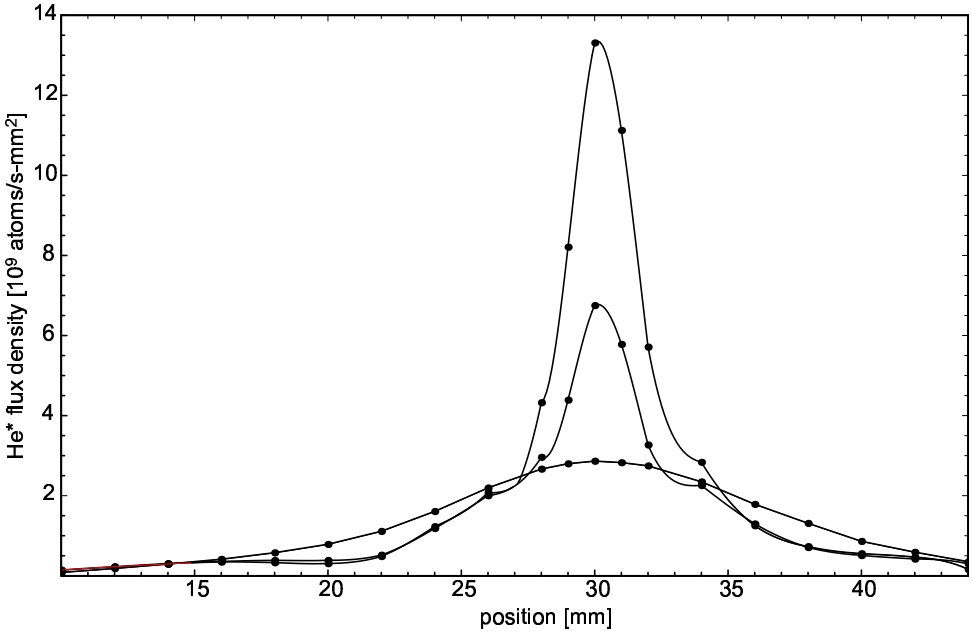

Figure 6.8 Stainless Steel Detector scan across the atomic beam with 2D collimation at 16 cm from the skimmer. 1D collimation and lasers off signal are shown for comparison. Derivation of flux density from raw signal is described in the text. Curves drawn to guide the eye.

of the beam, Θ, is simply the difference between the two measured diameters divided by the distance between them. This also gives the remaining transverse velocity spread of the atoms: $v_t = \pm\frac{\Theta}{2}\overline{v}_{long}$. Typical scans of 2D collimation for both SSD's are shown in figures 6.8 and 6.9. We convert the measured I from the SSD to an atomic flux density (or intensity) via:

$$\Phi_{\mathrm{He}^*} = \left(I\left[\frac{\mathrm{C}}{\mathrm{s}}\right]\right)\left(\frac{1\ \mathrm{e}^-}{1.6\times10^{-19}\mathrm{C}}\right)\left(\frac{1\ \mathrm{He}^*}{0.7\ \mathrm{e}^-}\right)\left(\frac{1}{\pi(0.5\ \mathrm{mm})^2}\right) \tag{6.1}$$

where 0.5 mm is the radius of the SSD aperture. The UV contribution is removed by subtracting 25% of the background (lasers blocked) signal from each of the scans.

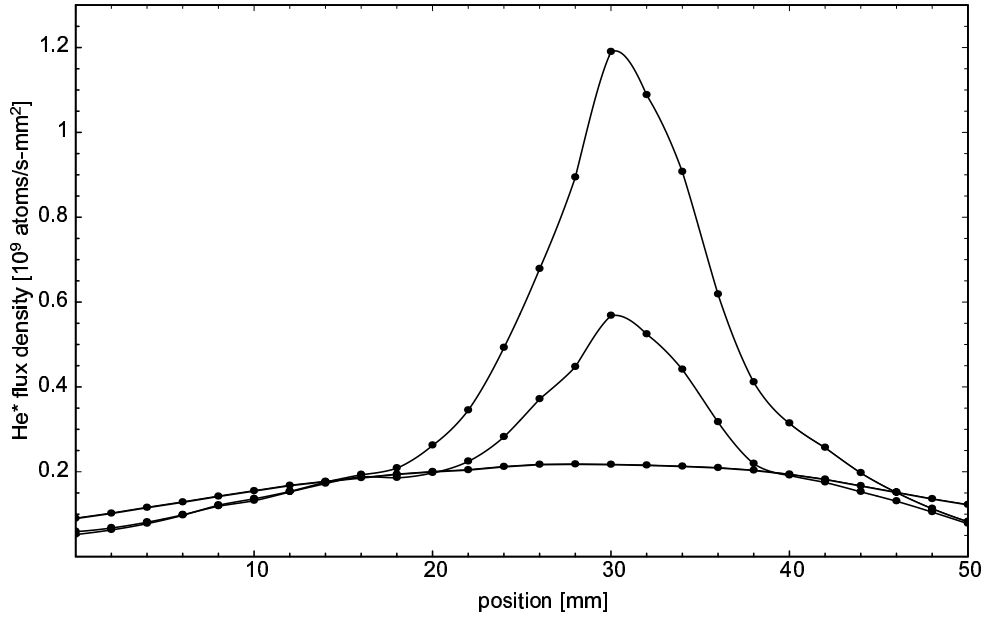

Figure 6.9 Stainless Steel Detector scan across the atomic beam with 2D collimation at 56 cm from the skimmer. The highest peak is 2D collimation. 1D collimation and lasers off signal are shown for comparison. Derivation of flux density from raw signal is described in the text. Note that this SSD has the same scan range as the SSD at 16 cm, but since it is farther downstream, it can only measure the central HWHM of the uncollimated beam. Curves drawn to guide the eye.

With 2D collimation, the scans show that the atomic beam spot size was reduced to 3 mm FWHM at 16 cm from the source, and to 10 mm at 56 cm. This gives a divergence of ∼17.5 mrad, which corresponds to average residual transverse velocities of $v_t \approx \pm 9$ m/s. This width agrees well with a rough estimate. We can estimate, based on the slope of the force profile near $v = 0$ in figure 2.7, a damping constant for the bichromatic force of $\beta_b \sim (14\hbar k\gamma)/(15\gamma/k)$. With the high intensity beams, we estimate a dipole force diffusion constant from Eq 4.6 of [15] to be $D_b \sim (\hbar\delta k)^2/(2\gamma)$ (four beams $\Rightarrow \omega_1 \sim 4\delta$). Thus, with $\delta = 37\gamma$, $k_B T_b \equiv D_b/\beta_b \sim 1500\hbar\gamma/2$, or 1500× the Doppler temperature, which gives $v_t \approx \pm 11$ m/s. However, the force profile of figure 2.7 is the result of two spatially separated interaction regions, each pushing in only one direction. So strong comparisons of the measured value to this estimate cannot be made.

In the data in figures 6.8 and 6.9, the center peak flux density from 2D collimation was $13.3 \times 10^9 \frac{\text{atoms}}{\text{s-mm}^2}$ at 16 cm, and $1.2 \times 10^9 \frac{\text{atoms}}{\text{s-mm}^2}$ at 56 cm, while the uncollimated beam had $2.8 \times 10^9 \frac{\text{atoms}}{\text{s-mm}^2}$ at 16 cm and $0.2 \times 10^9 \frac{\text{atoms}}{\text{s-mm}^2}$ at 56 cm. The lower signals at 56 cm correspond exactly to the spread of the uncollimated beam and the residual spreading of the collimated beam. That is, the ratio of the beam flux at 16 cm to beam flux at 56 cm is equivalent to the square of the ratio of the FWHM diameter of the beam at 56 cm to

the FWHM at 16 cm. This consistency between detectors lends confidence to the measurements, and also suggests that at most only a few percent of the metastables in the beam are lost due to intrabeam or background gas collisions. The ratio of collimated flux density to uncollimated flux density is greater at 56 cm than at 16 cm, consistent with the beam being collimated to a smaller divergence.

We obtained an even larger flux density in the collimated beam by raising the current feeding the discharge to 12 mA, which increased the total metastable output by $\sim 50\%$. We estimated, based on past TOF measurements [35], that the mean longitudinal velocity of the atoms increased no more than $\sim 5\%$. This estimate is supported by the fact that we did not observe any significant change in the FWHM size of the uncollimated or collimated beam at 16 cm or at 56 cm. With this increased current, the peak intensity of the collimated beam was $1.8 \times 10^9 \frac{\text{atoms}}{\text{s-mm}^2}$, a factor of 6 larger than for the uncollimated beam ($0.3 \times 10^9 \frac{\text{atoms}}{\text{s-mm}^2}$), the same factor as with 6 mA. The total atomic flux in the beam can be roughly estimated by multiplying the peak instensity by the FWHM area of the beam. Then the integrated flux for the collimated beam was $1.4 \times 10^{11} \frac{\text{atoms}}{\text{s}}$. However, with the larger spot size, the total flux in the uncollimated beam was $5.9 \times 10^{11} \frac{\text{atoms}}{\text{s}}$, meaning that we collected only $\sim 24\%$ of the total output of the source into the collimated

beam. This inefficiency will be discussed in a subsequent section.

6.4 Additional Compression with Optical Molasses

After the success of the bichromatic collimation, we decided to attempt further velocity compression of the ±9 m/s beam with an ordinary optical molasses. With the compact length of the bichromatic collimation regions, and the large amount of optical access granted by the 4" windows, we were able to insert the optical molasses stage directly downstream from the 4th interaction region, minimizing the spatial spread between the two stages. The method used for producing the laser light for the molasses, and how it was delivered to the atomic beam is described in Section 4.5. We chose a molasses detuning, δ_{mol}, of -8 MHz for a velocity capture range on the order of the residual ±9 m/s bichromatic beam spread. Other detunings within a few MHz of this were tried, but did not make a significant difference in the peak flux. The intensity of the light was chosen experimentally by adjusting the gain of the third fiber amplifier to maximize the atomic current into the aperture of an SSD. We found that $s \sim 70$ gave the largest flux density. With these parameters, the capture range of the force is estimated to be $\sim$ ±10 m/s

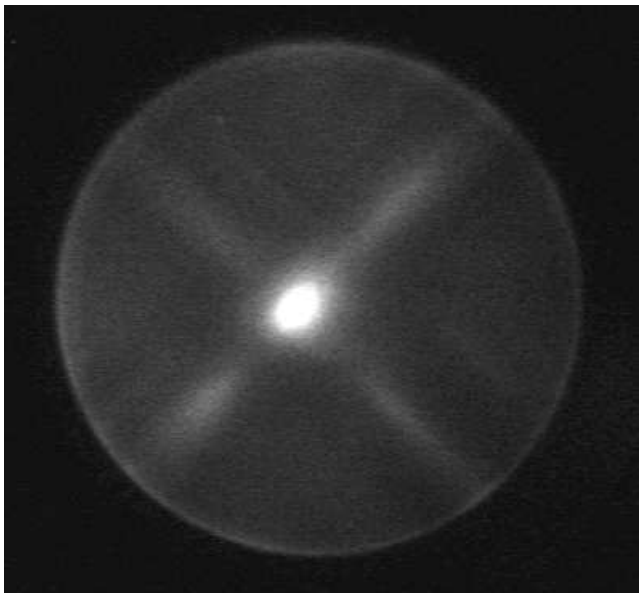

Figure 6.10 Phosphor screen image of the beam with both the bichromatic and molasses collimation stages active. The imaging system is near saturation at the beam peak. At the same detector settings, either stage acting alone has much lower contrast (see the surface plots in figure 6.11).

[8]. The experimentally difficult parameters in adding the molasses stage were aligning the molasses to be directly centered on the bichromatically collimated beam and for the resulting beam to still be in line with the SSD's.

Figure 6.10 is a phosphor screen image of the result of having the optical molasses stage well aligned to the bichromatic collimation stage. The spot is somewhat asymmetric since the uncollimated beam spreads out more before reaching interaction regions 3 and 4, than it does before the closer interaction regions 1 and 2. The extra compression of beam spread from the molasses makes this evident where it could not be seen before. The asymmetry is also seen in the orthogonal SSD scans at 56 cm. Figure 6.11 shows a surface plot

of an image such as figure 6.10. Also shown are the results of bichromatic collimation and molasses acting alone. The same detector settings were used for each image, and all plots have the same vertical scale. If the bichromatic collimation image were to be scaled on its own, it would be identical to figure 6.7. At these detector settings, the compressed beam nearly saturates the imaging system. So an offset is not added before the subtraction of the background, thus the flat level represents the zero level and/or the removal of atoms.

Figure 6.12 shows an SSD scan at 56 cm along the direction of the first dimension of bichromatic collimation, with the source discharge at 6 mA. The capture range of the molasses can be seen to span most of the bichromatic peak. In the scan of the molasses alone, and in the combined collimation, an accumulation of atoms above the uncollimated beam can be seen out to either side of the peak. This is because the SSD aperture is scanning through the center of the molasses, along the ridge seen in the image and surface plot. This ridge is produced by the small velocity range of the molasses force collimating atoms that are not collected into the bichromatic collimated beam. The extent of the ridge is not suprising (it is the full length of the MCP/phosphor screen as well as the SSD scan). Optical molasses does not have the strict intensity dependence of the bichromatic force, and so the dropoff of the molasses force due to finite w_{short} is not seen as it in the middle image of figure 6.6 for

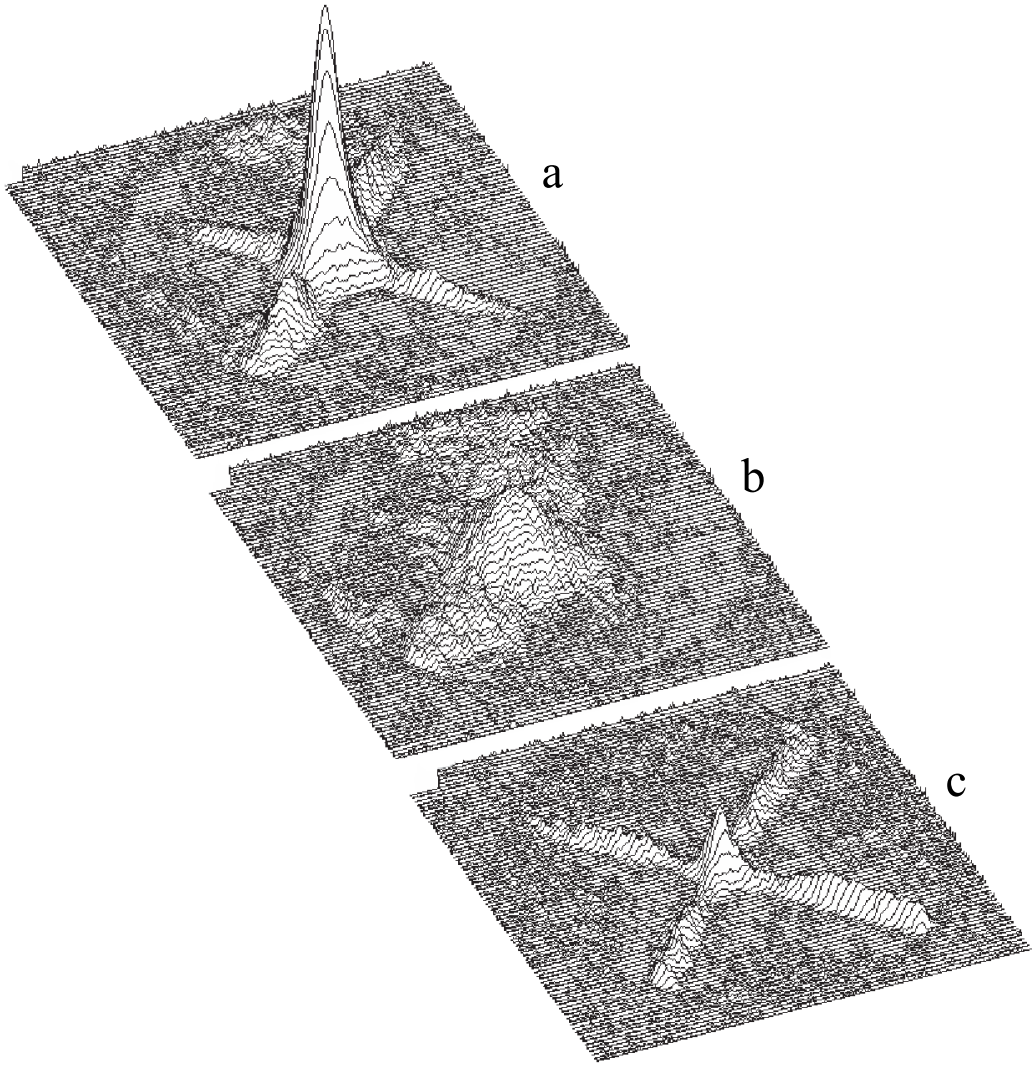

Figure 6.11 Plot (a) Bichromatic collimation followed by optical molasses. Plot (b) Bichromatic collimation alone. Plot (c) Optical molasses stage only. All plots are drawn with same vertical scale, and based on images acquired with the same detector settings. Plot (b) would be identical to figure 6.7 if rescaled.

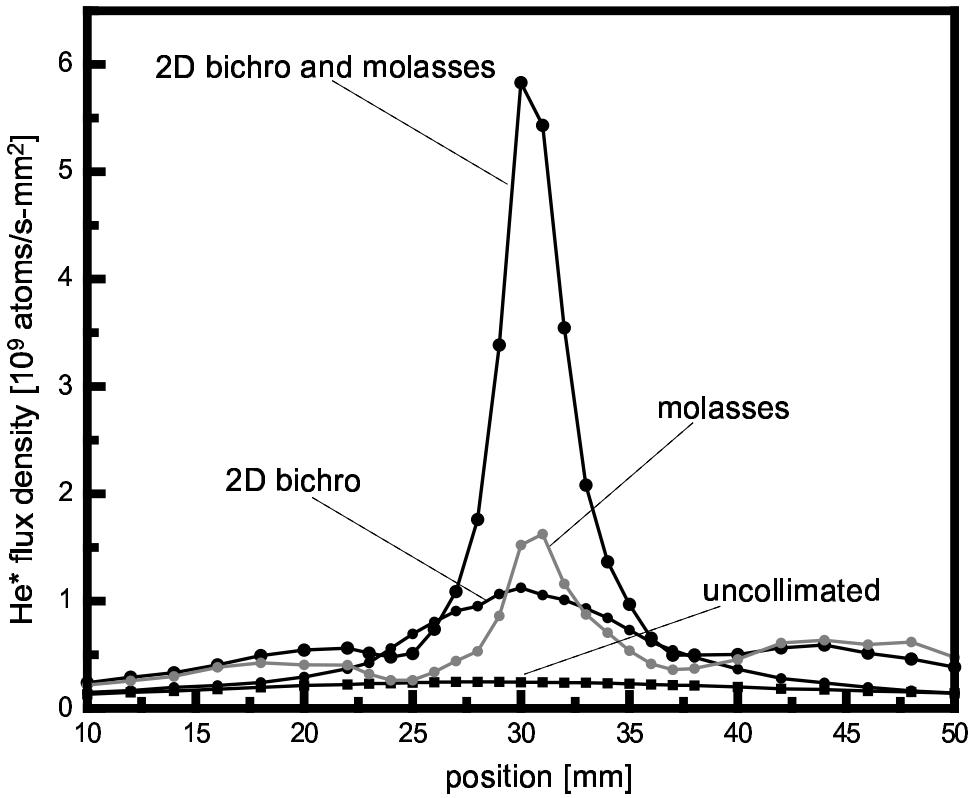

Figure 6.12 Stainless Steel Detector scans across the atomic beam at 56 cm from the skimmer. Here the source discharge is at 6 mA. Derivation of flux density from raw signal is described in the text. Note that the signal with bichromatic collimation AND optical molasses is greater than the sum of either acting alone. Curves drawn to guide the eye.

bichromatic collimation. There is a dip in the ridge near the shoulder of the collimated beam, this is other dimension of the optical molasses collimating atoms into the center.

The scans show that while molasses may create a higher flux density in the center of the beam, bichromatic collimation collects a greater number of atoms into the central peak. Moreover, it can be seen how bichromatic collimation and subsequent optical molasses combine to create a larger flux

density. Bichromatic collimation collects atoms from a wide angle of divergence into a spot with velocity width within the capture range of the molasses. The molasses then further compresses this beam to narrower velocities and thus a smaller angle of divergence, resulting in greater peak flux. The combined action of both is much greater than the sum of both acting alone, creating a flux density 30 times greater than the uncollimated beam. Raising the source current to 12 mA resulted in a peak intesity of $9.0 \times 10^9 \frac{\text{atoms}}{\text{s-mm}^2}$ into a 3.5mm $\times$ 5mm FWHM spot size. The total flux in this collimated beam was then $\sim 1.2 \times 10^{11} \frac{\text{atoms}}{\text{s}}$, containing most of the atoms collected into the bichromatic peak. The difference can possibly be accounted for in that the SSD at 56 cm might not be going through the exact center of the molasses compressed beam. A misalignment of $\gtrsim 0.5^\circ$ between the $\vec{k}$ of the molasses laser beams and $\vec{v}_{long}$ of the atomic beam could move the collimated beam from being directly on the SSD aperture to being one full width off of the aperture. Also, some of the atoms in the wings of the bichromatic collimated peak may fall outside the capture range of the molasses.

Another difficulty arises in that it is no longer straightforward to measure the divergence of the beam. The FWHM measured at 16 cm by the SSD was ~ 2 mm. However, this is near the resolution limit of the 1 mm diameter aperture of the SSD, and so the actual width may be smaller. This 2 mm

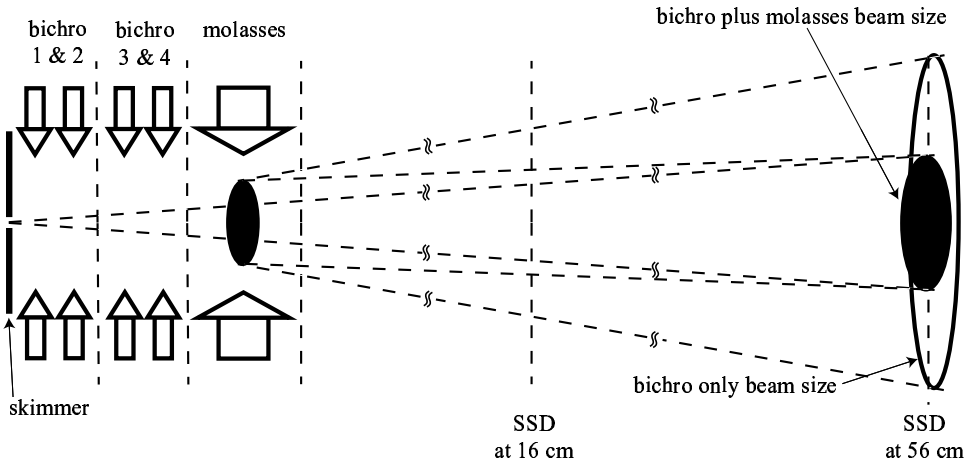

Figure 6.13 A schematic representation of two methods for determining the divergence of the atomic beam collimated by both the bichromatic force and an optical molasses. An upper limit to the divergence can be obtained from the angle that the measured FWHM at 56 cm subtends from the skimmer. Another estimate is obtained using the spot size of the bichromatic-force collimated beam at the molasses stage. Note that the distances to the SSD's are not drawn to scale, and that the divergences are exaggerated for clarity.

FWHM gives at 16 cm gives a lower limit to the divergence of the beam (3.8 mrad $\rightarrow \pm 1.9$m/s). An upper limit can be obtained by assuming the 3.5 $\times$ 5 mm spot size at 56 cm has diverged directly from the skimmer (7.5 mrad $\rightarrow \pm 3.8$m/s, see figure 6.13). Another estimate may be obtained by extending the known divergence of the bichromatic-only collimated beam back into the center of the molasses stage to find the FWHM size of the beam there and then assuming that the molasses compressed beam starts from this size. This gives a divergence of 4.4 mrad, for a velocity spread of ± 2.2 m/s. The SSD at 16 cm and prior charged particle deflection is currently undergoing re-design to allow a finer resolution scan (the deflection plates had to be moved farther

from the skimmer (closer to the SSD) to allow room for the molasses beams).

Based on equation 1.6, we estimate a molasses damping coefficient $\beta \sim \hbar k^2/10$ for the molasses parameters $s \sim 70$ and $\delta \sim 5\gamma$. In the molasses, the heating about $v = 0$ caused by spontanteous emission results in diffusion in momentum space. Since $s \sim 70$ is a significant intensity, we again use the estimate of [15] to find a diffusion coefficient $D_0 \sim 5\gamma(\hbar k)^2$. Then the steady-state temperature within the molasses is $k_B T \equiv D_0/\beta \sim 100 \times \hbar\gamma/2$ (100× the Doppler temperature, $\hbar\gamma/2k_B \simeq 40\mu K$), a velocity spread of ±2.8 m/s. This falls well into the range of the experimental estimations of this velocity spread. It should be noted that in the high intensity molasses, there may be other features of the resulting atomic velocity distribution [15], however, they would be below the limit of the resolution of the measurement. Also, the molasses interaction time is quite short, compared to the $1/e$ molasses damping time, $M/\beta \sim 20/\omega_r \sim 76$ μs. The interaction length is only ~ 25 μs long (25 mm and $v_{long} \sim 1000$ m/s).

A typical figure of merit for atomic beam collimation experiments is the brightness, or radiance, that has been constructed in analogy to radiometry. The brightness combines the measures of atomic flux, beam size, and divergence. Following the definitions used in [69, 70] we have:

$$\mathcal{R} = \frac{\dot{N}}{\pi(\Delta x_\perp)^2 \Delta\Omega} \tag{6.2}$$

where the solid angle has been defined as

$$\Delta\Omega = \pi \left(\frac{\Delta v_\perp}{\overline{v}_\parallel} \right)^2 \tag{6.3}$$

and $\Delta x_\perp$ is the HWHM radius of the beam spot, $\Delta v_\perp$ is the HWHM of the tranverse velocity distribution, and $\overline{v}_\parallel$ is v_{long}. Taking the upper limit estimated for the divergence of the compressed beam, ± 3.8 m/s, gives a lower limit to the beam brightness of 1.9×10^{20} $\frac{\text{atoms}}{\text{s-sr-m}^2}$, an increase by a factor of ~ 4100 over the uncollimated brightness. Choosing the divergence estimate found from the spot size of the bichromatic collimated beam at the molasses stage yields a brightness of 5.7×10^{20} $\frac{\text{atoms}}{\text{s-sr-m}^2}$

6.5 Inefficiency of Bichromatic Collimation

While being a comparable flux density and brightness to other collimated metastable atomic beams, the potential is there for much more. We were only able to collect 1/4 of the estimated total output of the source into the collimated beam. There are several possible contributions to this inefficiency.

The capture range of the bichromatic force is quite large, but does not quite cover the full extent of the uncollimated beam. As can be seen in figure 6.14 the uncollimated beam extends out to ± 20 mm from its center, a full divergence of 250 mrad. However, the bichromatic collimation only collects

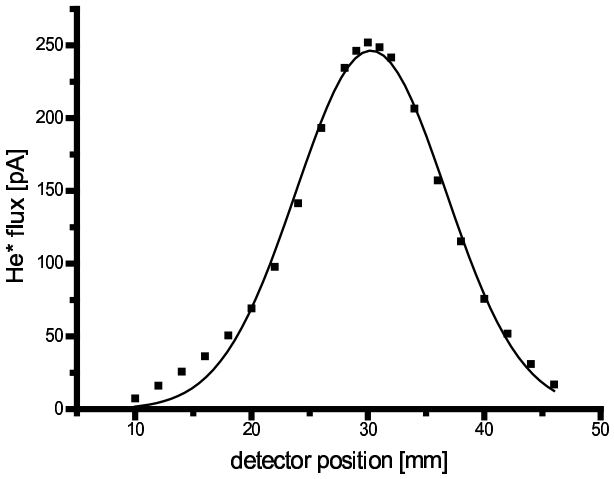

Figure 6.14 An SSD scan of the uncollimated beam at 16 cm from the skimmer (points) and a Gaussian fit (line). The fit gives a Gaussian waist of $w = 12.8$ mm, corresponding to a FWHM diameter of 15 mm, or a FWHM divergence of 90 mrad.

from an angle of 175 mrad. Figure 6.15 is a pictoral representation of the overlap of the bichromatic collimation capture ranges with the divergence of the full extent of the atomic beam. The capture range of each collimation transverse to the direction of collimation is limited by the finite size of the bichromatic light beams and the distance of the interaction region from the source skimmer. Assuming the Gaussian distribution from the fit of figure 6.14 and integrating over the area covered by collimation, we can estimate that 10% of the atomic beam is beyond the reach of collimation. Thus, the next generation of collimation should have slighty larger beams and bichromatic detuning. This would require more power in the beams, but with the fiber amplifiers, more than enough is available. However, this 10% is only a small

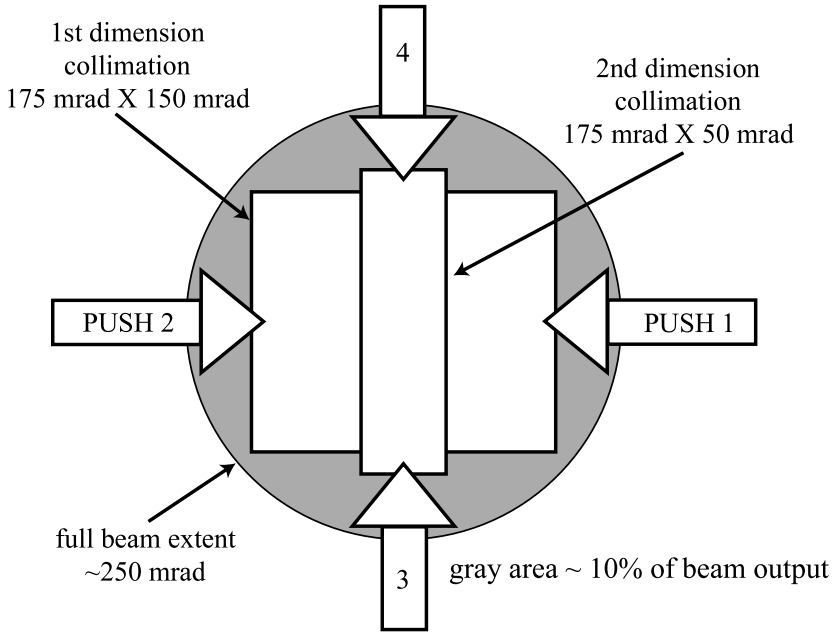

Figure 6.15 A representation of the angular overlap of bichromatic collimation with the full extent of the atomic beam. The angular reach of the collimation transverse to the direction of the pushes is determined by the size of the bichromatic light beam, w_{short}, and the distance of the interaction regions from the skimmer.

fraction of the 76% of the beam that is not in the collimated peak.

A significant portion of the atoms are not completely collimated because they have high longitudinal velocities. Figure 6.5 at the end of section 6.2 shows how the bichromatic force profile changes as the atoms traverse the interaction region, due to the Gaussian intensity profile of the bichromatic light beams (and thus changing Rabi frequencies). With light beams of Gaussian waist $w_{long} \sim 6.3$ mm, at ~ 3.15 mm from the center of the beam, the intensity has dropped from the peak value by 61% and thus the Rabi frequency was reduced to 78% of $\sqrt{\frac{3}{2}}\delta$, and at this point the force peaks at

$\sim 6\hbar k\gamma \sim \frac{1}{2}\frac{\hbar k\delta}{\pi} = \frac{1}{2}F_{bichro}$. At 3.5 mm from the center of the beam, the Rabi frequency has been reduced by 73% for which the peak value of the force is only $\sim \frac{1}{6}F_{bichro}$. We can use either of these points to define an effective interaction length with the bichromatic beams to be either 6.3 mm or 7 mm. The bichromatic slowing time, 5.9 μs, was calculated assuming the atom is slowed from $v = \delta/k$ to 0 m/s with a constant force of F_{bichro}. With an interaction length of 6.3 mm or 7 mm, atoms faster than 1100 m/s or 1200 m/s, respectively, are not in the effective interaction region long enough for the full bichromatic slowing time, and thus do not experience the full push. This means, referring to figure 3.3 (the longitudinal velocity distribution), that possibly 15 to 30% of the atoms do not experience the full bichromatic push to $v_\perp = 0$. This situation is supported by the observation of the broad shoulders to the collimated peak of 1D collimation in figure 6.4 (the atoms in the shoulders are not included in the estimation of the total flux of the collimated beam). This situation could be alleviated to some extent by re-collimating the beams to have a broader Gaussian waist (however, space is certainly limited), and by refurbishing the source and re-optimizing the operating parameters to reduce the longitudinal velocity without reducing the total source flux.

Another factor contributing to an atom not experiencing the total bichromatic push is the optical pumping time. The three sublevels (see figure

4.9) of the metastable "ground-state" are assumed to be equally populated as the atoms emerge from the source. For a given intensity of σ^+-polarized light, each $\Delta m = +1$ transition to the 2^3P_2 state has a different Rabi frequency based on the transition strength. We set the bichromatic light intensity to maximize the force for the cycling transition, $m_j = 1 \leftrightarrow 2$, and so for the other two σ^+ transitions the Rabi frequency and thus the bichromatic force is greatly reduced. So for an atom to experience the bichromatic force, it must be optically pumped to the $m_j = 1$ ground state, a process with a timescale constrained by the necessity of spontaneous emmision and the weaker excitation rates from the $m_j = -1, 0$ levels. The time for an atom to be pumped to the $m_j = 1$ sublevel is on the order of the flight time through the interaction region, such that possibly none of the atoms starting in the $m_j = -1$, and only half of the atoms starting in the $m_j = 0$ state experience a strong bichromatic force. Thus, potentially up to half of the atoms do not experience the full bichromatic push. Another addition to this effect is that our bichromatic beams are only $\sim 95\%$ circularly polarized. Even though the light is linearly polarized before and after the waveplates directly before and after the vacuum chamber, some phase between the linear components can be accumulated due to reflections off of the multiple number of mirrors delivering the beam. Implementing a solution to insure the atoms are optically pumped before entering

the effective interaction region is not straightforward. Inserting optical pumping beams would require the interaction regions to be spaced farther apart. Also, the light would have to be greatly modulated or focused/defocused to optically pump atoms over the full range of velocities of interest.

A simulation was written by Jörg Bochmann [71] (see Chapter 4 of [71] for an in-depth description) as an attempt to model the bichromatic collimation from interaction regions 1 and 2. The simulation incorporates the spatial separation between the two regions, the changing force profiles as the atoms traverse each region (calculated by the OBE Fortran code), the measured longitudinal and transverse velocity profiles, as well as having the force "turned off" for atoms which are not yet optically pumped. The actual "physics" at the heart of the simulation is based on simple classical dynamics. A comparison between the simulation and experiment is shown in figure 6.16. The simulation does match the experiment in correctly predicting the full angular range from which atoms can be collected. Also well matched is the FWHM of the collimated peak (i.e. the final velocity spread). The incorporation of the optical pumping times serves to match well the number of atoms not collected from the far left and right. However, the broad shoulders of the collimated peak are not present in the simulation results, even though the simulation does contain the longitudinal velocity distribution of figure 3.3. The discrepancy between

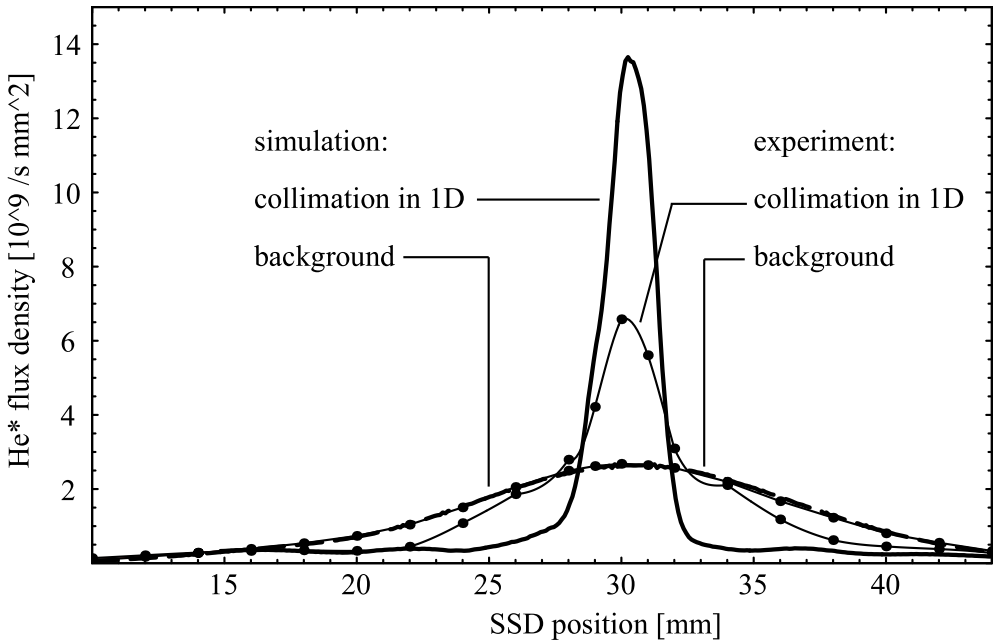

Figure 6.16 [71] Comparison between a numerical simulation and the experimental data of measured flux density for a scan with the SSD at 16 cm. The simulation matches the actual data quite well in terms of the capture range and in the FWHM of the collimated peak. Simulation parameters are set to as closely match the experiment as possible.

the simulation and the basic, yet strong, argument of insufficient bichromatic slowing time has not yet been resolved. It may lie in a poor understanding of momentum diffusion in the bichromatic collimation, which is not included in the simulation.

A factor that is not included in the simulation is the imbalancing of intensities between the counterpropagating beams. Although we used dielectric coated or high quality metallic mirrors, many surfaces still gave $\sim 1\%$ loss on reflection. In the phase delay path, where each beam ("$+kv_c$" and "$-kv_c$") is redirected to counterpropagate the other, this amounts to losses of 5 to 10%.

Thus adjusting the gain of the FA's to match the intensities at one interaction region would mean a greater mismatch at the other. In the end, the FA gains were set a priori to produce approximately the correct intensity for the first crossing of each bichromatic beam across the atomic beam, then the gains were optimized with minimal adjustment by looking at the total flux. Another source of mismatch in intensities is caused by imperfect collimation of the bichromatic light beams. We could measure the beam waists several meters away from the optical setup and see that one beam waist was smaller, and the other larger, than 6.3 mm. Unfortunately, even with great effort, we were not able to produce better collimation. A third and major contribution to the mismatch in intensities is the alignment of the counterpropagating beams. A slight ~ 1 mrad misalignment could destroy the alignment needed for collimation. However, perfect alignment could not be obtained either. In the case of perfect alignment, light from the output of one fiber amplifier was fed back into the output of the other (the FA's have no isolation on the output). While internal isolation prevented this feedback from reaching the diode laser itself, it did produce a great deal of feedback to the locking setup, and laser stability could not be maintained. Thus, the beams were required to be slightly misaligned. This difficulty could be alleviated by the investment in high power optical isolators.

Lastly, as each of the above mentioned parameters for bichromatic collimation become less than ideal, other effects besides the bichromatic force gain in prominence and possibly redistribute the atoms in undesired ways. These effects can be seen *outside* the area of bichromatic collimation in figure 6.1.

Chapter 7

Conclusion

Due to the low efficiencies ($\approx 10^{-5} - 10^{-4}$) at which metastable rare gas atoms are produced in typical gas discharge sources, there has always been great interest in effective ways of collimating beams of these atoms to increase their intensity and brightness [8]. Atomic flux and/or beam brightness are important considerations for a variety of experiments with these atoms, such as neutral atom lithography [60, 61], trap loading for Bose-Einstein condensation, photoassociation spectroscopy and ultra-cold collisions [62–65], and precision measurements [66, 67]. The large magnitude and short interaction lengths of the bichromatic force make for a very attractive method of improving beam intensity and brightness.

The bichromatic force can be used as a powerful tool in atomic beam

manipulation as it overcomes the limits imposed, by monochromatic light manipulation, on force magnitude and velocity range. We have utilized the bichromatic force for atomic beam collimation. Collimation is a new developement over past bichromatic experiments. Previous bichromatic experiments of beam slowing and deflection [38, 39, 59, 72, 73] were based on a single bichromatic force interaction region. Here, we have collimated a metastable helium beam in two dimensions using four interaction regions which were derived from a single diode laser and with only 5 cm total interaction length. The result is an unprecedented collimation of atoms from within a 175 mrad cone from the source, corresponding to a capture velocity of ± 87 m/s. The collimation yields a significant increase in peak flux density and brightness, with a factor of 5 reduction in the velocity spread of the beam. An additional simple optical molasses was applied to further compress the collimated beam giving a total increase in brightness of a factor of 4100 over the uncollimated beam. These results are summarized in Table 7.

The 20 eV internal energy of the He* atom make it quite useful for neutral atom lithography. The bichromatic collimation setup presented here can be considered a first generation beamline for neutral atom lithography, and progress is underway to use it for simple exposures. With the flux density acheived, exposure times should be on the order of minutes, at par with other

Quantity	Peak Flux Density	Spot Size FWHM	Divergence FWHM	Total Flux	Brightness
Units	atoms/s-mm^2	mm	mrad	atoms/s	atoms/s-sr-m^2
Raw Beam	0.3×10^9	50	90	5.9×10^{11}	4.6×10^{16}
2D BF	1.8×10^9	10	17.5	1.4×10^{11}	7.1×10^{18}
+molasses	9.0×10^9	3.5×5	≤ 7.5	1.2×10^{11}	$\geq 1.9 \times 10^{20}$

Table 7.1 A summary of the results at 56 cm from the source skimmer. For the raw beam the total flux is the estimated total output of source. "2D BF" is bichromatic collimation in two dimensions, while "+molasses" is two dimnesional bichromatic colliamtion followed by the optical molasses. The results are with the source discharge source discharge at 12 mA.

current experiments [61]. A new source is being constructed, and with further improvements of the collimation efficiency, as well as optmizing the new source to run more stably at higher discharge and lower pressures, sub-minute exposure times may be possible.

Bibliography

[1] D. Wineland and H. Dehmelt, Bull. Am. Phys. Soc. **20**, 637 (1975).

[2] T. Hänsch and A. Schawlow, Opt. Commun. **13**, 68 (1975).

[3] D. Wineland and W. Itano, Phys. Rev. A **20**, 1521 (1979).

[4] P. Meystre and S. S. (Eds.), J. Opt. Soc. Am. B **2**, 1705 (1985).

[5] S. Chu and C. Wieman, J. Opt. Soc. Am. B **6**, 2020 (1989).

[6] W. Phillips and H. Metcalf, Phys. Rev. Lett. **48**, 596 (1982).

[7] J. Prodan, W. Phillips, and H. Metcalf, Phys. Rev. Lett. **49**, 1149 (1982).

[8] H. Metcalf and P. van der Straten, *Laser Cooling and Trapping* (Springer, New York, 1999).

[9] C. Adams and E. Riis, Prog. Quantum Electron. **21**, 1 (1997).

[10] D. Suter, *The Physics of Laser-Atom Interactions* (Cambridge University Press, Cambridge, 1997).

[11] P. Lett, R. Watts, C. Westbrook, W. Phillips, P. Gould, and H. Metcalf, Phys. Rev. Lett. **61**, 169 (1988).

[12] P. Ungar, D. Weiss, S. Chu, and E. Riis, J. Opt. Soc. Am. B **6**, 2058 (1989).

[13] J. Dalibard and C. Cohen-Tannoudji, J.Opt.Soc.Am. B **6**, 2023 (1989).

[14] C. Cohen-Tannoudji and W. Phillips, Phys. Today **43**, October, 33 (1990).

[15] J. Dalibard and C. Cohen-Tannoudji, J. Opt. Soc. Am. B **2**, 1707 (1985).

[16] E. Kyrola and S. Stenholm, Opt. Commun. **22**, 123 (1977).

[17] A. Kazantsev and I. Krasnov, Zh. Eksp. Teor. Fiz. **95**, 104 (1989).

[18] V. Voitsekhovich, M. Danileiko, A. Negriiko, V. Romanenko, and L. Yatsenko, Pisma Zhur. Teor. Eksp. Fiz. **49**, 138 (1989), [JETP Lett. **49**, 161-164, (1989)].

[19] R. Grimm, G. Wasik, J. Söding, and Y. Ovchinnikov, in *Proceedings of the Fermi School CXXXI*, edited by A. Aspect, W. Barletta, and R. Bonifacio (IOS Press, Amsterdam, 1996), p. 481.

[20] R. Grimm, Y. Ovchinnikov, A. Sidorov, and V. Letokhov, Phys. Rev. Lett. **65**, 1415 (1990).

[21] V. Voitsekhovich, M. Danileiko, A. Negriiko, and et al., Zh. Eksp. Teor. Fiz. **99**, 393 (1991), [Sov. Phys. JETP **72**, 219-227, (1992)].

[22] R. Gupta, C. Xie, S. Padua, H. Batelaan, and H. Metcalf, Phys. Rev. Lett. **71**, 3087 (1993).

[23] V. Voitsekhovich, M. Danileiko, A. Negriiko, V. Romanenko, and L. Yatsenko, Zh. Tekh. Fiz. **58**, 1174 (1988), [Sov. Phys. Tech. Phys. **33**, 690-691, (1988)].

[24] L. Allen and J. Eberly, *Optical Resonance and Two-Level Atoms* (Dover, New York, 1975).

[25] R. Grimm, J. Söding, and Y. Ovchinnikov, Opt. Lett. **19**, 658 (1994).

[26] R. Grimm, G. Wasik, J. Söding, and Y. Ovchinnikov, in *Proceedings of the Fermi School CXXXI*, edited by A. Aspect, W. Barletta, and R. Bonifacio (IOS Press, Amsterdam, 1996), p. 481.

[27] L. Yatsenko and H. Metcalf, accepted for publication in Phys. Rev. A (unpublished).

[28] C. Cohen-Tannoudji, J. Dupont-Roc, and G. Grynberg, *Atom-Photon Interactions* (J. Wiley & Sons, New York, 1992).

[29] L. Landau and E. Lifshitz, *Quantum Mechanics (Non-Relativistic Theory)* (Pergamon Press, Oxford, 1958).

[30] J. R. Rubbmark, M. M. Kash, M. G. Littman, and D. Kleppner, Phys. Rev. A **23**, 3107 (1981).

[31] J. Shirley, Phys. Rev. **138**, B 979 (1965).

[32] S. Guérin and H. Jauslin, Adv. Chem. Phys. **125**, 1 (1993).

[33] J. Söding, Ph.D. thesis, Univ. Heidelberg, 1996.

[34] M. Williams, Ph.D. thesis, Stony Brook University, 1999.

[35] M. Cashen, Ph.D. thesis, Stony Brook University, 2002.

[36] R. Feynman, F. Vernon, and R. Hellwarth, J. App. Phys. **28**, 49 (1957).

[37] P. Ehrenfest, Zeit. f. Phys. **45**, 455 (1927).

[38] M. Williams, F. Chi, M. Cashen, and H. Metcalf, Phys. Rev. A **60**, R1763 (1999).

[39] M. Williams, F. Chi, M. Cashen, and H. Metcalf, Phys. Rev. A **61**, 023408 (2000).

[40] J. Kawanaka, M. Hagiuda, K. Shimizu, F. Shimizu, and H. Takuma, App. Phys. B **56**, 21 (1993).

[41] H. Mastwijk, Ph.D. thesis, Utrecht University, 1997.

[42] H. Mastwijk, J. Thomsen, P. van der Straten, and A. Niehaus, Phys. Rev. Lett. **80**, 5516 (1998).

[43] W. Lu, M. Hoogerland, D. Milic, K. Baldwin, and S. Buckman, Rev. Sci. Instrum. **72**, 2558 (2001).

[44] T. Chuang, Ph.D. thesis, Stony Brook University, 1991.

[45] G. Woestenenk, J. Thomsen, M. van Rijnbach, P. van der Straten, and A. Niehaus, Rev. Sci. Instrum. **72**, 3842 (2001).

[46] F. B. Dunning, R. D. Rundel, and R. F. Stebbings, Rev. Sci. Instrum. **46**, 697 (1975).

[47] C. Wieman and L. Hollberg, Rev. Sci. Instrum. **62**, 1 (1991).

[48] C. Bohler and B. Marton, Opt. Lett. **19**, 1346 (1994).

[49] G. Agrawal, *Fiber-Optic Communication Systems, 3rd Edition* (Wiley-Interscience, New York, 2002).

[50] L. Coldren and S. Corzine, *Diode Lasers and Photonic Integrated Circuits* (John Wiley & Sons, New York, 1995).

[51] S. C. of a 1083 nm Diode Laser, Master's thesis, Stony Brook University, 1998.

[52] M. Prevedelli, P. Cancio, G. Giusfredi, F. Pavone, and M. Inguscio, Opt. Comm. **125**, 231 (1996).

[53] W. Demtröder, *Laser Spectroscopy - Basic Concepts and Instrumentation - 3rd Edition* (Springer-Verlag, Berlin, 2003).

[54] B. Saleh and M. Teich, *Fundamentals of Photonics* (John Wiley & Sons, New York, 1991).

[55] G. Agrawal, *Nonlinear Fiber Optics, 3rd Edition* (Academic Press, San Diego, 2001).

[56] P. Milonni and J. Eberly, *Lasers* (Wiley, New York, 1988).

[57] R. Ulrich, S. Rashleigh, and W. Eickhoff, Opt. Lett. **5**, 273 (1980).

[58] B. Cagnac and J. Pebay-Peyroula, *Modern Atomic Physics* (Wiley, New York, 1975).

[59] M. Cashen and H. Metcalf, J. Opt. Soc. Am. B **20**, 915 (2003).

[60] D. Meschede and H. Metcalf, J. Phys. D: Appl. Phys. **36**, R17 (2003).

[61] S. Petra, L. Feenstra, W. Hogervorst, and W. Vassen, App. Phys. B **78**, 133 (2004).

[62] A. Robert, O. Sirjean, A. Browaeys, J. Poupard, S. Nowak, D. Boiron, C. I. Westbrook, and A. Aspect, Science **292**, 461 (2001).

[63] F. P. D. Santos, J. Lonard, J. Wang, C. Barrelet, F. Perales, E. Rasel, C. Unnikrishnan, M. Leduc, and C. Cohen-Tannoudji, Phys. Rev. Lett. **86**, 3459 (2001).

[64] N. Herschbach, P. Tol, W. Vassen, W. Hogervorst, G. Woestenenk, J. Thomsen, P. van der Straten, and A. Niehaus, Phys. Rev. Lett. **84**, 1874 (2000).

[65] M. Pieksma, M. Čížek, J. Thomsen, P. van der Straten, and A. Niehaus, Phys. Rev. A **66**, 022703 (2002).

[66] L.-B. Wang, P. Mueller, G. Drake, J. Greene, D. Henderson, R. Holt, R. Janssens, C. Jiang, Z.-T. Lu, T. O'Connor, R. Pardo, K. Rehm, J. Schiffer, and X. Tang, Phys. Rev. Lett. **93**, 142501 (2004).

[67] M. George, L. Lombardi, and E. Hessels, Phys. Rev. Lett. **87**, 173002 (2001).

[68] W. Rooijakkers, W. Hogervorst, and W. Vassen, Opt. Commun. **123**, 321 (1996).

[69] F. Lison, D. Haubrich, P. Schuh, and D. Meschede, Appl. Phys. B **69**, 501 (1999).

[70] J. Tempelaars, R. Stas, P. Sebel, H. Beijerinck, and E. Vredenbregt, Europhys. J. D **18**, 113 (2002).

[71] J. Bochmann, Master's thesis, Stony Brook University, 2004.

[72] J. Söding, R. Grimm, Y. Ovchinnikov, P. Bouyer, and C. Salomon, Phys. Rev. Lett. **78**, 1420 (1997).

[73] M. Cashen and H. Metcalf, Phys. Rev. A **63**, 025406 (2001).